Study of self-modulation of an electron beam in plasma

Dissertation
zur Erlangung des Doktorgrades
an der Fakultät für Mathematik, Informatik
und Naturwissenschaften
Fachbereich Physik
der Universität Hamburg

vorgelegt von
Osip Lishilin

Hamburg
2018

Gutachter der Dissertation:	Prof. Dr. Florian Grüner Prof. Dr. Wolfgang Hillert
Zusammensetzung der Prüfungskomission:	Prof. Dr. Sven-Olaf Moch Prof. Dr. Florian Grüner Prof. Dr. Wolfgang Hillert Dr. Matthias Groß Dr. Jens Osterhoff
Vorsitzender der Prüfungskomission:	Prof. Dr. Sven-Olaf Moch
Datum der Disputation:	25.09.2018
Vorsitzender Fach-Promotionsausschusses PHYSIK:	Prof. Dr. Wolfgang Hansen
Leiter des Fachbereichs PHYSIK:	Prof. Dr. Michael Potthoff
Dekan der Fakultat für Mathematik, Informatik und Naturwissenschaften:	Prof. Dr. Heinrich Graener

Abstract

The acceleration of electron beams in plasma wakefields driven by charged particle beams is among the most promising candidates for future TeV-scale compact electron accelerators. Currently available high energy proton beams that could serve as driver beams in a plasma wakefield accelerator (PWFA) are much longer than what is required for efficient excitation of high-amplitude wakefields and thus for generating the desired high acceleration gradients. The self-modulation instability (SMI) is a phenomenon which enables the transformation of a long charged particle beam into a train of equidistant short bunches when passing through a plasma. Such bunch trains can resonantly drive wakefields in plasma and generate multi-GV/m acceleration gradients. The proof-of-principle experiment AWAKE was started at CERN to demonstrate acceleration of electrons in plasma wakefields driven by self-modulated proton beams.

Since the underlying physics of the SMI is the same for any charged particle beam, the use of electron beams for studying the SMI is an appealing option, as the electron beams are easier to handle. The Photo Injector Test facility at DESY in Zeuthen (PITZ) offers a unique possibility to study and experimentally demonstrate the self-modulation of long electron beams in plasma: it is capable of generating long electron beams, and it possesses a variety of diagnostic devices for the electron beam characterization. For the SMI studies, measurements of the longitudinal phase space are of main importance, as they reflect characteristic features of the SMI.

This work is devoted to the first experimental demonstration of the SMI by using long electron beams passing through a plasma. Preparations for the self-modulation experiment, including the development of a plasma source, are described. Results of the first longitudinal phase space measurements of the SMI at PITZ and supporting beam dynamics simulations are presented.

Zusammenfassung

Die Beschleunigung von Elektronenstrahlen in Plasma-Wakefeldern, die von geladenen Teilchenstrahlen angetrieben werden, gehört zu den vielversprechendsten Kandidaten für zukünftige kompakte Elektronenbeschleuniger im TeV-Bereich. Derzeit verfügbare Hochenergie-Protonenstrahlen, die als Treiberstrahlen in einem Plasma-Wakefeld-Beschleuniger (PWFA) eingesetzt werden könnten, sind viel länger als das, was zur effizienten Anregung von Wakefeldern mit hoher Amplitude und damit zur Erzeugung der gewünschten hohen Beschleunigungsgradienten erforderlich ist. Die self-modulation instability (SMI) ist ein Phänomen, das die Umwandlung eines langen geladenen Teilchenstrahls in eine Folge äquidistanter kurzer Bündel beim Durchgang durch Plasma ermöglicht. Solche Bündelzüge können Wakefelder im Plasma resonant antreiben und Beschleunigungsgradienten mit mehreren GV/m erzeugen. Am CERN wurde das Experiment AWAKE als Machbarkeitsstudie gestartet, um die Beschleunigung von Elektronen in Plasma-Wakefeldern zu demonstrieren, die von selbstmodulierten (self-modulated) Protonenstrahlen angetrieben werden.

Da die zugrundeliegende Physik der SMI für jeden geladenen Teilchenstrahl die gleiche ist, ist die Verwendung von Elektronenstrahlen zur Untersuchung der SMI eine attraktive Option, da Elektronenstrahlen leichter zu handhaben sind. Die Photo Injector Test Facility (PITZ) bei DESY in Zeuthen bietet die einzigartige Möglichkeit, die Eigenmodulation (self-modulation) langer Elektronenstrahlen im Plasma zu studieren und experimentell zu demonstrieren: hier können lange Elektronenstrahlen erzeugt werden und das Labor verfügt über eine Vielzahl von Diagnosegeräten für die Charakterisierung des Elektronenstrahls. Für die SMI-Untersuchungen sind Messungen des longitudinalen Phasenraums von großer Bedeutung, da sie charakteristische Merkmale der SMI widerspiegeln.

Diese Arbeit beschäftigt sich mit der ersten experimentellen Demonstration der SMI, für die lange Elektronenstrahlen durch Plasma geleitet wurden. Vorbereitungen für das Eigenmodulations-Experiment, einschließlich der Entwicklung einer Plasmaquelle, werden hier beschrieben. Ergebnisse der ersten longitudinalen Phasenraummessungen des SMI bei PITZ und unterstützende Strahldynamiksimulationen werden vorgestellt.

Contents

Chapter 1

Introduction

Particle accelerators have applications in many aspects of modern life: industry, security, medicine, applied and fundamental science. The accelerated particle energy typically ranges from hundreds of keV to TeVs, and lots of scientific applications require high energies. Conventional accelerating structures are resonant radio-frequency (RF) cavities where particles are accelerated by electromagnetic waves. The probability of the electrical breakdown in the RF cavity rises with the amplitude of the electromagnetic field. An amplitude of 100 MV/m is the current practical limit for cavity-based accelerating structures. A TeV-scale linear accelerator built based on the conventional accelerating technology would be several tens of kilometers long. For example, the baseline design of the International Linear Collider involves the use of two 11 km long linear accelerators (linacs) in order to achieve the center-of-mass energy of 500 GeV [1]. Another example is the proposed design for a Compact Linear Collider (CLIC) [2]: two 25 km long linacs are needed to reach the center-of-mass energy of 3 TeV. Circular accelerators utilize the same kind of accelerating structure to accelerate particles multiple times (once per turn), but this approach also suffers from limitations. The synchrotron radiation occurs during curvilinear motion of charged particles. The power of the synchrotron radiation P depends on the particle energy E, the particle mass m and the trajectory radius R:

$$P \sim \frac{1}{R^2} \left(\frac{E}{mc^2} \right)^4 . \tag{1.1}$$

The synchrotron radiation losses increase very sharply with the particle energy, and in order to fully compensate that increase, one should scale the trajectory radius quadratically with the energy. Electrons and positrons have much higher synchrotron losses compared to that of heavier protons and ions; effectively, the synchrotron radiation is the current limiting factor for circular lepton accelerators. The highest energy achieved for electron synchrotrons is about 100 GeV [3]. The most powerful circular accelerator up to date is the Large Hadron Collider with the center-of-mass energy up to 14 TeV.

Plasma wakefield acceleration (PWFA) is an alternative proposed to the conven-

tional accelerating structures. In this scheme, particles are accelerated by high (up to 100 GV/m) electric gradients that occur in plasma waves driven by high-intensity laser pulses [4] or relativistic particle beams [5]. The production of GeV-scale beams was already demonstrated [6–9]. PWFA would allow to increase the energy level significantly while keeping the physical dimensions of new accelerator complexes comparable to that of existing ones. For example, a CLIC-like complex based on a multi-staged laser wakefield acceleration scheme would require a 10 times shorter acceleration length [10]. A compact plasma-based source of GeV-scale monoenergetic electrons can drive a free-electron laser, providing an affordable tool for material science and biological studies. Future plasma-based ion sources have a broad spectrum of applications, such as material treatment, energy research, and medical applications [11].

1.1 PWFA principles

Plasma waves are driven either by a laser pulse or a relativistic charged particle beam (the driver). Electrons of quasi-neutral plasma are pushed away from the driver path (due to the laser pondermotive force or the particle beam space charge forces in case of a negatively charged particle driver) while heavier ions of the plasma remain static on the time scale of the electron reaction. The restoring Coulomb force pushes the plasma electrons back to neutralize the charge imbalance created by the driver. In case of a positively charged particle driver, the plasma electrons are attracted towards the axis of the driver first and then pushed back due to the charge imbalance. The electrons exercise an oscillatory movement around the trajectory of the driver governed by the Coulomb force; the frequency of these oscillations is the plasma electron frequency ω_p. The field that occurs in plasma behind the driver is called the wakefield. An electron bunch propagating in plasma behind the driver, also called the witness bunch, can be accelerated if placed in a proper phase of the wakefield (Fig. 1.1). Additionally, there is a transverse wakefield component which can focus or defocus the electron beam. The transverse field has a 90° phase offset with respect to the longitudinal field, so there is a phase region where the witness bunch experience both accelerating and focusing forces [12].

The longitudinal electric field produced by displacement of charges can be found applying Gauss's law:

$$\oint \mathbf{E} \cdot \, d\mathbf{S} = \frac{1}{\varepsilon_0} \int \rho \, dV, \tag{1.2}$$

$$E = \frac{nex}{\varepsilon_0}, \tag{1.3}$$

where E is the electric field, S is the closed surface, ρ is the charge density, V is the volume of the region inside the closed surface S, n is the density of the electrons, x is

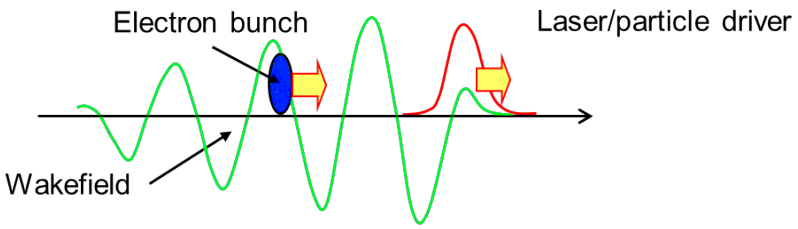

Figure 1.1: Wakefield (green curve) following the driver pulse (red curve). The witness bunch samples the wakefield (gains energy).

their displacement with respect to static ions, and ε_0 is the the vacuum permittivity [13]. The plasma frequency ω_p can be obtained from the equation of motion:

$$F = m\frac{d^2x}{dt^2} = -eE = -\frac{ne^2x}{\varepsilon_0}, \tag{1.4}$$

$$\omega_p^2 = \frac{ne^2}{\varepsilon_0 m}, \tag{1.5}$$

where m is the electron mass. The maximal electrical field created in plasma (for the case of a total charge separation, i.e. that the driver expels all the plasma electrons in a certain volume) can be estimated if a displacement of $x \sim \lambda_p \sim \frac{c}{\omega_p}$ is assumed:

$$E \sim \frac{nec}{\varepsilon_0\omega_p} = \frac{mc\omega_p}{e} \tag{1.6}$$

or

$$eE \sim \frac{mc^2\omega_p}{c}. \tag{1.7}$$

It can be seen that for a relatively low plasma density of $1 \times 10^{15}\,\mathrm{cm}^{-3}$ the maximum electric field is $3\,\mathrm{GV/m}$ which is substantially higher than that in conventional accelerating structures. The maximum amplitude of the electric field E in plasma can be estimated [14] as

$$E[\mathrm{V/m}] \propto 96\sqrt{n[\mathrm{cm}^{-3}]}, \tag{1.8}$$

where n is the plasma density.

The plasma wavelength λ_p can be quickly estimated from the plasma density n using the practical formula

$$\lambda_p[\mathrm{mm}] \approx \sqrt{\frac{10^{15}\,\mathrm{cm}^{-3}}{n\ [\mathrm{cm}^{-3}]}}. \tag{1.9}$$

1.2 Laser or beam drivers?

The achievable energy gain in plasma accelerators depends both on the electric field strength and on the distance the particles travel while being subjected to that field, also called the dephasing length. If the witness bunch "slips" out of the acceleration phase, it will not gain energy anymore. The phase slippage occurs due to a difference of the propagation speed of the witness bunch and the wake phase velocity. Usually, the dephasing length is defined as the propagation distance required for the witness bunch to slip $\lambda_p/2$ (or the wake phase of π) with respect to the plasma wave [15]. Sometimes the dephasing length is associated with the distance required for the witness bunch to slip $\lambda_p/4$ – in that case the witness bunch remains both in the accelerating phase of the longitudinal field and in the focusing phase of the transverse field over the dephasing length. As the witness bunch gains energy and accelerates, it eventually overruns the wakefield and slips into deceleration phase of the wakefield. In case of a laser driver, the wake phase velocity is equal to the laser group velocity in plasma; for that case, the Lorentz factor of the plasma wake is given as [16]

$$\gamma_\varphi = \frac{1}{\sqrt{3}}\sqrt{\frac{n_{cr}}{n_p}}, \tag{1.10}$$

where $n_{cr} = \varepsilon m\omega^2/e^2$ is the critical density, ω is the laser frequency and n_p is the plasma density. In case of a beam-driven wake, its phase velocity is equal to the driver beam velocity ($\approx c$ for high relativistic driver beams). The typical dephasing length for laser-driven wakefield accelerators is on the order of 10 cm, while for the case of beam-driven plasma accelerators this length can be several orders of magnitude longer. Dephasing can be partially mitigated by using plasma density tapering [17].

Another limiting factor for a laser driver is the Rayleigh length which is the propagation distance between a focal point and the point where the laser transverse spot area is doubled. For laser-driven plasma accelerators, this length is usually in the range from several millimeters to few centimeters; that means that the energy density of a laser driver changes significantly over a short distance. In order to effectively drive a plasma wake over a longer distance, a laser needs a guiding mechanism. This can be achieved using a waveguide or an axicon, or by means of self-guiding by utilizing the Kerr nonlinearity [18]. Laser-driven plasma acceleration over a distance of 9 cm was demonstrated using self-focusing of a laser in a plasma [9]. On the other hand, particle beams diverge on the scale of the β function at a focal point, and that distance can be substantially larger than that of laser pulses.

The ultimate energy gain limiting factor for laser-driven accelerators is the laser pump depletion length – the distance over that the laser driver loses its energy and cannot drive the plasma wake anymore. The depletion length is given as $L_d \sim {\lambda_p}^3/\lambda^2$ where λ_p is the plasma wavelength and λ is the driver laser wavelength [19]. The depletion length depends on acceleration regimes and strongly varies for different setups. In the linear regime (the plasma density modulations are small and quasi-sinusoidal),

the length of the acceleration stage is primarily limited by the Rayleigh length and the dephasing length and then by the depletion length [18]. If one mitigates the first two constraints, the latter one also can be manipulated by, for instance, lowering the plasma density. However, that will cause a decrease of the acceleration gradient and elongation of the acceleration stage.

These factors limit the length of the laser-driven wakefield accelerator and lead to a potentially complicated multi-stage scheme. Such schemes require a very precise stage-to-stage synchronization and alignment [20, 21].

1.3 The AWAKE experiment

So far electron beams were used as drivers for all PWFA demonstrations for ease of experimental setup. However, as mentioned before, the currently existing hadron accelerators can produce beams of much higher energies compared to that of electron accelerators. These hadron beams can serve as drivers and provide TeV-scale energy gain in single-staged PWFA [22]. In order to implement this scheme, one needs to use very short proton drivers (on the order of hundreds of µm), while existing high energy proton bunches from the Super Proton Synchrotron (SPS, CERN) are about 12 cm long. Soon a solution emerged: a long charged particle bunch that propagates through a plasma can be subjected to an instability that splits the bunch to a set of short sub-bunches [23]. This instability, called the self-modulation instability (SMI), develops due to a coupling between the transverse wakefield and the bunch radius evolution: initially, the long bunch gets modulated by a relatively small wake driven by its head, and then the wake is amplified through modulations of the beam. Eventually, the bunch is split into sub-bunches completely. The spacing between sub-bunches is equal to the plasma wavelength λ_p, and their length is less than λ_p, which allows to resonantly drive a high amplitude wake and utilize it for acceleration of electrons. The Advanced Proton-Driven Plasma Wakefield Acceleration Experiment (AWAKE) has been launched at CERN [24]. The experiment aims to demonstrate and study the SMI of a 12 cm long 400 GeV proton beam from the SPS in plasma and to accelerate electrons from approximately 15 MeV up to 1.8 GeV. The proton beam self-modulation takes place in a 4-meter-long plasma stage, followed by a 10-meter-long plasma stage for the electron acceleration [25].

1.4 SMI at PITZ

The self-modulation of long charged particle beams in plasma has been extensively studied analytically and by means of beam dynamics simulations, but there are only a few experimental indications of the SMI [26, 27]. To provide direct proof of the SMI, an experiment was launched at the Photo Injector Test facility at DESY in Zeuthen (PITZ). Its goals are to unambiguously demonstrate and study the SMI of

long electron beams passing through the plasma to provide insight for proton-driven experiments since the underlying physics of the SMI is the same. The primary objective of the experiment is to measure the longitudinal phase-space (LPS) of a flat-top electron beam after its propagation in plasma, as the main properties of the SMI can be obtained from that measurement: the magnitude and the phase velocity of the accelerating fields. Key devices of the experiment are a heat pipe based plasma cell, a photocathode laser system which enables production of long electron beams with sharp rising edges, and well-developed diagnostics at PITZ including a transverse deflecting cavity and a high-resolution electron spectrometer.

The main purpose of this thesis is to prepare the experimental setup, perform the first unambiguous experiments and characterize the self-modulation instability generated by passing long electron beams from PITZ through a lithium heat pipe plasma oven. This chapter described the background and scientific interest of the work carried out in this thesis. The following chapters include the theoretical basis of plasma physics and the SMI, an introduction to the PITZ facility, a description of the plasma cell and preparatory studies, the SMI experiment, supporting beam dynamics simulations and conclusions.

Chapter 2

Theoretical basics

This chapter briefly describes the physics behind the experiment. Basic plasma physics is introduced here (including the two-fluid approach to describe wave propagation in plasma) as well as a theoretical model of the self-modulation instability of electron beams in plasma.

2.1 Properties of plasma

Plasma is often defined as a quasi-neutral gas of charged particles. Plasma consists of free electrons and ions, and for unperturbed plasma, their charge densities cancel out each other:

$$n_e \approx Z n_i, \tag{2.1}$$

where n_e is the electron density, Z is the ion charge, and n_i is the ion density. Ideal plasma demonstrates a "collective" behavior, i.e., its dynamics is dominated by macroscopic fields and not by interactions of single particles. A local charge imbalance with density $\rho = e(Zn_i - n_e)$ will immediately create an electrostatic field:

$$\nabla \cdot \mathbf{E} = \frac{\rho}{\varepsilon_0}, \tag{2.2}$$

where e is the electron charge, ε_0 is the vacuum permittivity. Similarly, a set of moving particles creates a local current density $\mathbf{J} = e(Zn_i\mathbf{v}_i - n_e\mathbf{v}_e)$, which induces a magnetic field:

$$\nabla \times \mathbf{B} = \mu_0 \mathbf{J}, \tag{2.3}$$

where $\mathbf{v}_i$ and $\mathbf{v}_e$ are the ion and electron velocities, μ_0 is the vacuum permeability. These fields define the dynamics of the plasma, including its response to externally applied fields (e.g., through laser or particle beams).

2.2 Debye length

Plasma tends to counteract any disturbances, i.e., it tries to neutralize a local charge imbalance. Consider a positively charged sphere put in a plasma. Positive ions will be pushed away from the sphere and electrons will be attracted to it. One can estimate the potential φ of the sphere after the redistribution of the charge. Assuming equal ion and electron temperature,

$$\frac{1}{2}m_e\overline{v_e}^2 = \frac{1}{2}m_i\overline{v_i}^2 = \frac{3}{2}k_BT, \tag{2.4}$$

where m_e, m_i, $\overline{v_e}$ and $\overline{v_i}$ are the masses and the root mean square velocities of the electrons and ions, correspondingly, k_B is the Boltzmann constant, and T is the temperature, the thermal velocities of ions and electrons can be estimated as

$$\frac{\overline{v_i}}{\overline{v_e}} = \sqrt{\frac{m_e}{m_i}}. \tag{2.5}$$

For hydrogen plasma, the ion velocity is much lower than that of electrons,

$$\frac{\overline{v_i}}{\overline{v_e}} = \frac{1}{43}, \tag{2.6}$$

so the ion movement can be neglected. For other chemical elements, this ratio is even smaller, so in general ions are assumed to be static. In thermal equilibrium, the electron density n_e is governed by the Boltzmann distribution [28]:

$$n_e = n_i \exp\left(\frac{e\ \varphi(r)}{k_BT}\right), \tag{2.7}$$

where $\varphi(r)$ is the externally created potential. From Gauss's law, for a single-ionized plasma ($Z = 1$)

$$\nabla^2\varphi = -\frac{\rho}{\varepsilon_0} = -\frac{e(n_i - n_e)}{\varepsilon_0}. \tag{2.8}$$

Combining Eqs. (2.7) and (2.8) in spherical geometry yields a physically meaningful solution:

$$\varphi_D = \frac{1}{4\pi\varepsilon_0}\frac{\exp\left(-r/\lambda_D\right)}{r}. \tag{2.9}$$

λ_D is the Debye length and it is given as

$$\lambda_D = \frac{\varepsilon_0 k_B T}{e^2 n_e}. \tag{2.10}$$

The Debye length is a characteristic property of plasma, and it indicates how far the electric field of an introduced charge spreads into quasi-neutral plasma. It depends both

on the electron density and the plasma temperature. Outside the Debye length, the introduced electrical field is screened because of polarization of the plasma surrounding the introduced charge. Classical plasma theory assumes that there are many charged particles within the Debye sphere volume,

$$N_D = n_e \frac{4\pi}{3} {\lambda_D}^3 \gg 1, \tag{2.11}$$

so collective effects in plasma prevail over particle collisions effects.

2.3 Electromagnetic waves in plasma

The propagation of electromagnetic (EM) waves in plasma is a vast theoretical field, and many textbooks are devoted to this topic, e.g. [28–30]. The types of waves that can exist in plasma depend on local plasma properties, the external EM fields, and other factors. There are different models to describe waves in plasma: N-body molecular dynamics, the Vlasov-Boltzmann equations, magnetized fluid equations, and two-fluid equations. These models have their own scopes of application and advantages. Here only longitudinal and transverse electromagnetic waves are discussed, which is sufficient for the topic of this work. The two-fluid equations model suits well for the description of dynamics of collisionless non-relativistic plasma with a finite temperature. This model treats different components, or species (s), of plasma as fluids with their densities n_s and velocities $\mathbf{v}_s$. These fluids interact with each other via electric and magnetic fields. The following equations govern plasma dynamics:

$$\frac{\partial n_s}{\partial t} + \nabla \cdot (n_s \mathbf{v}_s) = 0, \tag{2.12}$$

$$n_s m_s \frac{dv}{dt} = n_s q_s (\mathbf{E} + \mathbf{v}_s \times \mathbf{B}) - \nabla P_s, \tag{2.13}$$

$$\frac{d}{dt}(P_s n_s^{-\gamma_s}) = 0, \tag{2.14}$$

where $v \ll c$, q_s is the charge of plasma species m_s is the mass of plasma species, P_s is the thermal pressure of plasma species, and γ_s is the specific heat ratio, $\gamma_s = (2+N)/N$, where N is the number of degrees of freedom [28].

The continuity Eq. (2.12) can be rewritten as a charge conservation equation:

$$\frac{\partial \rho_s}{\partial t} + \nabla \cdot \mathbf{J}_s = 0, \tag{2.15}$$

where $\rho_s = n_s q_s$ is the charge density and $\mathbf{J}_s = n_s q_s \mathbf{v}_s$ is the current density.

Equation (2.13) describes the motion of plasma species s in the presence of electric and magnetic fields. If the plasma is quasi-neutral ($n_e = Z n_i = n$), $\mathbf{v}_e = \mathbf{v}_i = \mathbf{v}$ and

there are no external fields, Eqs. (2.12) and (2.13) can be rewritten as the Navier-Stokes equations:

$$\frac{\partial \rho}{\partial t} + \nabla \cdot (\rho \mathbf{v}) = 0, \tag{2.16}$$

$$\frac{d\mathbf{v}}{dt} + (\mathbf{v} \cdot \nabla)\mathbf{v} = \frac{1}{\rho}\nabla P. \tag{2.17}$$

As it was justified before, ions can be assumed static ($\mathbf{v}_i = 0$). If considering unmagnetized plasma, Eq. (2.13) can be written as

$$n_e m_e \frac{dv}{dt} = n_e e\mathbf{E} - \nabla P_e. \tag{2.18}$$

Equations (2.12)–(2.14), combined with two Maxwell's equations

$$\nabla \times \mathbf{E} = -\frac{\partial \mathbf{B}}{\partial t}, \tag{2.19}$$

$$\nabla \times \mathbf{B} = \mu_0 \mathbf{J}_s + \mu_0 \varepsilon_0 \frac{\partial \mathbf{E}}{\partial t}. \tag{2.20}$$

present a system of equations, and the simultaneous solution of that system provides a self-consistent set of fields and motions in the two-fluid model approximation [28].

2.4 Longitudinal waves

For the two-fluid model, assuming $\mathbf{v}_i = 0$ and considering the electron motion in one dimension, the equation system (2.12)–(2.14) can be written as

$$\frac{\partial n_e}{\partial t} + \frac{\partial}{\partial x}(n_e v_e) = 0, \tag{2.21}$$

$$n_e\left(\frac{\partial v_e}{\partial t} + v_e \frac{\partial v_e}{\partial x}\right) = -\frac{e}{m} n_e E - \frac{1}{m_e}\frac{\partial P_e}{\partial x}, \tag{2.22}$$

$$\frac{d}{dt}(P_e n_e^{-\gamma_e}) = 0. \tag{2.23}$$

The system of equations (2.21)–(2.23) can be solved by adding a fourth equation (Poisson's equation)

$$\frac{\partial E}{\partial x} = \frac{e}{\varepsilon_0}(Z n_i - n_e), \tag{2.24}$$

and linearization of the equations. The solution of the above system yields [31] the Bohm-Gross dispersion relation for Langmuir waves:

$$\omega^2 = \omega_p^2 + k^2 c_s^2, \tag{2.25}$$

where $c_s = \sqrt{\gamma_e k_B T/m_e}$ is the electron speed of sound. The Langmuir electrostatic plasma wave is the wakefield that accelerates electrons in PWFA. The Bohm-Gross dispersion relation shows that in cold plasma ($T \to 0$) oscillations can exist and their frequency is equal to ω_p. The phase velocity of the wakefield is close to the speed of light for the relativistic driver bunch, and the group velocity of the wakefield is zero [28].

2.5 Transverse waves

Assuming low amplitude transverse waves, applying linearization and harmonic substitution $\partial/\partial t \to i\omega$, Eqs. (2.19) and (2.20) can be written as [31]

$$\nabla \times \mathbf{E}_1 = -i\omega \mathbf{B}_1, \tag{2.26}$$

$$\nabla \times \mathbf{B}_1 = \mu_0 \mathbf{J}_1 + i\varepsilon_0 \mu_0 \omega \mathbf{E}_1, \tag{2.27}$$

where $\mathbf{J}_1 = -n_0 e \mathbf{v}_1$ is the transverse current density and $\mathbf{E}_1 \ll \mathbf{E}_0$, $\mathbf{B}_1 \ll \mathbf{B}_0$, $\mathbf{v}_1 \ll \mathbf{v}_0$ are small perturbations from the equilibrium values $\mathbf{E}_0$, $\mathbf{B}_0$, and $\mathbf{v}_0$. Assuming cold plasma ($P_e = n_0 k_B T_e \approx 0$, so the wave group and phase velocities are larger than the thermal motion velocity of electrons, $v_p, v_g \gg v_{te}$), the linearized electron fluid velocity and corresponding currents are

$$\mathbf{v}_1 = -\frac{e}{i m_e \omega}\mathbf{E}_1, \tag{2.28}$$

$$\mathbf{J}_1 = \frac{e^2 n_0}{i m_e \omega}\mathbf{E}_1 = \sigma \mathbf{E}_1, \tag{2.29}$$

where σ is the alternating current electrical conductivity. Ampère's law for a dielectric medium is written as

$$\nabla \times \mathbf{B}_1 = \mu_0 \partial_t \mathbf{D}_1. \tag{2.30}$$

By analogy with Eq. (2.30) one can show that, by substituting Eqs. (2.28) and (2.29) into Eq. (2.20), the electric displacement field [31]

$$\mathbf{D}_1 = \varepsilon \varepsilon_0 \mathbf{E}_1, \tag{2.31}$$

where

$$\varepsilon = 1 + \frac{\sigma}{i\omega\varepsilon_0} = 1 - \frac{\omega_p^2}{\omega^2}. \tag{2.32}$$

From Eq. (2.32), the refractive index of plasma is

$$\eta = \sqrt{\varepsilon} = \frac{ck}{\omega} = \sqrt{1 - \frac{\omega_p^2}{\omega^2}}, \tag{2.33}$$

with

$$\omega^2 = \omega_p^2 + k^2 c^2. \tag{2.34}$$

Note the similarity of Eqs. (2.25) and (2.34). The dispersion relation shown in Eq. (2.34) demonstrates important features of EM wave propagation in plasma. If the wave frequency is larger than the plasma frequency $\omega > \omega_p$ then the phase and group velocities of that wave in plasma are:

$$v_p = \frac{\omega}{k} \approx c\left(1 + \frac{\omega_p^2}{2\omega^2}\right) > c, \tag{2.35}$$

$$v_g = \frac{\partial\omega}{\partial k} \approx c\left(1 - \frac{\omega_p^2}{2\omega^2}\right) < c. \tag{2.36}$$

If the wave frequency is smaller than the plasma frequency $\omega < \omega_p$, the wavenumber

$$k = \frac{\sqrt{\omega^2 - \omega_p^2}}{c} \tag{2.37}$$

becomes imaginary, the wave does not propagate and decays with a characteristic length that depends on the plasma collisionless skin depth $l_s = c/\omega_p$. The wave amplitude is attenuated by a factor of e over the skin depth distance.

2.6 Relativistic beam-plasma interactions

The fastest plasma response to an external perturbation is characterized by the plasma frequency ω_p, whereas the shortest distance over which the perturbation can be shielded is defined by the plasma collisionless skin depth c/ω_p. The driver beam current density $\mathbf{J}_b = q_b n_b c$ creates the opposing return plasma current $\mathbf{J}_p = e n_e \mathbf{v}_e$, where q_b is the beam particle charge, n_b is the beam charge density, n_e is the plasma density, and v_e is the plasma electrons velocity. The interaction of a charged particle beam with quasi-neutral plasma can be described as a function of the beam transverse σ_r and longitudinal σ_z rms sizes. For convenience, the beam sizes are often scaled to the plasma wavenumber $k_p = \omega_p/c$ and are denoted as $k_p\sigma_r$ and $k_p\sigma_z$. Another important parameter is the ratio of the driver beam charge density and the plasma density n_b/n_e, since it characterizes the magnitude of the initial plasma density perturbation.

Plasma wakefield acceleration. If $k_p\sigma_r, k_p\sigma_z \leq 1$, the plasma return current $\mathbf{J}_p$ flows around the particle beam and forms a bubble around it. A witness beam placed in a proper phase

$$\Delta z = (l + 1/2)\lambda_p,\ l = 1, 2, \ldots \tag{2.38}$$

behind the driver will be accelerated by the wakefields. The linear theory predicts that the maximum longitudinal electric field is [32]

$$E[\mathrm{GV/m}] \propto 96\sqrt{n_e[10^{14}\mathrm{cm}^{-3}]}. \tag{2.39}$$

Current filamentation instability. In this case, for relativistic beams with $k_p\sigma_r \geq 1$, the return plasma current $\mathbf{J}_p$ flows through the beam. Local perturbations of the

beam lead to unequal return current densities and local magnetic fields. The currents mutually interact through $\mathbf{J} \times \mathbf{B}$, increase the magnetic fields further and provide feedback for the instability growth. The beam splits transversely in separate filaments of higher densities. The size of the filaments and the distance between them is typically on the order of the plasma skin depth [33].

Self-modulation instability. When $k_p\sigma_r < 1$ and $k_p\sigma_z \gg 1$, the plasma return current $\mathbf{J}_p$ flows around the beam head and then crosses the beam axis within the beam. Low amplitude wakefields are excited, and the particles along the beam are periodically focused/defocused. As the beam transverse size and, consequently, the current density are modulated, they increase the wakefield amplitude and form a feedback mechanism for instability growth.

Sometimes the self-modulation instability is confused with the free-electron laser (FEL) instability. The FEL instability occurs when a relativistic electron beam propagating along the undulator oscillates and generates radiation. The electromagnetic field created by a single electron acts on surrounding electrons, introducing deceleration or acceleration, depending on the relative phase between the radiation and the electron oscillation. The energy modulation leads to a formation of a longitudinal electron beam density modulation (microbunching), which, in turn, results in the amplification of the electromagnetic field generated in the undulator and in the coherent emission. The modulation period corresponds to the wavelength of the emitted radiation. There is a feedback between the density modulation along the electron beam and the amplitude of the generated electromagnetic waves, which provides an exponential growth of the instability [34]. Despite having outward similarities, the self-modulation instability and the FEL microbunching instability have different feedback mechanisms and occur under different conditions. For the former, the electron beam is modulated transversely by the wakefields, while for the latter, the microbunching is formed in the longitudinal direction.

The linear PWFA theory predicts that a high amplitude plasma wakefield can be resonantly driven by a train of short ($\sigma_z < \lambda_p = 2\pi c/\omega_p$) particle beams with a spacing between bunches equal to λ_p [35] and the self-modulation instability provides a mechanism to generate such trains out of currently available long high-energy proton beams.

A practical implementation of an acceleration scheme which employs this mechanism is associated with several challenges, such as a proper witness bunch injection for an efficient utilization of the accelerating potential or a competitive growth of other beam-plasma instabilities, which can destroy the driver beam [36]. AWAKE is the first proof-of-concept experiment, the goal of which is to demonstrate acceleration of electron beams in a particle wakefield accelerator driven by self-modulated long proton beams. Several aspects of the self-modulation instability relevant in the context of its application for plasma wakefield accelerators are discussed below.

Hosing instability. Real particle beams always contain some small asymmetries or tilts due to imperfections during generation and transport of these beams. These

asymmetries can result in a transverse instability, named the hosing instability, which is coupled with a beam centroid displacement on the length of the beam with respect to the wakefield and which can result in a beam break-up. Growth rates of the self-modulation and hosing instabilities are comparable (see below). They both can start naturally from low amplitude noise or small beam imperfections.

However, if the SMI is seeded, the distance needed to saturate it shortens, and it develops completely before the hosing instability (whose seed should be minimized) effects the beam. Additionally, the seeding of the SMI allows to control the phase of wakefields. The seeding can be performed by introducing a sharp (compared to λ_p) increase of either the beam density (sharp rising edge) or plasma density (co-propagating ionization laser wavefront) [14].

The evolution of the seeded self-modulation instability growth during propagation of a relativistic electron beam in an overdense plasma are analytically described in frames of the linear theory in [14]. The evolution of the normalized electron density perturbation $\delta n/n_0 = (n - n_0)/n_0$ is

$$(\partial_\zeta^2 + 1)\delta n/n_0 = n_b/n_0, \tag{2.40}$$

where n_0 is the initial plasma density, n_b is the driver beam charge density, and $\zeta = z - ct$ is the co-moving variable. The beam-driven wakefields in terms of the normalized scalar potential $\phi = e\Phi/m_e c^2$ and normalized vector potential $\mathbf{a} = e\mathbf{A}/m_e c^2$ are [14]

$$\nabla_\perp^2 \phi = (\delta n - n_b)/n_0, \tag{2.41}$$

$$\nabla_\perp^2 a_z = v_z - (n - n_b)/n_0, \tag{2.42}$$

$$\nabla_\perp^2 \mathbf{a}_\perp = \mathbf{v}_\perp, \tag{2.43}$$

where a_z and v_z are the longitudinal components of the vector potential and the electron plasma fluid velocity, $\mathbf{a}_\perp$ is the transverse component of the normalized vector potential and $\mathbf{v}_\perp$ is the transverse component of the electron plasma fluid velocity. The (Lorentz) gauge condition is $\nabla_\perp^2 \cdot \mathbf{a}_\perp = \partial_\zeta(\phi - a_z)$. Defining the wake potential as $\psi = \phi - a_z$ and combining Eqs. (2.42) and (2.43) gives

$$(\nabla_\perp^2 - 1)\psi = \delta n/n_0, \tag{2.44}$$

the wake potential driven by the beam is

$$(\partial_\zeta^2 + 1)(\nabla_\perp^2 - 1)\psi = n_b/n_0, \tag{2.45}$$

and the force on a relativistic charged particle from the wake potential is

$$\boldsymbol{F}/(eE_0) = -\nabla\psi. \tag{2.46}$$

The general form of the seed transverse wakefield can be written as

$$(E_r - B_\theta)/E_0 = A_s f_s(r)\cos(\zeta + \varphi), \tag{2.47}$$

where A_s is the seed amplitude, $f_s(r)$ is the transverse distribution of the wakefield, φ is the time between the seed and the charged particle beam. If the seeding is done by a sharply rising front of a long charged particle beam, the transverse wakefield is

$$(E_r - B_\theta)/E_0 = -\frac{\hat{n_b}}{n_0} r_s K_1(r_s) I_1(r)(1 - \cos(\zeta + \varphi)), \tag{2.48}$$

where K_1 and I_1 are modified Bessel functions, r_s is the beam radius, the beam head is located at $\zeta = 0$ [14].

2.7 Beam evolution during seeded self-modulation

The transverse equation of motion for a single relativistic electron is

$$\frac{d^2\mathbf{x}}{dz^2} = \frac{1}{\gamma}\frac{\boldsymbol{F}}{eE_0} = \mathbf{W}_\perp, \tag{2.49}$$

where $\boldsymbol{F}$ is the force owing to the wakefileds and $\mathbf{W}_\perp$ is the transverse focusing field [14]. The beam envelope evolution describes the evolution of the rms beam transverse size $\sigma_x = \sqrt{\langle (x - x_c)^2 \rangle}$:

$$\frac{d^2\sigma_x}{dz^2} - \frac{\epsilon_x^2}{\sigma_x^3} - \frac{1}{\sigma_x}(\langle (x - x_c) W_{x,s} \rangle = -\frac{1}{\sigma_x}\frac{1}{\gamma}\langle (x - x_c)\partial_x \psi \rangle), \tag{2.50}$$

where $x_c = \langle x \rangle$, $W_{x,s} = (1/\gamma)(F_{x,s}/eE_0)$, $F_{x,s}$ is the force owing to the seed in x-direction and $\epsilon_x = \sqrt{\langle (x - x_c)^2 \rangle \langle (d(x - x_c)/dz)^2 \rangle - \langle (x - x_c) d(x - x_c)/dz \rangle^2}$ is the transverse rms geometric emittance [14]. A similar equation can be written for $\sigma_y = \sqrt{\langle (y - y_c)^2 \rangle}$. Assuming that the initial beam distribution is axisymmetric and the centroid displacement is small $x_c < \sigma_x$, the beam envelope equation can be written as

$$\frac{d^2 r_b}{dz^2} - \frac{\epsilon^2}{r_b^3} = \frac{4}{r_b}\langle (x - x_c) W_{x,s} \rangle - \frac{4}{r_b \gamma}\langle (x - x_c)\partial_x \psi \rangle, \tag{2.51}$$

where $r_b = 2\sigma_x = 2\sigma_y$ and the effective emittance is $\epsilon = 4\epsilon_x = 4\epsilon_y$.

An axisymmetric transverse beam density distribution with a small centroid offset in the x-direction can be written in general form as

$$n_b(\sqrt{(x - x_c)^2 + y^2}) \simeq n_{b0} - (\partial_r n_{b0}) x_c \cos\theta, \tag{2.52}$$

where $n_{b0} = n_b(x, y, x_c = 0) = n_b(r)$. A flattop transverse distribution can be written as

$$n_{b0} = \hat{n_b}\left(\frac{r_{b0}}{r_b}\right)^2 \Theta(r_b - r) f(\zeta), \tag{2.53}$$

where $r_{b0} = r_b(z = 0)$, Θ is the Heaviside function and $f(\zeta)$ is the normalized longitudinal profile [14].

For the general axisymmetric distribution n_{b0} of the form Eq. (2.52), the beam radius evolution equation is

$$\frac{d^2 r_b}{dz^2} - \frac{\epsilon^3}{r_b^3} = \frac{2}{\gamma r_b}\frac{\int_0^\infty r dr (n_{b0} r \partial_r \hat{\psi}_0)}{\int_0^\infty r dr (n_{b0})} + \frac{1}{\gamma} A_s \cos(\zeta + \varphi)\frac{2}{r_b}\frac{\int_0^\infty dr r^2 f_s(r) n_{b0}}{\int_0^\infty r dr (n_{b0})}. \tag{2.54}$$

Assuming a flattop transverse distribution of the form Eq. (2.53), the long beam limit, the linear focusing force provided by the seed $f_s(r) = r$, and neglecting the beam longitudinal profile ($f \approx 1$), Eq. (2.54) can be reduced to

$$\frac{d^2 r_b}{dz^2} - \frac{\epsilon^2}{r_b^3} = -\frac{k_b^2}{2\gamma} r_b \int d\zeta' \sin(\zeta - \zeta')\frac{r_{b0}^2}{r_b^2} + \frac{1}{\gamma} A_s \cos(\zeta + \varphi) r_b, \tag{2.55}$$

where $k_b^2 = \hat{n_b} e^2/m\varepsilon_0 c^2$ and $r_b(\zeta, z)$ is the beam radius.

Using Eq. (2.55), a long time scale beam radius evolution driven by the seed wakefield can be described approximately as

$$\frac{d^2 r_0}{dz^2} - \frac{\epsilon^2}{r_0^3} + k_\beta^2 r_0 \simeq \frac{1}{\gamma} A_s \cos(\zeta + \varphi) r_0, \tag{2.56}$$

where $k_\beta = k_b/\sqrt{2\gamma}$, γ is the Lorentz factor of the beam.

Consider a small perturbation of the beam radius r_1 from the slow betatron motion: $r_b = r_0 + r_1$, where $r_1 \ll r_0 \ll 1$. From the seed initial and boundary conditions, the beam radius perturbation can be found as [14]

$$\hat{r} = r_{b0} a_s e^{i\varphi} (k_\beta z)^2 \sum_{n=0}^{\infty} \frac{2(i|\zeta| k_\beta^2 z^2)^n}{n!(2n+2)!}, \tag{2.57}$$

where $a_s = (n_0/n_b)A_s$. The asymptotic solution for the beam radius perturbation $r_1 = r_b - r_{b0}$ is

$$r_1 \simeq r_{b0} a_s \left(\frac{3^{13/4}}{2^4\sqrt{2\pi}}\right)(k_\beta z)^2 \frac{e^N}{N^{5/2}} \cos\left(\frac{5\pi}{12} - \zeta - \frac{N}{\sqrt{3}} - \varphi\right), \tag{2.58}$$

where N is the number of e-foldings for the self-modulation instability [32]:

$$N = (3^{3/2}/4)(2|\zeta| k_\beta^2 z^2)^{1/3}. \tag{2.59}$$

In conclusion, the radius of a beam influenced by self-modulation instability is modulated sinusoidally along the bunch length. The modulation amplitude grows exponentially along the bunch (ζ) and with increasing propagation distance (z) through the plasma. This growth is restricted, and saturation will occur after some propagation distance which is not described by this theoretical model. The instability saturates due to nonlinear effects which occur at high wakefield amplitudes and which result in a dephasing between the beam and the wakefield and, therefore, a break-up of the instability feedback mechanism [37].

2.7.1 Hosing instability

In presence of the seed wakefield, the beam centroid x_c evolution equation is [14]

$$\frac{d^2x_c}{dz^2} = \frac{1}{\gamma}\left\langle \frac{F_x}{eE_0} \right\rangle = \frac{1}{\gamma}\left\langle \partial_x \psi \right\rangle + \left\langle W_{x,s} \right\rangle . \tag{2.60}$$

The beam centroid evolution can be found by averaging the transverse force over the general transverse distribution (Eq. (2.52)):

$$\begin{aligned} &\frac{d^2x_c}{dz^2} + \frac{x_c}{\gamma}\frac{\int_0^\infty rdr(\partial_r n_{b0})(\partial_r \hat{\psi}_0)}{2\int_0^\infty rdr(n_{b0})} + \frac{x_c}{\gamma}A_s\cos(\zeta+\varphi)\frac{\int_0^\infty rdr(\partial_r n_{b0})f_s(r)}{2\int_0^\infty rdr(n_{b0})} = \\ &= \frac{1}{\gamma}\frac{\int_0^\infty dr(n_{b0})[\partial_r(r\hat{\psi}_1)]}{2\int_0^\infty rdr(n_{b0})}. \end{aligned} \tag{2.61}$$

For a flattop distribution (Eq. (2.53)), Eq. (2.61) can be written as

$$\begin{aligned} &\frac{d^2x_c(\zeta)}{dz^2} = A_s\cos(\zeta+\varphi)f_s(r_b)\frac{x_c}{r_b} + \frac{k_b^2}{\gamma}\frac{I_1(r_b(\zeta))}{r_b(\zeta)}\int_\infty^\zeta d\zeta\prime \sin(\zeta-\zeta\prime)\times \\ &\times f(\zeta\prime)\frac{r_{b0}^2}{r_b(\zeta\prime)}K_1(r_b(\zeta\prime))[x_c(\zeta\prime)-x_c(\zeta)]. \end{aligned} \tag{2.62}$$

Assuming a flattop transverse distribution (Eq. (2.53)), a linear focusing field due to the seed wakefield $f_s(r) = r$, and a narrow beam limit ($r_b \ll 1$) , the centroid evolution due to the seed can be written as [32]

$$\frac{d^2x_c}{dz^2} = \frac{k_b^2}{2\gamma}\int d\zeta\prime \sin(\zeta-\zeta\prime)\frac{r_{b0}^2}{r_b^2}[x_c(\zeta\prime)-x_c(\zeta)] + \frac{1}{\gamma}A_s\cos(\zeta+\varphi)x_c. \tag{2.63}$$

Consider a long beam initially displaced with respect to the seed wakefield axis $x_{c0} = x_c(z=0,\zeta)$. Using Eq. (2.63), the centroid evolution is

$$\left[\frac{d^2}{dz^2} - \frac{1}{\gamma}\frac{f_s(r_b)}{r_b}A_s\cos(\zeta+\varphi)\right]x_0 = 0. \tag{2.64}$$

The approximate solution for early times ($k_\beta z \ll 1$) is [14]

$$x_0 \approx x_{c0}\left[1 + a_s\cos(\zeta+\varphi)(k_\beta z)^2\right]. \tag{2.65}$$

Consider a small centroid displacement x_1 describing the hosing instability: $x_c = x_0 + x_1$. Assuming that the hosing growth length is much shorter than the betatron scale length $|\partial_z x_1| \gg k_\beta |x_1|$ and the initial and boundary conditions defined by the seed wakefield, the beam centroid perturbation can be found as [14]

$$\hat{x} = x_{c0} a_s e^{i\varphi} (k_\beta z)^2 \sum_{n=0}^{\infty} \frac{2(i|\zeta| k_\beta^2 z^2/2)^n}{n!(2n+2)!}. \tag{2.66}$$

The asymptotic solution for the beam centroid displacement $x_1 = x_c - x_{c0}$ is

$$x_1 \simeq x_{c0} a_s \left(\frac{3^{13/4}}{2^4 \sqrt{2\pi}} \right) (k_\beta z)^2 \frac{e^{N_h}}{N_h^{5/2}} \cos\left(\frac{5\pi}{12} - \zeta - \frac{N_h}{\sqrt{3}} - \varphi \right), \tag{2.67}$$

where N_h is the number of e-foldings for the hosing instability [38]:

$$N_h = (3^{3/2}/4)(|\zeta| k_\beta^2 z^2)^{1/3}. \tag{2.68}$$

As the self-modulation and hosing instabilities have similar growth rates, the seed for the later should be minimized, i.e., the initial centroid displacement with respect to the seed wakefield should be much smaller than the beam radius $x_{c0} \ll r_{b0}$. The hosing instability will develop even after the saturation of the SMI and eventually the hosing could be a limiting factor for the plasma accelerator stage length.

2.7.2 Phase velocity of the SMI and mitigation of the phase slippage

Although dephasing is usually not an issue for beam-driven plasma accelerators, the phase velocity of the plasma wave during the development of the SMI is substantially lower than that of the driver beam due to the instability dispersion [32, 39]. An analytical expression for the Lorentz factor γ_p of the wake is given in [32]:

$$\gamma_p = \left(\frac{\gamma n_0 M_b}{v n_{b0} m_e} \frac{z}{|\zeta|} \right)^{1/6}, \tag{2.69}$$

where γ is the Lorenz factor of the driver beam, n_0 is the plasma density, M_b is the driver particle mass, m_e is the electron mass, n_{b0} is the initial peak density of the driver, $\zeta = z - ct$ is the co-moving variable, and $v \simeq 1 - (k_p r_0)^2/6$ for a narrow beam $k_p r_0 \ll 1$, where r_0 is the beam radius and k_p is the plasma wavenumber. The wake factor γ_p can be orders of magnitude less than that of the driver, but once the SMI is saturated, the wake phase velocity catches up with that of the driver. It was shown analytically that the reduced phase velocity of the SMI wake can be compensated by plasma density tapering: a witness bunch can be phase locked (i.e. can be kept in the accelerating phase of the wake) by introducing the plasma density taper in form of $\hat{k_p} = 1 + \eta \hat{z}^{2/3}$ [40]. The number of e-foldings for the self-modulation instability is $\Re(N_t)$, where N_t is

$$N_t = \frac{3}{4}(i + \sqrt{3}) \left[2\hat{k}_b^2 \left| \hat{\zeta} \right| \left(\int_0^{\hat{z}} \hat{k}_p^{1/2} d\hat{z} \right) \right]^{1/3}. \tag{2.70}$$

However, the instability growth can be suppressed by plasma density inhomogeneities. For plasma density profile $n_0(z) = n_0(0)\,[1 + \Delta n_f \sin(k_f z)]$ (where n_f is the fluctuation amplitude, k_f is the fluctuation wavenumber), a for a short density fluctuation period ($k_f z > 1$) the instability growth will be suppressed for $\eta \gtrsim (\hat{k_b}/\hat{\zeta})^{1/3}$ due to decoherence between the beam head and tail [40]. It was shown in numerical simulations that the self-modulation instability will be suppressed by the density fluctuation amplitude several times higher than the theoretically predicted cutoff value [41].

Numerical studies [42] have shown that a sharp density increase (step) introduced in plasma at the linear stage of the instability growth can decrease dephasing and result in a higher established wakefield amplitude after the development of the instability. Another possible solution is to avoid the dephasing issue by injecting the witness bunch into the plasma having the SMI already saturated. That could be achieved by means of a multi-staged scheme [32].

Chapter 3

PITZ facility

The Photo Injector Test facility at DESY in Zeuthen (PITZ) is an R&D facility developing, characterizing and optimizing high brightness electron sources for free electron laser (FEL) applications. One of the main tasks at PITZ is to demonstrate the reliable operation of electron sources meeting the requirements for the European X-ray Free Electron Laser (European XFEL or just XFEL). This includes the demonstration of a normalized projected transverse emittance lower than 1 mm mrad for a 1 nC electron bunch from the electron source with a low momentum spread [43] and the confirmation that the electron source can be stably operated at nominal parameters in long-term conditions. At XFEL, the electron source (a photocathode RF gun) should operate reliably at a high average RF power. For different gun setups, studies have shown that the projected transverse emittance even below the XFEL specification can be produced at PITZ [44] and that the latest PITZ gun setups can fulfill the XFEL reliability requirements [45].

This chapter describes the basic layout of PITZ (see Fig. 3.1) and its diagnostic equipment related to the self-modulation experiment.

3.1 Photoinjector laser system

The photocathode laser was developed and built for PITZ by the Max Born Institute, Berlin. Its key feature is a pulse shaper [46] – a set of 13 motorized birefringent crystals which allows to transform an initial short Gaussian pulse (about 2 ps FWHM) to a flat-top temporal profile with short rise and fall times, defined by the fundamental pulse length, and a pulse length of up to 24 ps FWHM (Fig. 3.2). The laser system consists of an Yb:KGW oscillator ($\lambda \approx 1030$ nm), the pulse shaper, Yb:KGW amplifier stages, two conversion crystals to obtain UV output ($\lambda \approx 257$ nm), a transport beamline and diagnostic devices [47]. The temporal profile of the laser pulses can be measured with the optical sampling system (OSS) – a setup which uses the principle of a cross correlator and scans UV laser pulses by means of short probe laser pulses [47]. In the current configuration, the laser system generates pulse trains with a repetition

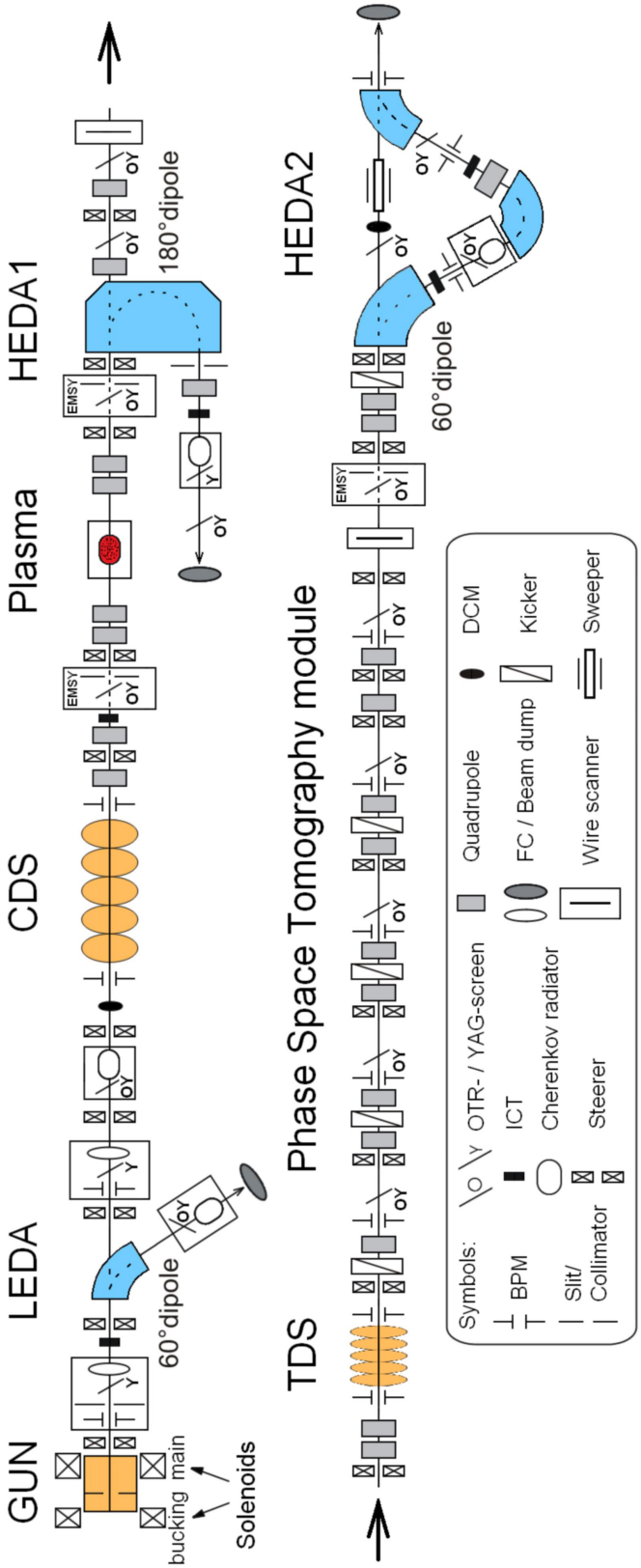

Figure 3.1: A schematic layout of the PITZ beamline. Based on Fig. 3.1 from [51].

rate of 10 Hz and up to 600 pulses per pulse train. The spacing of the pulses within the pulse train is 1 µs. The laser is synchronized with a master oscillator which also provides the timing signals for the RF stations. The output pulse energy can be attenuated by means of a $\lambda/2$ plate installed on a motorized rotation stage and a subsequent birefringent crystal to separate the polarizations spatially. The laser beam is transported to the PITZ tunnel by a transport beamline which is about 25 m long. The transverse beam distribution is Gaussian, and a central uniform part of the transverse profile is cut out by a variable size beam shaping aperture (BSA) before being imaged onto the photocathode. The transverse laser distribution is observed with a JAI RM1405 CCD [48] camera, which is specially modified for UV imaging (the microlens array which is normally found in front of the CCD chip, was not installed during manufacturing). This camera is installed after the BSA at the same distance as the photocathode and thus named Virtual Cathode (VC2). The laser beam position on the last (in-vacuum) mirror and on the photocathode can be adjusted by a pair of remotely controlled mirrors installed after the BSA. The laser pulse energy is measured with a laser pulse energy meter [49], and the position jitter is measured with a quadrant diode [50].

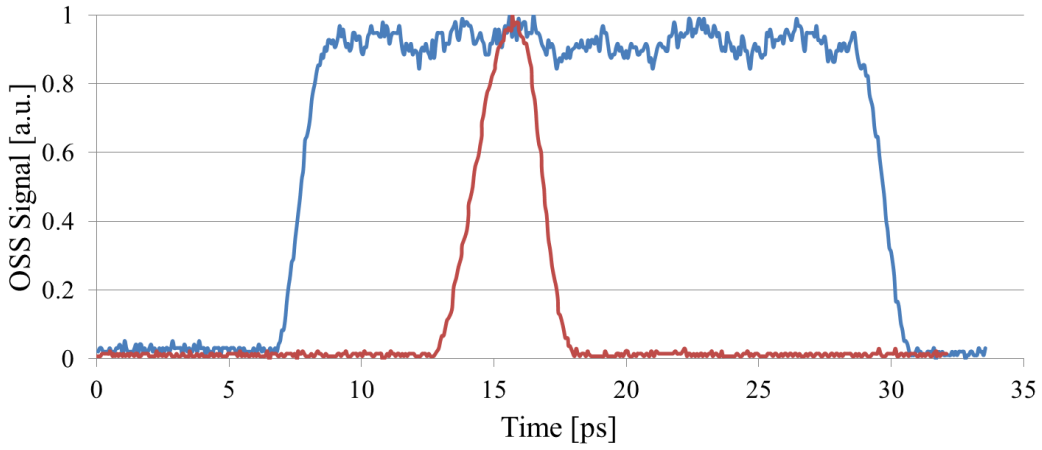

Figure 3.2: Photoinjector laser profiles measured with the OSS: the fundamental Gaussian laser pulse (red) and the long flattop obtained with the pulse shaper (blue).

3.2 Gun

The PITZ gun is a 1.6 cell L-band RF normal-conducting cavity (Fig. 3.3), and it is operated nominally with a 60 MV/m acceleration gradient at the cathode and at high average RF power (6.5 MW peak power in the gun for 650 µs RF pulse length at 10 Hz repetition rate) [45]. The gun is surrounded by two solenoids: the main solenoid focuses the extracted electrons and controls the evolution of the electron beam, while

the bucking solenoid compensates the main solenoid magnetic field on the cathode plane to minimize the contribution of the induced angular momentum to the beam emittance. The RF power from a 10 MW klystron is fed through a waveguide system with two vacuum RF windows and an in-vacuum T-combiner, and a 10 MW directional coupler [45]. A photocathode is inserted from the backside of the gun by means of a special in-vacuum actuator. The molybdenum photocathode plug is coated with a thin photoemissive layer of Cs_2Te on the front surface. At the nominal conditions, the gun accelerates electrons to a momentum of 6.5 MeV/c. The gun prototype 4.6 (Gun4.6) was installed at PITZ during the SMI experiments described in this work.

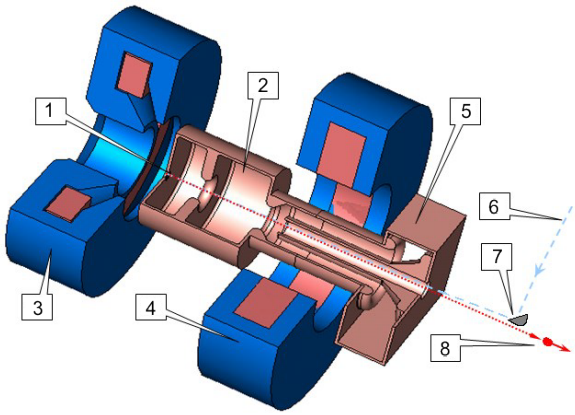

Figure 3.3: PITZ gun layout. 1 – photocathode, 2 – 1.6-cell copper RF cavity, 3 – bucking solenoid, 4 – main solenoid, 5 – coaxial RF coupler, 6 – trajectory of the incoming laser beam, 7 – in-vacuum laser mirror, 8 – trajectory of the generated electron beam. Source: [51].

3.3 Booster

The second accelerating cavity is located about 3 m downstream of the cathode plane. It is a 14 cell cut disk structure RF cavity designed by the Institute for Nuclear Research (INR RAS, Troitsk, Russia) and built by DESY Hamburg [52]. Typical beam momentum gain in the booster is 15 MeV/c (corresponding peak RF power in the cavity is 3.5 MW). The beamline section upstream of the booster usually is referred to as the low energy section and the beamline downstream of the booster is referred to as the high energy section.

3.4 Transverse deflecting structure

The transverse deflecting structure (TDS) is used for the characterization of the longitudinal properties of electron beams. The PITZ TDS was designed and built by

the Institute for Nuclear Research (INR RAS, Troitsk, Russia) as a prototype of the TDS for the European XFEL injector section [51, 53]. It is a 16 cell traveling wave copper structure which runs at 3 GHz. The deflecting voltage is up to 1.7 MV/m, and the pulse length is 3 µs. This allows to deflect up to three bunches from the bunch train. The practically achievable temporal resolution for the cavity is below 200 fs [54].

The electron beam passing through the TDS is subjected to the action of transverse electric and magnetic fields. As the electron beam co-propagates with the traveling wave, it sees a constant phase of the transverse force. The deflection of each longitudinal slice of the beam can be estimated for the case that the TDS RF wavelength is much longer than the electron beam length and the center of the electron beam passes through the cavity at the zero RF phase (i.e., is subjected to zero transverse force). In that scenario, the deflecting angle (or vertical transverse position on an observation screen) of each electron linearly depends on its longitudinal position with respect to the beam center.

In general case, the resolution of a TDS is given by the inequality [51, 55]

$$\sigma_z \geq \frac{\sqrt{\varepsilon_y}}{\sqrt{\beta_y(s_0)\sin(\Delta\psi_y)}} \cdot \frac{pc}{eV_o k}, \tag{3.1}$$

where σ_z is the minimum resolvable distance between two slices on the observation screen, ε_y is the vertical geometrical emittance at the observation screen position, $\beta_y(s_0)$ is the vertical beta function at the TDS center, $\Delta\psi_y$ is the vertical beta function phase advance between the TDS center and the observation screen, p is the beam longitudinal momentum, V_0 is the deflecting voltage amplitude, and k is the wave number, $k = 2\pi f/c$, f is the RF frequency. The higher the deflecting voltage and the beam beta function in the TDS are, the better longitudinal resolution can be achieved. A more straightforward estimation of the resolution is useful for the measurements [51]:

$$\sigma_z \geq \frac{\sqrt{\beta_y(s)\varepsilon_y}}{S} \quad \text{or} \quad \sigma_z \geq \frac{\sigma_y}{S}, \tag{3.2}$$

where $\beta_y(s)$ is the beam beta function at the observation screen position, σ_y is the vertical rms size of the beam on the observation screen and S is the TDS shear parameter. The shear parameter can be measured in the experiment during the so-called TDS calibration [51]. The TDS calibration is a measurement of the mean vertical position of a streaked beam on the observation screen as a function of the TDS RF phase. The shear parameter is then obtained from a linear fit of the measured data:

$$S = a\frac{2\pi f}{\beta c}, \tag{3.3}$$

where a is the first order term of the fit (the slope of the linear fit) and βc is the electron bunch velocity.

An important aspect of the TDS is the induced momentum spread. The principle of the TDS is based on the Panofsky-Wenzel theorem which states that transverse acceleration occurs whenever there is a transverse variation of the longitudinal accelerating field [56]:

$$\frac{\partial}{\partial z}\mathbf{F}_{\perp} = -\nabla_{\perp}\mathbf{F}_{\parallel}, \tag{3.4}$$

where $\mathbf{F}_{\perp}$ and $\mathbf{F}_{\parallel}$ are the transverse and longitudinal forces. The longitudinal electric field is 0 only on the axis of the TDS, and the electrons which travel through the cavity off axis will be subjected to the longitudinal electric field. Similarly to the resolution (Eq. (3.2)), the relative induced momentum spread σ_{δ} also depends on the applied deflecting voltage V_o and the rms vertical beam size inside the TDS σ_y [51]:

$$\sigma_{\delta} = \frac{eV_0 k}{pc}\sigma_y. \tag{3.5}$$

Figures 3.4 and 3.5 show the resolution and the induced energy spread for several vertical rms beam sizes inside the TDS as a function of the deflecting voltage. For these illustrations the RF frequency f is 3 GHz, beam momentum p is 23 MeV/c, phase advance $\Delta\psi_y$ is 110° and geometrical vertical emittance ε_y is 1 mm mrad – these parameters correspond to the PITZ beam parameters without interaction with plasma.

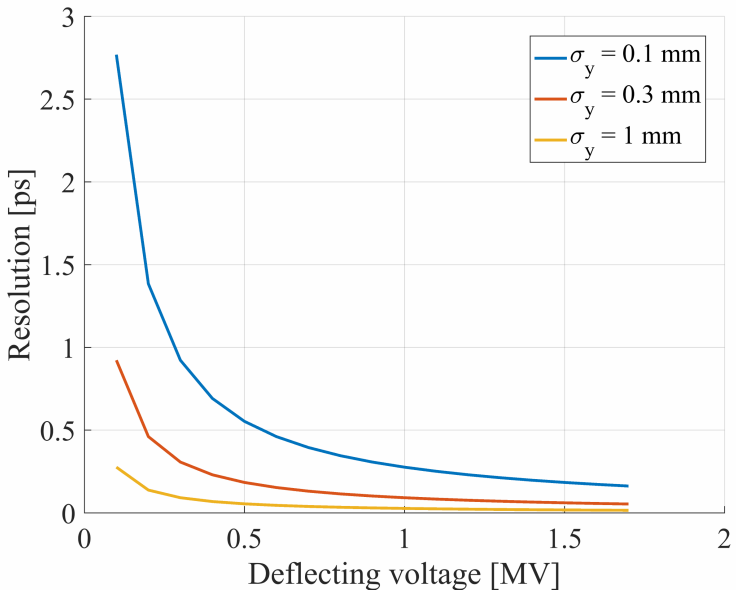

Figure 3.4: The longitudinal TDS resolution as a function of the TDS deflecting voltage and the vertical beam size in the TDS.

For $1 \times 10^{15}\,\mathrm{cm}^{-3}$ plasma density, the plasma wavelength and, consequently, the modulation period of the self-modulated beam are equal to 1 mm or 3.3 ps. For lower

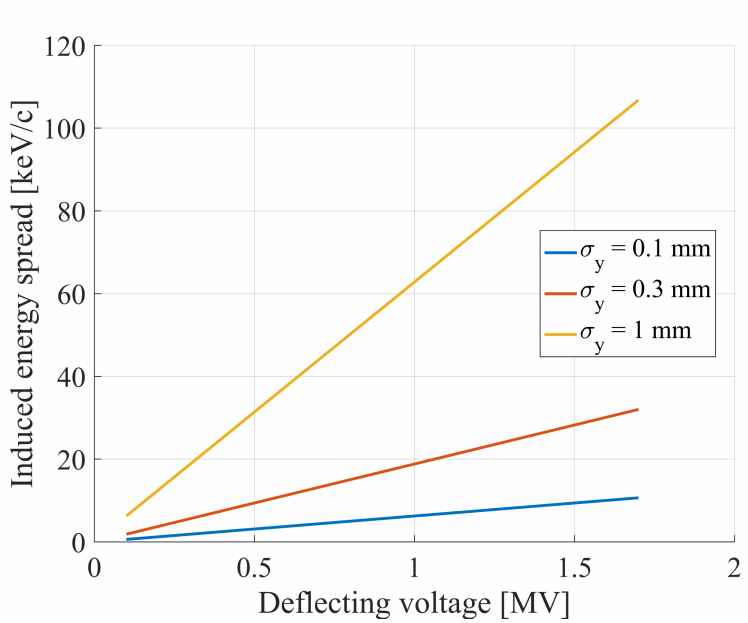

Figure 3.5: The induced longitudinal momentum spread as a function of the TDS deflecting voltage and the vertical beam size in the TDS.

plasma densities the modulation period is larger. However, measurements of some features of the self-modulation instability, such as the phase slippage (see Chapters 2 and 6), could require temporal resolution of 1 ps and better. These resolutions are achievable for a broad range of the TDS deflecting voltages. Simulations [57] predict the maximum peak-to-peak momentum spread for a self-modulated beam at PITZ of about 1 MeV/c, therefore the induced momentum spread is not large enough to interfere with the momentum measurement of the modulated beam.

3.5 Beam optics

Twenty corrector dipole magnets (steerers) are installed along the PITZ beamline. Their function is to adjust the beam trajectory, to guide the beam through small apertures and to position it properly at the measurement stations. There are twenty-one quadrupole magnets installed in the high energy section, and two more are installed in HEDA1 and HEDA2 (see below). All quadrupoles along the straight beamline are of the same type, manufactured and measured by DANFYSIK [58]. They are powered independently from power supplies with a maximum current of 12 A, and their maximum gradient is about 7.5 T/m. Due to PITZ space restrictions, the quadrupoles are very compact, with an average effective length of 0.043 m and a bore radius of 0.02 m. More details are available in [59]. For the self-modulation experiment, quadrupole magnets provide tight focusing of the electron beam into the plasma cell and onto

measurement screens.

3.6 Dipole spectrometers

There are three dipole sections along the beamline: one in the low energy section, named Low Energy Dispersive Arm or LEDA, and two in the high energy section – High Energy Dispersive Arms 1 and 2 (HEDA1 and HEDA2). They are used for momentum and momentum spread measurements, as well as for longitudinal phase space characterization. The LEDA dipole is a 60° bending magnet located about 1 m downstream of the gun cavity. HEDA1 (Fig. 3.6) consists of a 180° dipole with a bending radius of 0.3 m and is installed about 7 meters downstream of the gun.

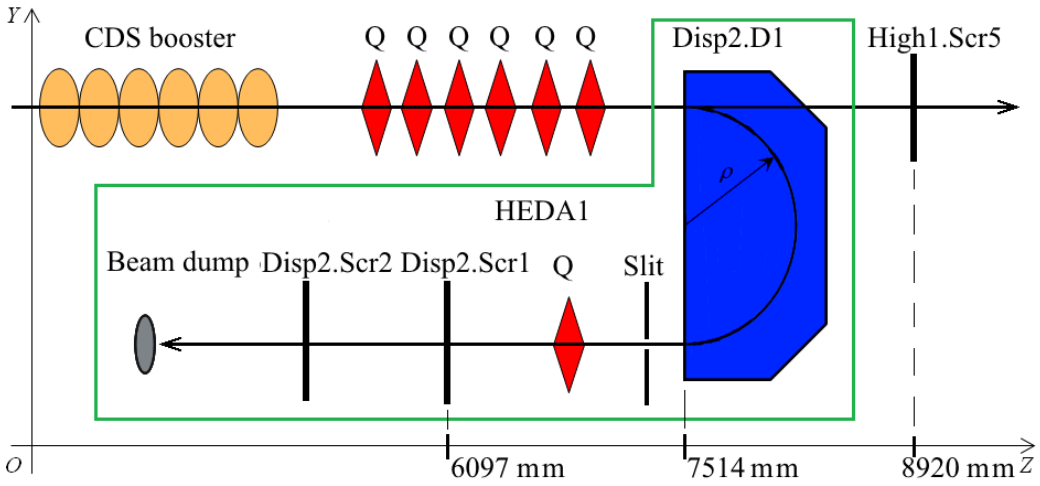

Figure 3.6: HEDA1 setup. The electron beam comes from the left side. The bending radius ρ is 0.3 m. Based on an illustration from [51]; the quadrupole setup in the main beamline was changed.

The HEDA2 section was designed and built in collaboration between DESY and Laboratoire de l'Accélérateur Linéaire (LAL, Orsay, France). It includes three magnets: 60° entrance and exit sector magnets and a 120° sector magnet with exit wedge angle in the middle, but only the first magnet is used for momentum measurements (Fig. 3.7). HEDA2 is designed for beam momentum measurements up to 40 MeV/c with a momentum spread resolution better than 1 keV/c [60]. The observation screen for the longitudinal phase space measurement at HEDA2 is the Disp3.Scr1 screen and it is located about 70 cm downstream of the entrance dipole.

In a dipole spectrometer, the final position of a particle on an observation screen is

$$x = x_0 \left(\cos\theta - \frac{L}{\rho} \sin\theta \right) + x'_0 \left(L \cos\theta + \rho \sin\theta \right) + \delta p \cdot D, \tag{3.6}$$

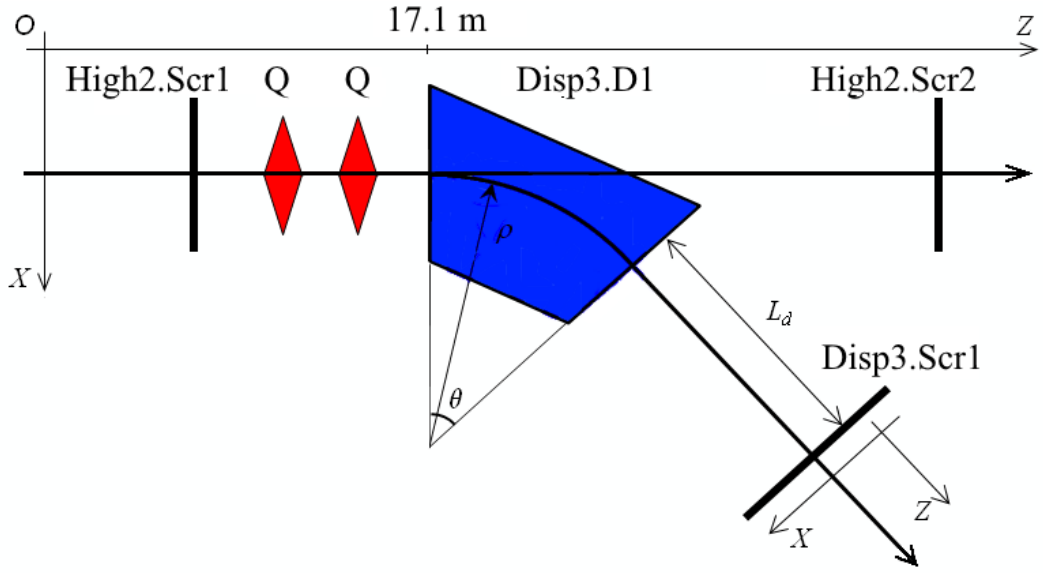

Figure 3.7: Entrance dipole of the HEDA2 setup. Electron beam comes from the left side. The bending radius ρ is 0.6 m. The distance L_d to the observation screen Disp3.Scr1 is 0.6994 m. Based on an illustration from [51].

where θ is the dipole bending angle, ρ is the bending radius, L is the drift distance between the dipole and the observation screen, δp is the relative particle momentum with respect to the reference particle and D is the dipole dispersion. The first two terms of Eq. (3.6) describe the dependence of the final particle position on its position and divergence at the dipole entrance, and the last term is the contribution of the relative particle momentum to its final position on the observation screen. For the HEDA1 measurement, $\theta = 180°$, so Eq. (3.6) can be written as

$$x = x_0 + x'_0 \cdot L + \delta p \cdot D. \tag{3.7}$$

The sign before the second term of Eq. (3.7) is flipped with respect to Eq. (3.6) in order to keep the same direction on the x axis.

To minimize the influence of the first two terms in this equation for all particles, the electron beam is centered and focused horizontally on the reference screen High1.Scr5 which is installed in the straight section of the beamline on the same distance L downstream of the dipole as the measurement screen Disp2.Scr1 in the dipole arm. The relative HEDA1 momentum measurement resolution is estimated as $\delta p \geq \sigma_y / D$. For this magnet, $D = 0.6$ m and σ_y is the vertical rms size on the reference screen High1.Scr5. For $\sigma_y = 0.5$ mm the relative measurement resolution is 8.3×10^{-4} which gives an absolute resolution of 19 keV/c for $p = 23$ MeV/c. The HEDA2 dipole bending angle is 60°. To achieve the best momentum resolution, one needs to minimize the first two terms of Eq. (3.6) for all particles:

$$\left| x_0 \left(\cos\theta - \frac{L}{\rho} \sin\theta \right) + x_0' \left(L\cos\theta + \rho \sin\theta \right) \right| < |\delta p \cdot D| \,. \tag{3.8}$$

There is no reference screen for Disp3.Scr1, so the electron beam is simply focused with quadrupole magnets upstream of the HEDA2 dipole in such a way that the horizontal beam size on Disp3.Scr1 is the smallest. This allows to achieve the best optical resolution [51].

3.7 Charge measurement

Six integrating current transformers (ICTs) manufactured by Bergoz [61] are installed along the PITZ beamline: one in the low energy section, two in the straight part of the high energy section, one in HEDA1 and two in HEDA2. The ICTs are nondestructive measurement devices and allow to monitor beam charge continuously; however, the installed devices are not sensitive enough to reliably measure charges lower than 100 pC (they were designed for bunch charges of 1 nC). In addition to the ICTs, two in-house built Faraday cups are installed in the low energy section. They allow to measure beam charges down to fractions of pC. However, when inserted in the beamline, they block the beam.

3.8 Screen stations

The transverse beam distribution and the transverse beam position can be measured on a number of screen stations along the PITZ beamline. Most of the stations are equipped with Optical transition radiation (OTR) screens and Cerium doped Yttrium-Aluminum Garnet powder coated (Ce:YAG) screens [62]. The OTR screens are suitable for high-energy and high-intensity beams, while YAG screens are more sensitive and saturate more easily. Only YAG screens were employed in the SMI experiment. The following screens were directly used in the measurements: HIGH1.Scr5 (downstream of the plasma cell), PST.Scr1 (downstream of the TDS), DISP2.Scr1 (in the HEDA1 section) and DISP3.Scr1 (in the HEDA2 section). All screen stations along the beamline were used to tune the beam trajectory in preparation for and during the experiment. 90° and 45° screen orientations with respect to the beam are used at PITZ. In case of the 90° mounting, a 45° mirror mounted behind the screen is used to deflect light to the camera, as shown in Fig. 3.8 [63].

Each screen station is equipped with a lens and CCD camera for readout. Usually, there are two interchangeable lenses – one for a whole screen and one with a greater magnification for a region of interest. All CCD cameras installed in the beamline are Allied Vision Technologies (AVT) Prosilica GC1350M [64]. These are 1.4 Mpx monochrome 12-bit cameras. They support binning modes – a combination of 2×2 or 4×4 adjacent pixels into one pixel. This increases the signal to noise ratio and

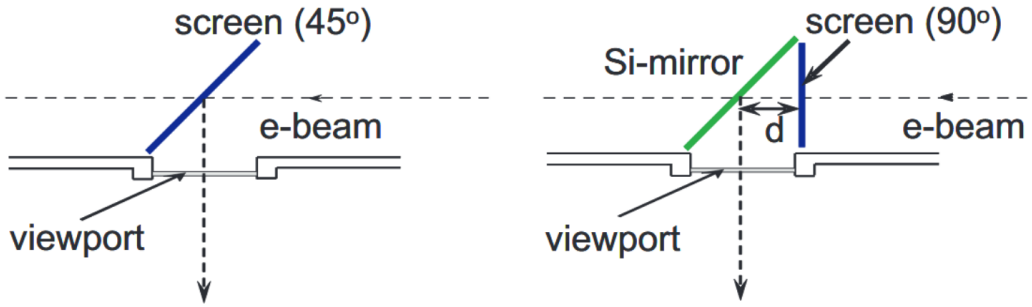

Figure 3.8: Screen orientations at PITZ screen stations: 45° (left) and 90° (right). Illustration is taken from [62].

readout speed but decreases the image resolution. At PITZ, the 2×2 binning option is usually enabled for all cameras. During measurements, captured images are averaged and undergo processing in order to reduce background noise [59]. Scaling parameters of the screens are listed in Table 3.1.

Table 3.1: Parameters of PITZ screen stations used in this work. The scale factor is given for the 2×2 binning mode.

Screen station	Screen orientation	Focal length of the lens [mm]	Scale [µm/px]	Comment
High1.Scr5	90°	100 160 250	76.1 38.2 12.4	HEDA1 reference screen
Disp2.Scr1	45°	50 120	116.7 35.3	HEDA1 observation screen
PST1.Scr1	90°	140 200	76.1 44.4	TDS measurements screen
Disp3.Scr1	90°	80 200	127.7 37.3	HEDA2 observation screen

3.9 Vacuum system

The PITZ beamline was upgraded in order to accommodate the self-modulation experiment. Quadrupole magnets were repositioned in order to provide optimal focusing to and after the plasma cell (see Chapters 4 and 6). A special frame was built at the

HIGH1.Scr2 position. This frame includes a slot for the plasma cell installation and a vacuum bypass which connects the vacuum beamline before and after the plasma cell. Two pressure gauges are installed close to the plasma cell to monitor the vacuum level around the plasma cell during operation. The frame also allows installation of the High1.Scr2 station, or a simple beamline tube when the plasma cell is out. Figure 3.9 shows a CAD model of the beamline section around the plasma cell.

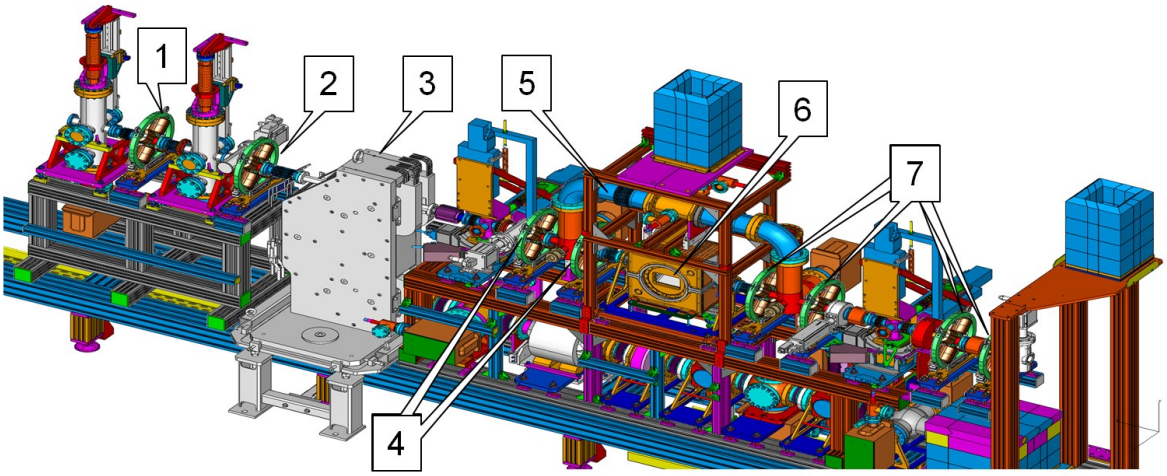

Figure 3.9: PITZ beamline around the plasma cell position. 1 – quadrupole magnet High1.Q8, 2 – High1.Q7, 3 – HEDA1 dipole, 4 – High1.Q6 and High1.Q5, 5 – vacuum bypass, 6 – plasma cell (see Chapter 4), 7 – High1.Q1-High1.Q4.

Chapter 4

Plasma cell and pre-experiments

Initial parameters for the self-modulation experiment were derived from the simulation results (see Section 6.1) and design considerations. In order to obtain missing parameters, a set of preliminary experiments was conceived and conducted. The studies were focused on the plasma source and the beam parameters for the self-modulation experiment. There are two generations of the lithium vapor plasma cells at PITZ. For both, the mechanical design was done by Gerald Koss, and they were manufactured at the mechanical workshop at DESY, Zeuthen site. The first plasma cell was installed in the PITZ tunnel in the autumn of 2015, but the experiment was quickly interrupted due to technical issues. The goal of the second design was to improve the overall stability of the plasma cell operation and its parameters, most importantly the plasma density.

4.1 Heat pipe oven plasma cell

In a heat pipe oven plasma source the plasma is generated by ionization of a working medium in a gas loaded heat pipe. Heat pipes are devices which employ the phase transition to transport large quantities of heat. In a heat pipe, a gaseous phase of the working medium flows from the evaporator (hot zone) to the condenser or heat sink (cold zone), cools down and condenses to a liquid phase and flows back to the heater. The liquid transport is assisted by capillary forces generated in a wick structure (Fig. 4.1). In the gas-loaded heat pipe (sometimes called the gas-controlled heat pipe), a working medium vapor is confined by a buffer gas to the central part of the heat pipe, limiting the effective area of the condenser zone. Due to the gas-loaded heat pipe nature [65], the working medium vapor density remains nearly constant along the heat pipe and is defined by the evaporator temperature. The heat pipe working medium in the gaseous phase is ionized by an external laser.

The PITZ plasma cell design is inspired by the SLAC lithium oven plasma source [67]. A goal plasma density of $1 \times 10^{15}\,\mathrm{cm}^{-3}$ was suggested for the experiment at PITZ [57]. This density corresponds to the plasma wavelength λ_p of approximately 1 mm, while the PITZ electron beam length is about 7 mm, so the number of

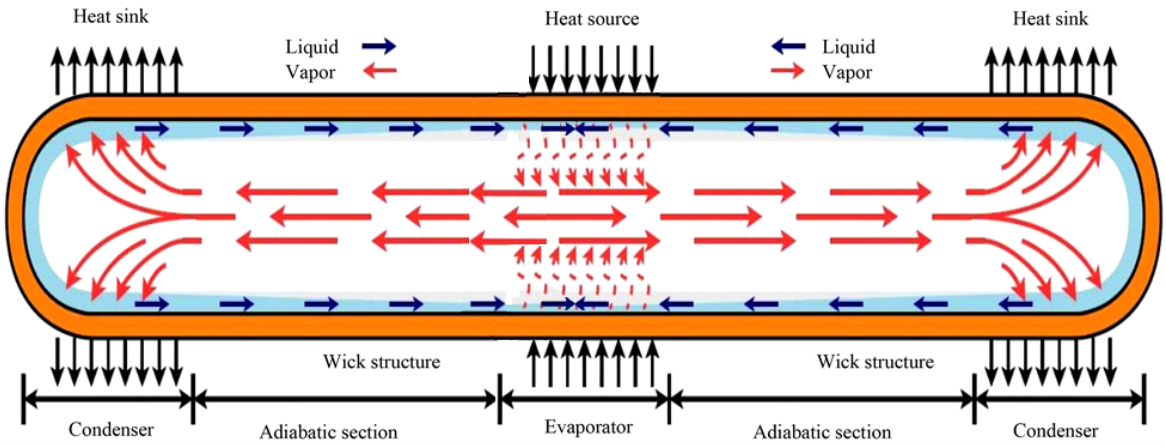

Figure 4.1: Schematic of a heat pipe. Based on Fig. 1 from [66].

modulations along the electron beam is high enough for a detailed study of SMI features and, at the same time, the modulated bunch structure at that scale can be reliably resolved by the PITZ beam diagnostics. Heat pipe ovens are long known as sources of homogenous metal vapor [68]; successful operation at the desired plasma density for that type of plasma sources was already demonstrated [67].

The SLAC source uses a plasma ionization scheme with a coaxially coupled ionization laser, however, due to space restrictions only a side ionization scheme is possible at PITZ (Fig. 4.2). A conceptually similar prototype of a side-ionized, cross-shaped plasma source was developed in Bernhard Hidding's group in the University of Hamburg [69]. Several alternate optical configurations of the side ionization for the PITZ plasma cell were studied during the design of the experiment [70]. The single photon ionization by a pulsed 193 nm laser was chosen for plasma generation [71].

The working medium for the PITZ plasma source is lithium, as at SLAC, whereas the working medium at AWAKE is rubidium[1] [72]. Although rubidium has several advantages – a lower melting point (and, correspondingly, a lower temperature needed to achieve a given vapor density) and lower ionization potential, – the ionization cross section of lithium is substantially higher, which is favorable for the single photon ionization scheme. The much higher absorption length in rubidium would decrease the ionization rate by more than an order of magnitude. Table 4.1 gives an overview of rubidium and lithium properties related to the experiment. Lithium is an alkali metal with very high chemical activity; it reacts quickly with air components. Special procedures for lithium handling and for removing products of chemical reactions with lithium were developed (Appendix A). Following these procedures is necessary for the

[1]The AWAKE plasma source is not a heat pipe oven (the vapor density is maintained constant not by a heat pipe, but by a sophisticated heater), but the same ionization mechanism is employed.

stable performance of the heat pipe, and therefore the plasma source in whole.

Adjusting the heat pipe evaporator temperature allows to set a desired working point on the vapor pressure curve (Fig. 4.3). For the desired plasma density of about $1 \times 10^{15}\,\mathrm{cm}^{-3}$, taking into account the ionization rate of lithium vapor, the optimum vapor density is in the range from few times $1 \times 10^{15}\,\mathrm{cm}^{-3}$ to few times $1 \times 10^{16}\,\mathrm{cm}^{-3}$ [71] which corresponds to an operational temperature range from 700 to 800 °C.

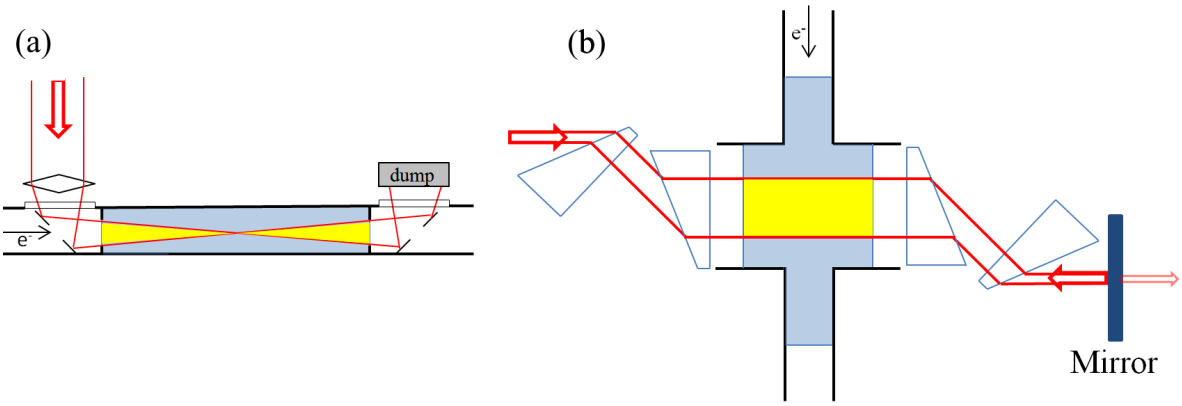

Figure 4.2: Ionization schemes: (a) coaxial ionization; (b) side ionization. Neutral metal vapor is shown in light blue, plasma is shown in yellow. In panel (b) a double pass scheme is shown: the laser travels from the left side and is reflected back by a mirror, increasing the ionization rate. Two prism pairs allow to stretch the laser beam and extend the length of the plasma channel. For the description of the side ionization scheme used at PITZ, refer to [70].

Table 4.1: Selected properties of lithium and rubidium. Data is taken from [73, 74]

	Melting point [°C]	Ionization energy [eV]	Ionization cross section at $\lambda = 193\,\mathrm{nm}$ [Mb]	Maximum ionization cross section	Vapor density $1 \times 10^{16}\,\mathrm{cm}^{-3}$ at
Rb	39.5	4.18	0.06	0.14 Mb at $\lambda = 120\,\mathrm{nm}$	270 °C
Li	180.5	5.39	2	2 Mb at $\lambda = 193\,\mathrm{nm}$	741 °C

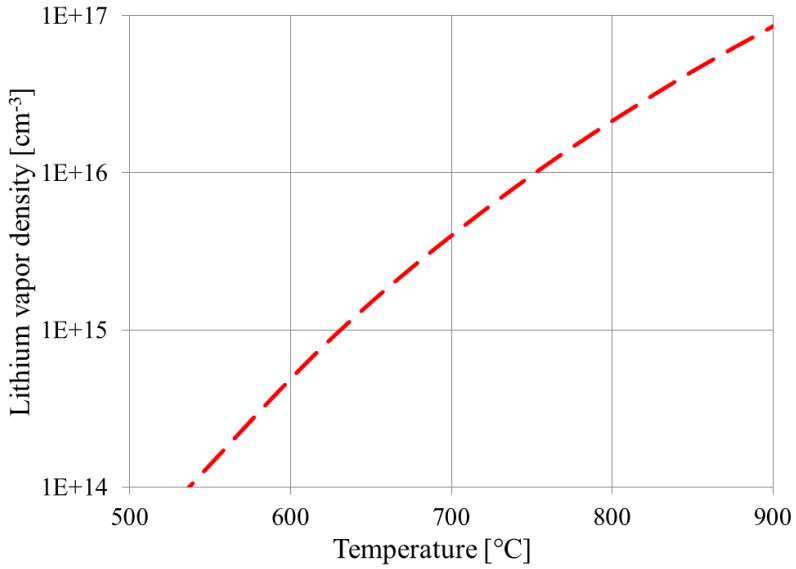

Figure 4.3: Lithium saturated vapor pressure curve [75].

4.2 Lithium distribution and heat pipe studies

Heat pipes invoke capillary forces to maintain the circulation of the working medium. Several wicking structures which are used in heat pipes for transportation of the liquid phase are described in [65, 66]. One of the most common wicking structures is a woven metal mesh screen laid around the inner surface of the heat pipe. The mounting and dismounting of the mesh screen is quite simple (if the heat pipe has a constant diameter). This type of wick structure is easily scalable: one can vary mesh parameters and the number of mesh layers to optimize the liquid transport.

A metal mesh screen was used in the SLAC plasma source [67], and the same wicking structure type was used in the first generation of the PITZ plasma cell. However, due to the side ionization scheme, the PITZ plasma cell has a more complex geometry with side arms (Fig. 4.2 (b)), so it was not possible to insert the mesh in one piece into the cell. A technique was developed to cover the inner surface of the plasma cell with several pieces of mesh, which were connected at their edges [76]. To test the transport of liquid lithium through this mesh setup, a special oven (Fig. 4.4) was manufactured at the DESY workshop. The oven itself is a steel pipe with two flanges at the ends, which are used to load specimen (in this case, small amounts of metallic lithium); additionally, they provide a port for a vacuum pump connection. The pipe is covered with two semicircular copper plates for better heat distribution. The plates have heating wire (filament) channels, the former of which is wound around the pipe and works as a resistive heater. The oven is covered with several layers of glass cloth heat insulation. A steel pipe of a smaller diameter and cut along into two pieces is used to test the mesh

specimens and connections between pieces of mesh. The test mesh was put against the inner surface of the smaller pipe pieces together with a small piece (3 to 4 g) of pure lithium, the small pipe was then closed and loaded into the oven. The oven is not a heat pipe: the mesh is placed within a region with homogeneous heating, and the lithium vapor is continuously pumped out during operation so that recondensation of lithium vapor is minimized which gives an opportunity to study the distribution of the liquid phase of lithium only. The experiments have shown that to ensure proper distribution over a mesh piece, the mesh should be placed close to the tube wall without any gaps. If this condition is fulfilled, the liquid lithium travels both horizontally and vertically over the mesh and the connections between the pieces. The connections are made by interlacing loose mesh wires. Following mesh parameters were chosen for the plasma cell wick: wire diameter $d = 0.28\,\mathrm{mm}$, opening between wires $w = 0.71\,\mathrm{mm}$, mesh number (number of openings per linear inch, $N = 1/((w + d)\ [\mathrm{inch}])$) of about 26.

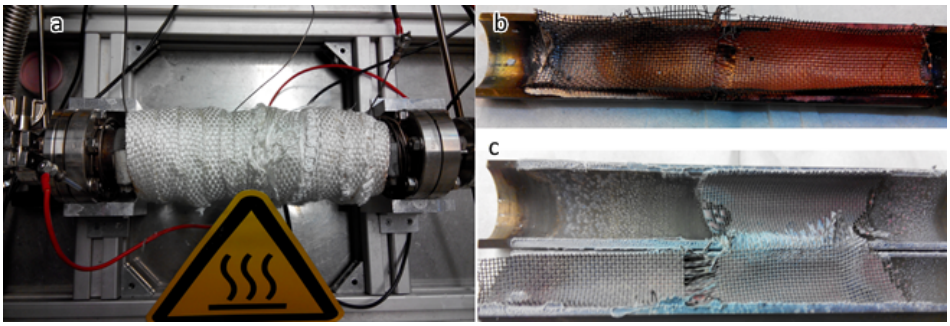

Figure 4.4: a: The oven for the lithium melting tests, top view; b: Lithium has melted well and passed the mesh joint; c: The pipe was closed and opened again after the test; lithium went from the left part of the mesh to the right part and from the bottom part to the top. This picture was taken the next day after the experiment, so lithium was already covered with an oxide layer.

However, long-term runs with the first generation plasma cell have shown that the metal mesh wick is complicated in use: there were some gaps in the side arms between the mesh and the walls, so large amounts of lithium accumulated there over time, not taking part in the circulation anymore. The loose wires used for the connection of the individual pieces served as additional condensation centers (Fig. 4.5). Although calculations (see Appendix B) show that the mesh that was used in the experiment ($N = 26$) provides enough capillary force to operate the heat pipe stably, it is mentioned in literature [77, 78] that the recommended mesh number for stable operation is 40. Meshes with higher mesh numbers are stiffer, and the spacing between wires is smaller which makes them impractical to use: it is harder to form separate pieces of the wick and then connect them inside the plasma cell. For that reason, other wick structures were considered for the second generation plasma cell. The calculations have shown that

the axial grooves provide a stronger capillary force than the metal mesh and that a heat pipe with axial grooves will perform stably at the desired parameters (Appendix B). Thus, it was decided to use the axial grooves in the second plasma cell generation.

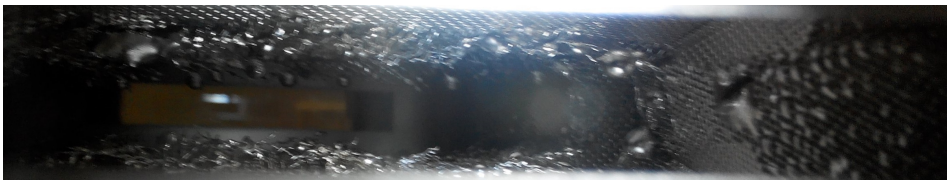

Figure 4.5: Lithium droplets condensed on loose wires at the mesh pieces connection inside the first generation plasma cell.

Another dedicated heat pipe setup was built (Fig. 4.6) before manufacturing the second generation of the plasma cell. This setup was used to study the metal grooves wick structure and to determine the optimal buffer gas pressure. The test heat pipe has the same dimensions as the main tube of the plasma cell: a length of 50 cm and diameter of 36 mm. Axial grooves were cut using an AC Progress VP3 wire electrical discharge machine [79]. 240 grooves (0.4 mm width and 0.3 mm depth) were cut into the inner surface of the test heat pipe. On the outer surface of the tube the grooves for electrical heating wires were cut. A type K thermocouple was mounted in the middle of the heat pipe in its outer surface to measure the oven temperature. Quartz windows were mounted at both pipe ends, allowing to observe the lithium melting and distribution process and to measure lithium vapor density with optical methods as described in [67]. Both ends of the pipe were water cooled in order to protect the windows and to enable the heat pipe process. A ThermoFlex TF1400 recirculating chiller [80] was used with the test heat pipe setup and with both plasma cell setups. It has knowingly higher cooling capacity than the maximum heating power at any configuration of the test setup. The gas inlet allows to adjust the buffer gas (argon) pressure while the heat pipe is in the cold state. About 5 g of lithium is needed to completely fill the volume of the grooves. The heating was governed by an in-house built, Siemens SIMATIC-based [81] controller. The controller maintains a desired heating/cooling rate or a temperature set point by dynamically adjusting the input power level. The same controller was used with both plasma cells.

At the beginning of the test, metallic lithium was loaded into the cold pipe, the pipe was pumped down, and the buffer gas was filled up to the desired pressure, and afterward the heating was started. As the test pipe heats up, lithium melts and starts to evaporate, and there is a mixture of the buffer gas and a low-density lithium vapor in the tube. With the heater temperature increasing the lithium vapor pressure rises and at a specific temperature, the pressure of lithium vapor is equal to that of the buffer gas. The molecules of the buffer gas are pushed to the tube ends due to increased lithium evaporation rate in the middle of the test tube and a lithium vapor column is formed [65]. There is a sharp transition zone (a flat front) between the lithium

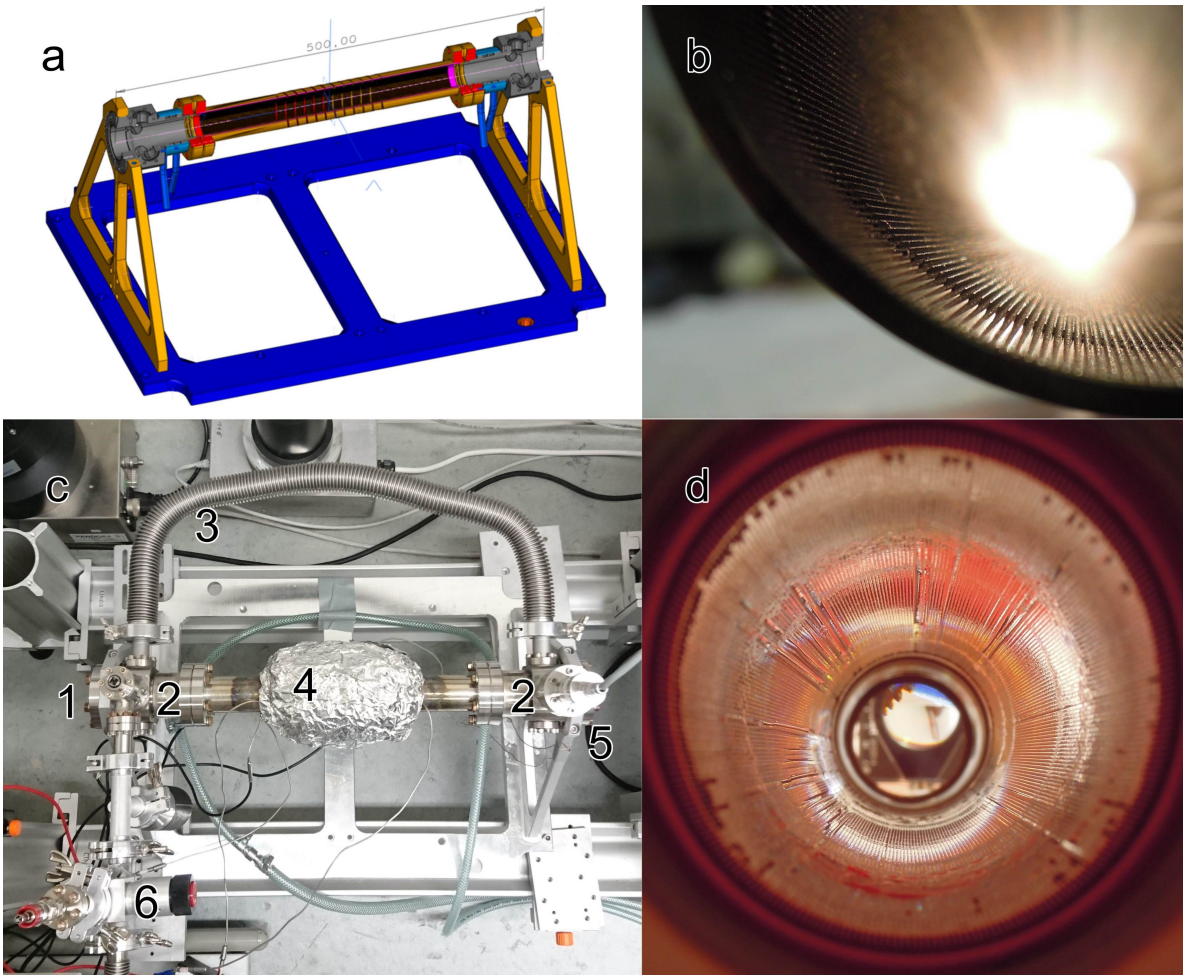

Figure 4.6: a: Design model for the heat pipe. b: Axial grooves cut inside the heat pipe. c: The heat pipe test setup. 1 – Viewport, 2 – Water cooling jackets, 3 – Buffer pressure equalization bypass, 4 – Heater covered with several layers of glass cloth and aluminium foil for heat insulation, 5 – Pressure gauge, 6 – Gas inlet and vacuum pump connection. Note the coloration of the steel pipe surface on both sides of the thermal insulation. It indicates the length of the adiabatic heat pipe zone. d: View through the heat pipe running at 700 °C. The axial grooves are filled with liquid lithium.

vapor column and the incondensable buffer gas. At this border, the lithium molecules collide with the buffer gas molecules, lose energy and condense to the liquid phase. The test tube starts to function as a gas-loaded heat pipe at the moment when this transition zone is formed: it transports heat using circulation and phase change of the working medium, and the temperature and pressure along the lithium vapor column are constant, while there is a temperature step at the vapor-gas transition zone. Any further increase of temperature requires a significant increase of input power, as heat

transport capacity of the heat pipe increases with the increase of the temperature. As the temperature rises, the lithium vapor pressure rises as well, the vapor column expands (the transition zones move closer to the pipe ends) and compress the buffer gas until the pressures of lithium vapor and buffer gas are equalized. This expansion effectively increases the condenser area, resulting in a higher heat transport rate. The lithium vapor column length depends on the initial (at the cold state) buffer gas pressure in the heat pipe and on the core-to-reservoir ratio (ratio of the metal vapor volume to the volume occupied by buffer gas) [65]. If the buffer gas pressure is too low, it will not confine the lithium vapor in the hot central zone of the oven, resulting in the condensation of lithium on the water cooled parts of the pipe and the windows. Measurements showed that visible lithium condensation on the cold parts starts within a few days of operation with the buffer gas pressure lower than 1.4 mbar. Figure 4.7 shows heating curves of the test heat pipe at various initial buffer gas pressures. In general, all curves demonstrate the same behavior: the input power-temperature dependency is linear until the specific temperature for the heat pipe oven mode at a given buffer gas pressure is reached. At that point, the required amount of heat needed for further increase of temperature sharply rises. The measured values are valid for this specific setup: for the cross-shaped plasma cell the heat flux and the core-to-reservoir ratio are not the same as for the test heat pipe; however, the values served as a reference for the initial plasma cell operating parameters, which were tuned in the course of preparatory test runs.

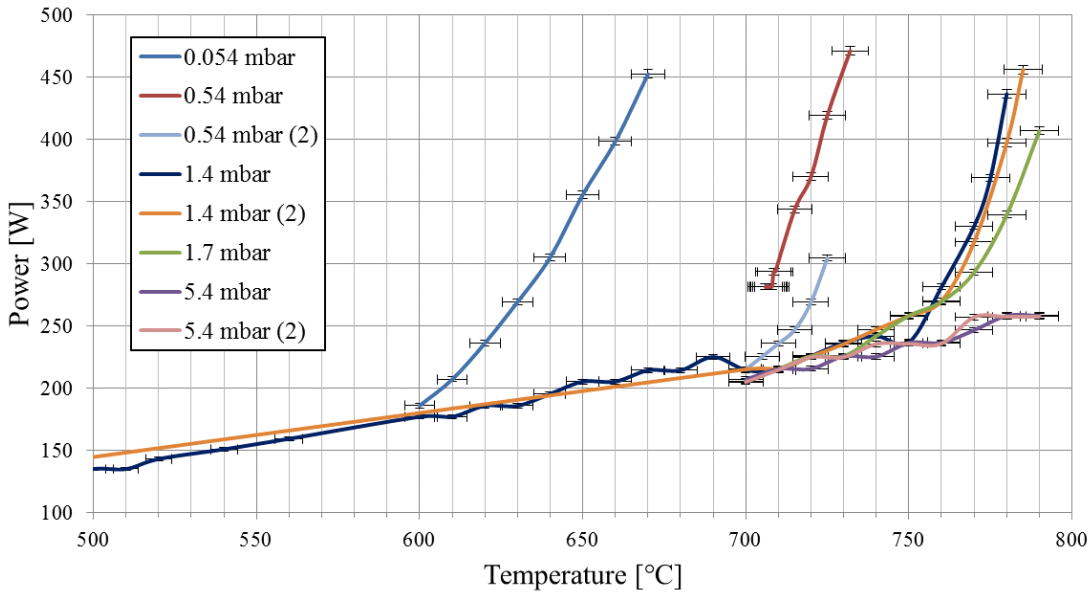

Figure 4.7: Power input vs. temperature set point for different buffer gas pressures. Kinks on the curves indicate transitions to the heat pipe oven mode. Pressure is given according to the readings of the Pfeiffer Vacuum TPR 018 vacuum gauge [82] at room temperature.

4.3 Plasma cell design

The PITZ plasma cell has a cross-shaped structure with four ports: two electron windows mounted at the ends of the main tube and two laser ports at the ends of the side arms (Fig. 4.8). There are water cooling jackets installed next to all four windows. All four buffer gas zones are connected for pressure equalization. The total length of the cell is 50 cm and the length of the ionization channel is 8 cm. It is possible to control the plasma channel geometry (especially the plasma channel length) and the plasma density by means of a shadow mask installed on the ionization port (this option was not yet implemented for the measurement described in this work). Another advantage of the cross-shaped design is the feasibility of optical plasma characterization methods conducted through the side ports, e.g., plasma density measurements with an interferometer. The first plasma cell was assembled and welded from separately manufactured pieces: beam tubes, side arms, central body, etc. (Fig. 4.9).

The side arms were funnel-shaped (expanding towards the ionization windows) in order to accommodate multi-pass ionization schemes, which were studied in [70]. The above-described metal mesh was used as a wick. There were four heating wires installed: two 210 W heaters in the central part of the cell and two 160 W heaters along the main tube (Thermocoax, ZUZAc/ZEZAc type [83], maximal operational temperature 800 °C). A copper heat spreader with channels to house the heating wires was mounted

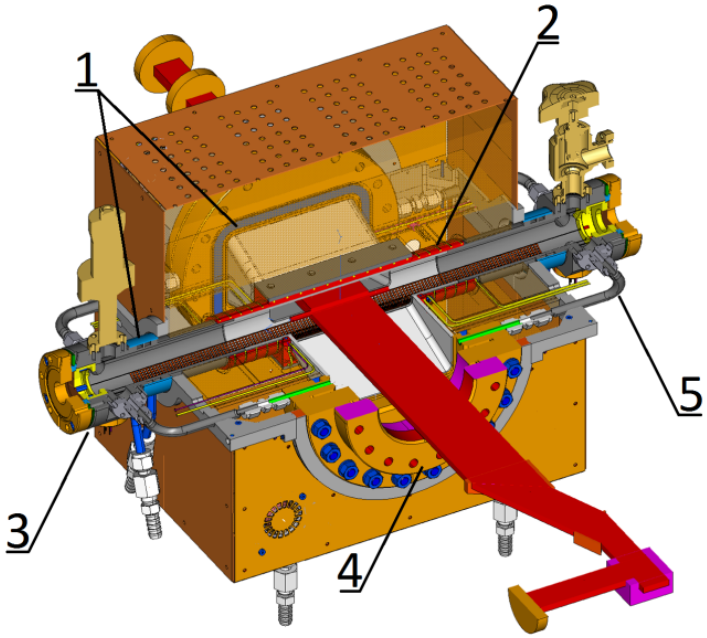

Figure 4.8: Design model of the first PITZ lithium plasma cell. 1 – cooling sleeve, 2 – heating coil, 3 – electron window, 4 – laser window, 5 – buffer gas distribution pipe. For more details refer to the text.

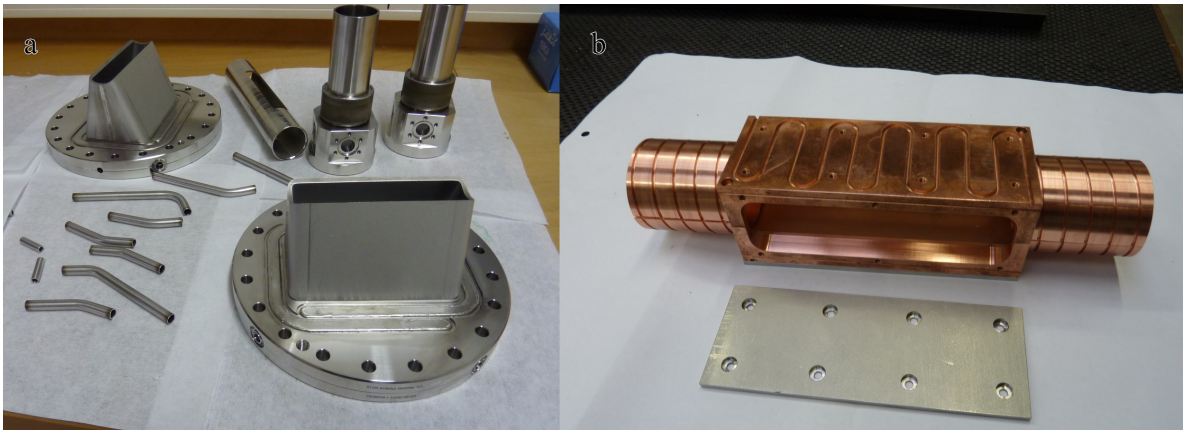

Figure 4.9: a: Parts of the first PITZ plasma cell; b: the copper heat spreader with channels for heating wires, consisting of upper and lower parts which are mounted around the central part of the first plasma cell. In front is a steel plate for the fixation of the heating wire on the heat spreader.

around the central part of the plasma cell (Fig. 4.9 (b)). Thermal insulation was provided by a solid foam brick assembly cut specially to accommodate the plasma cell metal body. The temperature distribution across the device and the mechanical stress

due to thermal expansion were simulated with the ANSYS software, aiding the design process [84].

Experimental runs in the PITZ tunnel conducted in the autumn of 2015 brought out downsides of the first plasma cell design. Liquid lithium transport in the oven was not optimal and over time lithium condensed and crystallized in the cold regions of the cell. The complex geometry of the side arms made the installation of the mesh inside the cell much more difficult compared to a simple tube. Overall heating power was not enough to achieve temperatures higher than 710 °C at that configuration. The main reason for this was strong heat loss through the funnel-shaped side arms with the large cross section. After multiple heating-cooling cycles, a virtual leak appeared (a volume of gas trapped in the metal body or a crack inside the plasma cell metal body and connected to the plasma cell volume by a narrow channel), complicating adjustments of the buffer gas pressure. The copper heat spreader was eventually heavily oxidized (Fig. 4.10), leading possibly to a decrease of its performance.

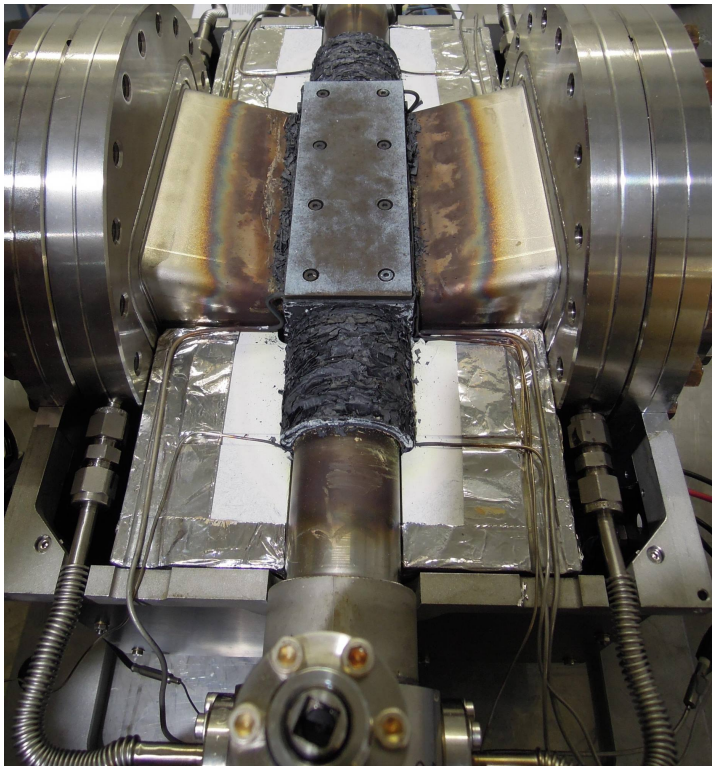

Figure 4.10: The first generation plasma cell with the top thermal insulation cover removed. The copper heat spreader was oxidized, and top layers of the oxide were exfoliated. The color tint on the steel body indicates the temperature distribution inside the plasma cell.

The second design is conceptually similar to the first one (Fig. 4.11). Following changes were made to improve the operational stability of the cell: the main body

without the flange connectors was manufactured from a single slab of steel (minimizing the possibility to create virtual leaks on heated weld joints) with grooves in its outer surface to accommodate the heating wires. The geometry of the side arms was simplified compared to that of the first plasma cell: they have a constant cross-section. This is because we only consider a UV laser with a collimated beam for ionization. Where it was possible, the metal walls were made thinner to minimize the cross-section of the pipe wall and therefore to minimize the solid body thermal conductance. The idea here was to make the temperature transition as steep as possible to minimize the loss of lithium vapor during the heating and cooling times. Four Thermocoax ZUZI/ZEZI type [83] heating filaments were installed, providing a total heating power up to 1 kW; their operational temperature limit is 1000 °C. Two central heating wires are fixed as meanders on the top and bottom of the crossing region. Two side heating wires are wound around the beam tube on both sides of the crossing area (Fig. 4.11 (b)). Three type K thermocouples are fixed on the outside of the beam pipe tube to measure the temperatures of the central and side heating elements. Axial grooves of the same parameters as in the test heat pipe are used as the wicking structure inside both the main tube and the side arms.

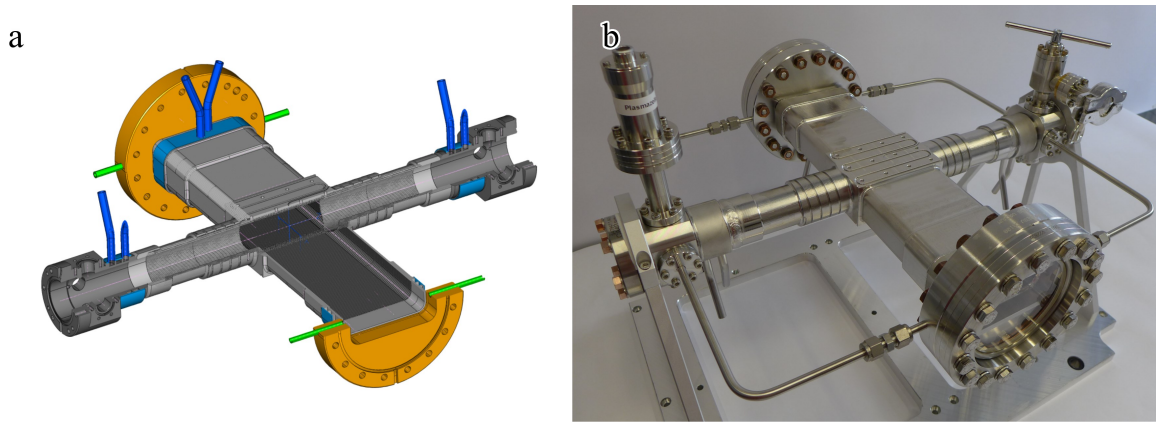

Figure 4.11: a: Design model of the second generation of the PITZ plasma cell. b: Assembled plasma cell without heating wires and heating insulation installed.

The temperature distribution without lithium along the main and orthogonal pipes was measured with a movable temperature sensor (Fig. 4.12). The movable sensor is a thermocouple type J mounted on a metal rod and inserted into the cell through a vacuum feedthrough installed instead of one of the viewports. The temperature drop in the central zone for the measurement along the beam pipe (Fig. 4.12 (a)) is attributed to heat losses through the side ports. During operation with lithium, the temperature of core zone equalizes due to the heat pipe mechanism [65]. Because of the heat conductivity of the metal rod, the temperature scans are not perfectly symmetric.

After initial measurements with the second generation plasma cell were conducted, metallic lithium was loaded into the plasma cell (Fig. 4.13 (a)) and melted; for the first

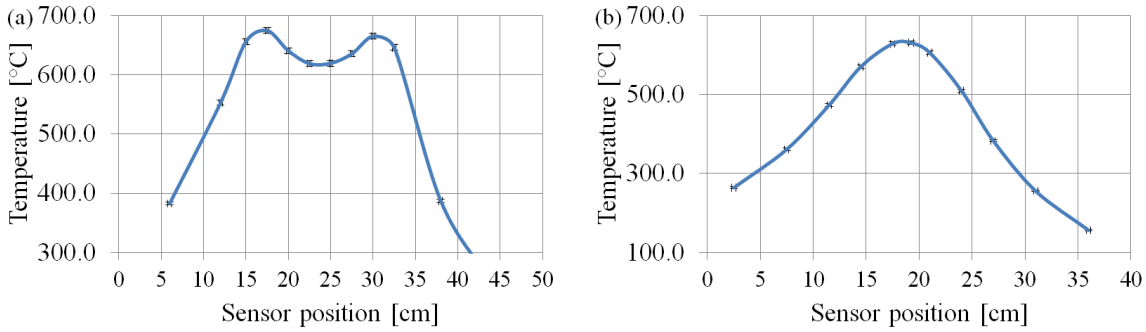

Figure 4.12: Temperature distribution inside the second generation plasma cell (a) along the beam pipe and (b) along the side arms, without lithium, measured with a movable temperature sensor. The temperature of the central heating elements is 700 °C.

time, plasma was generated in the new setup (Fig. 4.13 (b)), followed by measurements of metal vapor and plasma homogeneity.

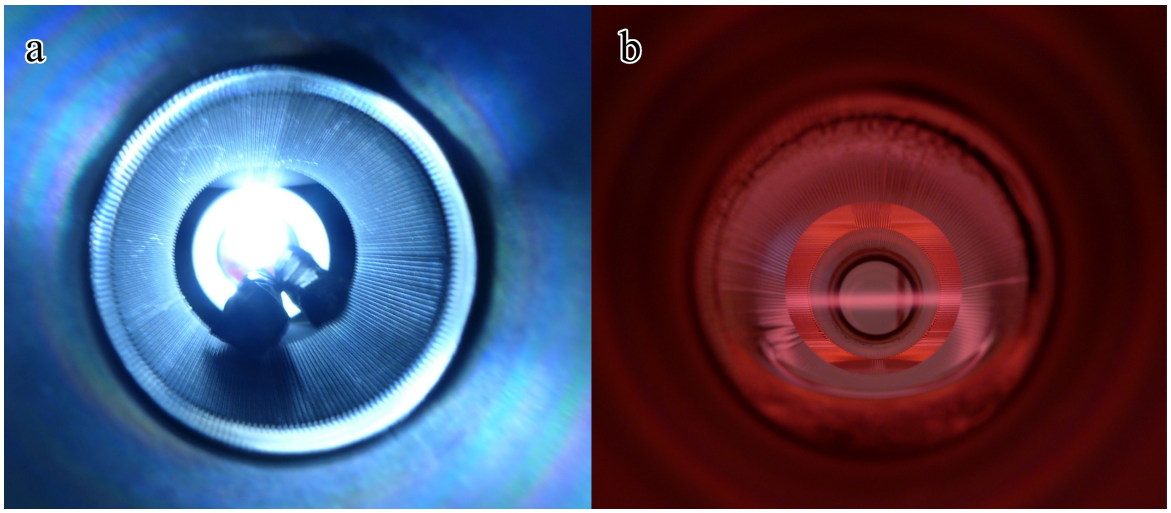

Figure 4.13: a: Lithium rods are loaded into the plasma cell. b: Plasma is generated through the sidearm ionization ports. A small aperture is installed between the ionization laser and the plasma cell, as described in Section 4.6.

The experiment described in Chapter 5 was conducted using the second generation plasma cell. That experimental run had shown that the condensation of lithium still occurred in the side arms as for the first plasma cell, but at a much-reduced rate. The maximum achievable plasma cell temperature during the experiment was 715 °C. The plasma density achieved during the experiment was about an order of magnitude lower than the goal plasma density of $1 \times 10^{15}\,\mathrm{cm}^{-3}$. After 7 days of operation, the mentioned experiment was interrupted: the cell went out of liquid lithium similarly to the first generation plasma cell. Figure 4.14 shows the interior of the plasma cell after

the experimental run seen through a side arm. It is seen that there is a sharp border between the core zone where the walls of the plasma cell are clean, and the outer zone where the walls are covered with small shiny crystals of lithium. Larger crystals had grown on the border of the two zones. Later it was found that the location of the condensation border corresponds to the dimensions of the heat insulation. Apparently, the plasma cell was not fully running in the oven mode: there was no sharp lithium vapor – buffer gas border or that border was located too far in the cold zone, resulting in incomplete circulation of lithium. As there was some initial surplus of lithium loaded into the cell, that surplus was compensating the lithium that condensed on the walls and never returned to the central zone. When the surplus was depleted, the vapor density in the core zone dropped to a low value and the experiment was stopped.

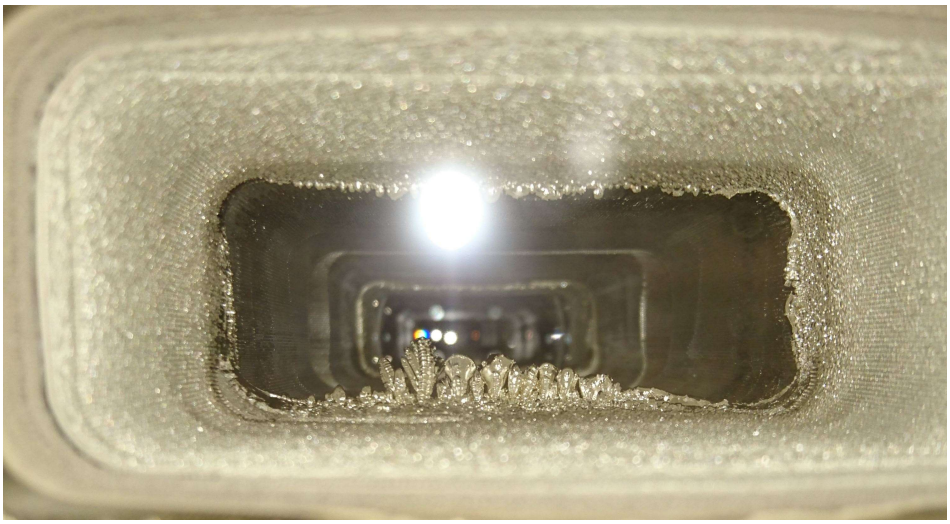

Figure 4.14: View through a side arm of the second generation plasma cell after 7 days of continuous operation in the beam line: lithium is mostly condensed outside of the core zone. There is a clearly distinguishable border between the heat insulated plasma cell core and non-insulated side arm parts.

For further experiments to be conducted in 2018, two measures were implemented in order to overcome this issue: the side arm heat insulation was extended by approximately 2 cm each side and the buffer gas pressure was increased from 0.9 mbar to 1.7 mbar. These two measures resulted in a 100 °C increase of the operation temperature. Due to higher buffer gas pressure, the lithium vapor column is shorter and the metal vapor – buffer gas transition zone is sharper. The plasma cell with the improved heat insulation and the increased buffer gas pressure demonstrated stable operation in laboratory conditions and better vapor homogeneity along the ionization channel (see Section 4.6). The improved setup will be used in follow-up experiments starting in 2018.

4.4 Electron windows and trajectory studies

Two electron windows are mounted at the ends of the main tube. Their function is to separate buffer gas and lithium vapor inside the plasma cell from the vacuum beamline in order not to contaminate the accelerator ultra-high vacuum environment and at the same time to introduce as low as possible scattering to the electron beam, since tight focusing of the beam into the plasma cell (i.e., high charge density) is one of the conditions to demonstrate SMI. The window must withstand continuous operation for at least one run period of 2 weeks in the beamline.

4.4.1 Beam scattering

It was shown that the maximum tolerable scattering introduced by the entrance electron window is 0.2 mrad with the goal to reach 50 µm rms radius size of the beam at the beginning of the plasma channel [85] (see Section 6.1). Thin polymer films are a favorite material for electron windows, since they have long radiation lengths (the radiation length is the measure of the energy loss in a material; it is the distance over that the electron energy decreases by e times), especially when made of polypropylene and polyethylene [76]. Additionally, these films are mechanically sturdy, minimizing the risk of damage during installation and operation. To estimate the electron beam scattering, different approaches were taken:

- An analytical estimation using the multiple Coulomb scattering theory [86]:

$$\Theta_{\mathrm{rms}} = \frac{13.6\,\mathrm{MeV}}{\beta c p}\sqrt{\frac{x}{X_0}}\left(1 + 0.038\ln\left(\frac{x}{X_0}\right)\right), \tag{4.1}$$

  where β is the ratio of the electron velocity to the speed of light c, p is the electron momentum in MeV/c units, x is the path length in the material, X_0 is the radiation length of the material.

- Scattering simulation with the FLUKA code [87, 88] assuming a transverse Gaussian particle distribution.

- Measurements of electron scattering in the PITZ beamline. The following setup was used: the foil specimen was mounted on the High1.Scr2 actuator. The rms beam sizes without and with foils inserted were recorded on a screen downstream of High1.Scr2 to find the divergence.

The analytical estimation fits well for a foil thickness of several tens of µm and more, but breaks down for thinner foils. The reason for this is that the number of scattering processes is reduced so much that a simple statistical approach underlying Eq. (4.1) is not valid anymore. FLUKA is a multi-particle Monte Carlo simulation package. For charged particle transport through matter, it uses a model based on Molière theory [89].

This model fits well with the experimental data, and it is relatively fast to compute. However, it is only valid if the number of elementary scatterings per step of simulation is large enough (> 20). In case of thin films, gaseous mediums or borders between different materials, the number of scatterings can be lower than that, and the simulation breaks down like the analytical estimation. To simulate scattering of foils thinner than approx. 8 µm, one has to tune the simulation by enabling a single scattering model based on the Rutherford formula with several correction factors [89,90]. In this model, every particle-matter interaction is a single simulation step, so it consumes much more computational power but delivers results that fit with the experiment. The simulations were conducted for Kapton, PEN and PET foils, and the obtained results are very similar since these materials have very similar radiation lengths (Table 4.2).

Kapton was the first candidate for the window material, as it is known for its good mechanical stability, high temperature resistance, and resistance to UV. However, there is no Kapton foil thinner than 7.5 µm available on the market, and it turned out that to fulfill the scattering requirements, a thinner foil is needed. In absence of a more suitable window material, the first experimental run in 2016 was conducted with 8 µm Kapton electron windows. Meanwhile, thinner samples of Mylar and PET were tested, and the main candidate was a 0.9 µm PET foil coated with 37.5 nm Al on both sides, which was available as a sample from Astral Technology Unlimited, Inc. [91], satisfied the scattering requirements. The metallization decreases gas permeability of the foil, sealing pores and other possible imperfections on the foil surface. At the same time, the mechanical stability of the foil and the easiness of handling are improved. The metal layers increase beam scattering, but it stays on the acceptable level. Figure 4.15 shows reasonable agreement between simulation and measurement. All methods demonstrate an exponential growth of the scattering, and simulation and experiment suggest a maximum allowable window thickness of about 2 µm.

Table 4.2: Properties of considered foils. Source: [92]

Film type	Polyimide Kapton	Polyester Mylar	Polyester PEN
Continuous operating temperature [°C]	240	105	180
Tensile strength at 25 °C [Kpsi]	33	30	40
Modulus [Kpsi]	430	550	850
Elongation [%]	70	130	70
Heat Shrinkage (200 °C, 30 min) [%]	0.1	4	1
Radiation length [cm]	28.58	28.54	29.49
Chemical formula	$(C_{22}H_{10}N_2O_5)_n$	$(C_{10}H_8O_4)_n$	$(C_{14}H_{10}O_4)_n$

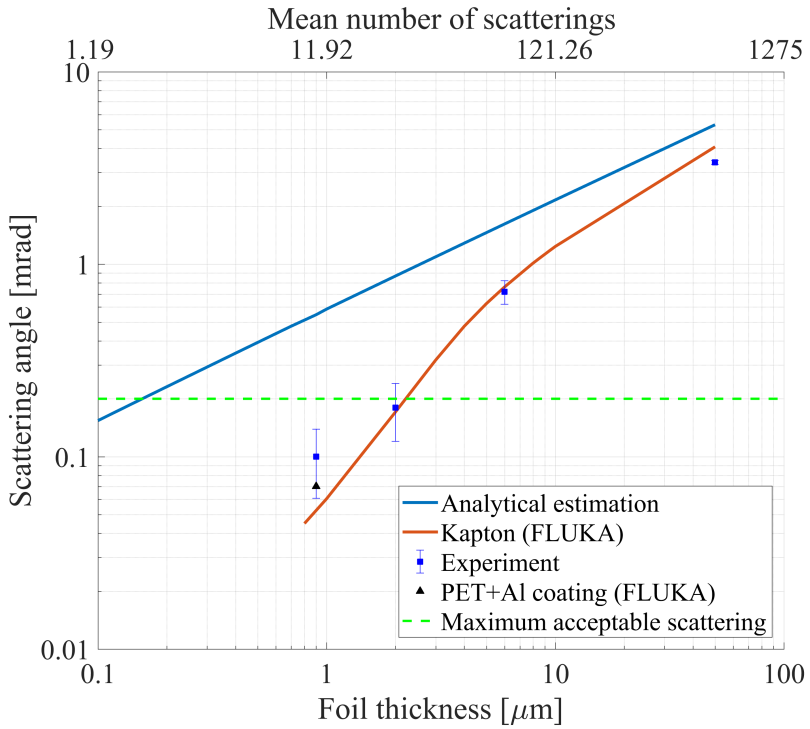

Figure 4.15: Electron beam scattering at polymer foils. The analytical estimation and FLUKA simulations were performed for Kapton and the electron beam momentum of 23 MeV/c using the single scattering model. Experiments were conducted with the following foil types: 50 µm – Kapton, 6 µm and 2 µm – Mylar, 0.9 µm – PET coated with 37.5 nm Al on both sides. The scattering angle for the last foil specimen was simulated separately. The black green line shows the maximum acceptable scattering for the experiment (0.2 mrad). The mean number of scattering events per electron is obtained from the FLUKA simulations.

4.4.2 Gas permeation and leak prevention

The gas permeation through the electron windows should satisfy two conditions:

- The pressure inside the plasma cell should not significantly change during operation;
- The leak rate through the entrance window should not exceed 1×10^{-6} mbar l s^{-1}, otherwise it will compromise the stability of the operation of the booster [93].

Although the permeation rates for different polymer foils are easily found in literature [94–96], data seems to be inconsistent, depending both on the measurement procedure and on the particular foil specimen. A special setup for permeation rate measurements was designed by Dieter Richter (HZB), and it was built in the vacuum lab at PITZ [97]. Initially it was planned to use helium as buffer gas, following [67],

but during the permeation tests the decision was made to use argon: due to a larger kinetic diameter of its atoms, the permeation rate of argon through foils is considerably lower, which outweighs the downside, that due to their higher mass, argon atoms cool down lithium vapor less effective than those of helium (less energy is transferred per atomic collision). Foils were prepared in a similar way both for the vacuum tests and for the installation on the plasma cell: a piece of foil with a diameter of about 2 cm was cut from the foil sheet and then fixed with vacuum glue on a steel flange having an aperture in the center thus covering it. Tests at the vacuum stand have shown that with argon buffer gas every tested type of foil except 2 µm uncoated Mylar would satisfy the requirements, but that the properties of certain samples of the same type may vary. The entrance window aperture diameter is 5 mm, and the exit window aperture diameter is 10 mm. This is a compromise between reliability and ease of operation: the entrance window is smaller to minimize mechanical stress and possibility of the lithium leakage towards the gun and booster cavities, while the larger exit aperture makes it easier to find optimal electron beam trajectories through the plasma cell.

In order to study possible damage by the electron beam, a stress test was carried out: a so-called dummy plasma cell was installed in the PITZ accelerator (Fig. 4.16). The dummy cell is a beam tube section terminated by the foil windows prepared and mounted as described above. It was installed in the plasma cell slot of the PITZ beamline, and the buffer gas pressure inside the dummy cell was set to the nominal experimental value. A 23 MeV/c electron beam was used for the stress tests.

Figure 4.17 shows the history of vacuum conditions around the dummy cell during the stress test with 0.9 µm coated PET windows[2]:

Top: 250 pC bunch charge, 5 bunches in the pulse train.

1. Opening booster vacuum valves
2. Start of the first stress test (beam only focused by the solenoid)
3. Stop of the first stress test / booster vacuum valves closed
4. Opening booster vacuum valves
5. Start of the second stress test (beam focused by the solenoid and quadrupole magnets)
6. Stop of the second stress test (interrupted by a non-related gun interlock)

It can be observed that the foil permeability depends on the beam focusing. If the beam was focused only with the solenoid, there was a steady increase of the beamline pressure over 9 hours, while with additional quadrupole focusing, the vacuum level remained almost constant over the same timespan.

Middle: 250 pC bunch charge, 10 bunches in the pulse train.

[2]The same foil was used for all measurements.

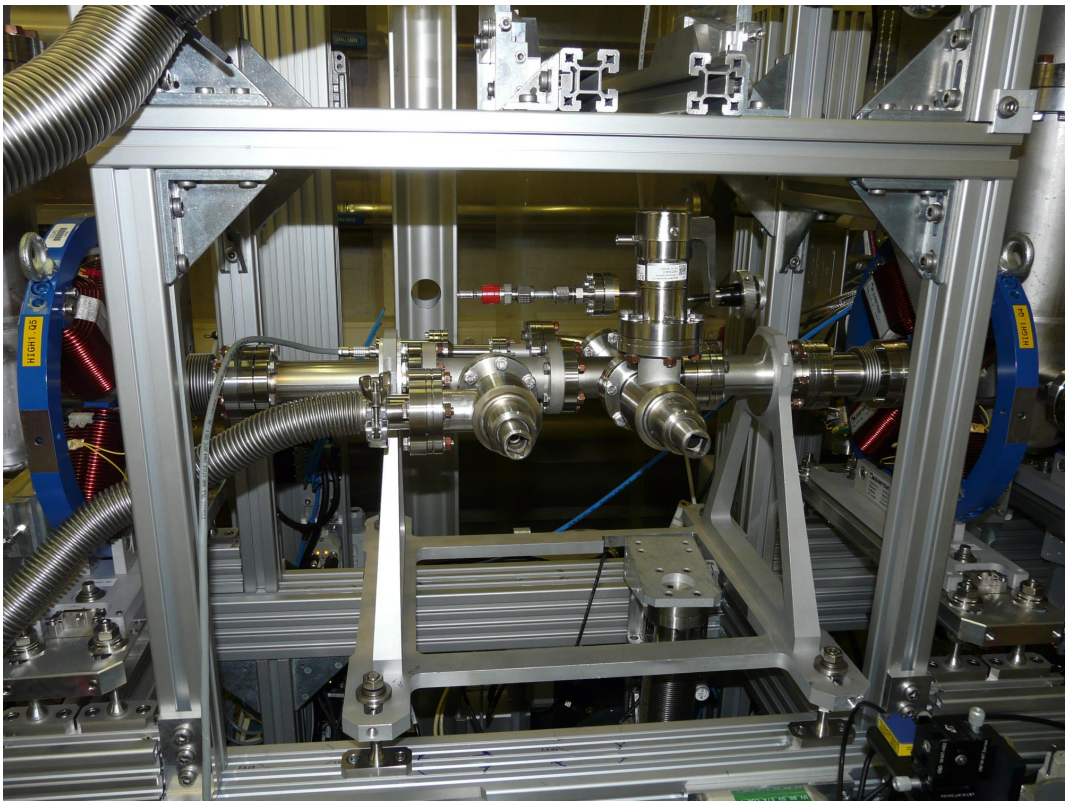

Figure 4.16: Dummy plasma cell installed in the beam line.

1. Opening booster valves

2. Start of the third stress test (beam focused with the solenoid and quadrupole magnets)

3. Stop of the third stress test / booster valves stay open

The vacuum level increases even without the electron beam being passed through the foils. It even improves slightly with the beginning of the third stress test. The test demonstrates that the dark current of the booster cavity has a bigger influence on the foils than the electron beam. When the third test started, the quadrupole magnets were switched on and defocused the dark current, decreasing the heat load on the foils, resulting in a vacuum level improvement.

Bottom: 1 nC bunch charge, 25 bunches in the pulse train.

1. Start of the fourth stress test (beam focused both with the solenoid and the quadrupole magnets)

2. Stop of the test (Booster interlock, not related to the test)

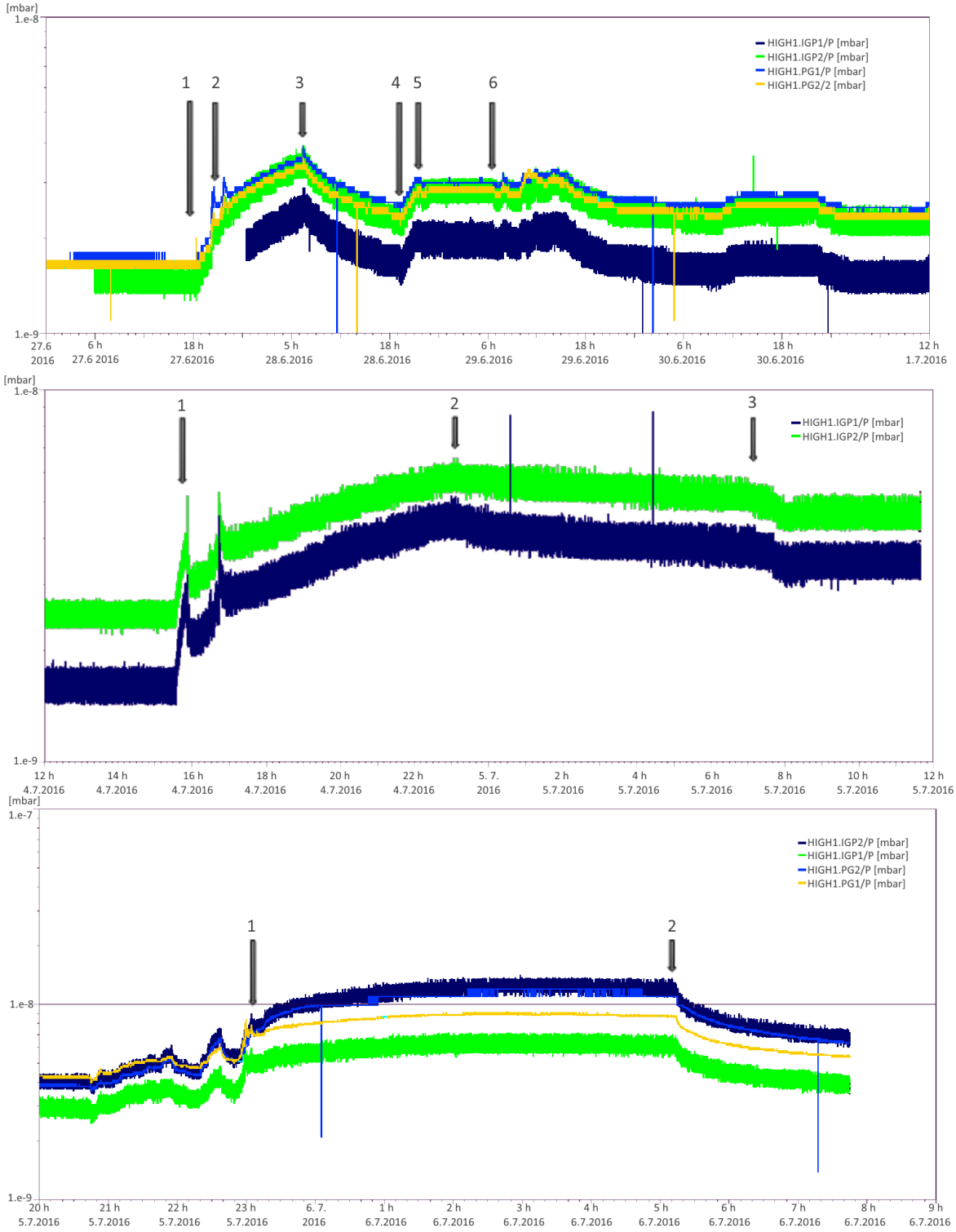

Figure 4.17: Dummy plasma cell stress test, 0.9 µm PET coated with 37.5 nm Al on both sides. See text for description.

The third test with significant beam loads – 25 times larger than the maximum expected load during the experiment – has shown that the foil permeation remains stable if appropriate beam transport is applied. The vacuum level slowly increased and almost saturated after 4 hours of the test. The vacuum increase during the tests was very small and did not affect the accelerator operation.

Dummy cell tests have proven that the foil can withstand several days of operation with electron beams of high intensities: the total electron beam charge during the tests is equivalent to about 200 hours of operation with a single 1 nC bunch, so no issues are expected for a 2 week long experimental run with nominal beam loads (during the experimental run, a substantial amount of time lower charge beams are used, e.g., for setting up the beam trajectory). As a consequence of these tests, the RF pulse lengths for the gun and booster cavities were shortened during the SMI experiment in order to minimize the dark current load on the electron windows.

Two samples of foils were investigated with an optical microscope after the 2 week experimental run in 2016 (Fig. 4.18). Since the trajectory settings were fixed in order to obtain the best focusing at the beginning of the plasma channel, the electron beam was hitting the same spots on the windows; these spots are clearly distinguishable under the microscope. A measurement after extraction showed that the permeation rate increased by two orders of magnitude and the foil became more fragile which could also be due to radiation damage. However, no systematic microscopic studies were conducted yet; for the experiment in 2018, the electron windows will be examined before and after the experiment.

The vacuum level around the plasma cell was not changing significantly during the experimental run. The increase of the plasma cell temperature (and, consequently the buffer gas pressure inside it) had a larger influence on the vacuum level than the electron beam impact.

There are two possible scenarios in case of window damage. If the whole window is destroyed, the gas content of the cell will be expelled into the vacuum beamline promptly. If the plasma cell is heated to the nominal temperature, lithium will reach the gun within 4 ms [93]; the reaction time of the valves in the PITZ beamline is slower, so in that case the cavity would be contaminated. However, the instant destruction of the whole window is more possible during preparations for the experiment, for example, by mishandling gas equipment while setting the desired buffer gas pressure. During operation the pressure is so low that the force is introduced by singular deflection of gas particles, therefore pressure difference is irrelevant. As microscopic investigations of foils show, it is possible to burn a hole through the foil with the electron beam, which could extend to a tear. In that case, the buffer gas will flow from the plasma cell into the beamline first and can be detected by an interlock system while the leak rate is low enough to prevent beamline contamination. A residual gas analyzer was mounted on the vacuum bypass above the plasma cell. It is set to monitor argon and lithium components of the beamline vacuum. If the presence of these gases in the beamline is detected, vacuum valves around the plasma cell will be closed to prevent any damage.

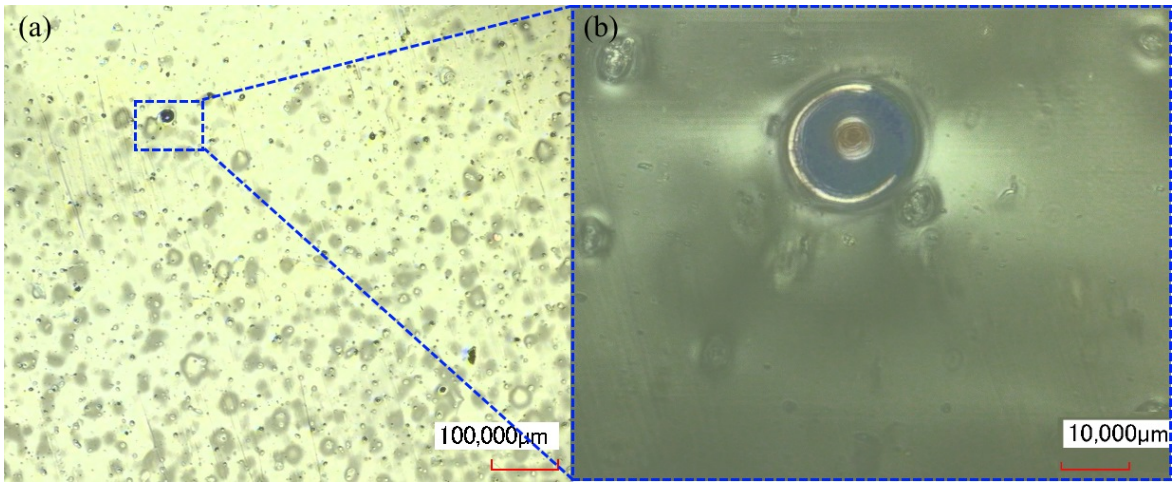

Figure 4.18: Microscopic investigation of the output electron window (Kapton, 8 µm) of the plasma cell after 10 days of continuous operation in 2016. Panel (b) is a zoomed-in area of panel (a). There is a bulge (swelling) on the surface of the foil associated with an electron beam influence.

4.4.3 Beam focusing

One of the important conditions of the SMI seeding is a high charge density (see Chapter 2). When designing the experimental setup, the position of the plasma cell and the magnets around were chosen such that it was possible to obtain a tightly focused beam at the entrance of the plasma channel and transport it further after the plasma cell [98]. In order to find proper trajectory settings, taking into account the scattering at the entrance window, an experiment was conducted: a 0.9 µm coated PET electron window was installed at the position of the plasma cell entrance ($z = 6$ m), and the beam was imaged on High1.Scr2 ($z = 6.25$ m), the position of which corresponds to the center of the plasma cell and plasma column. Optimum quadrupole magnets settings were established for a beam with 100 pC bunch charge [85]. Beam rms sizes and positions were recorded for all screens before the plasma cell for different charges: 100 pC, 250 pC, 500 pC and 750 pC (Fig. 4.19). It was shown that with the same quadrupole magnets settings only small adjustments (within 10 A) of the main solenoid current are needed in order to focus different charges. The beam $xy_{\mathrm{rms}} = \sqrt{x_{\mathrm{rms}} \cdot y_{\mathrm{rms}}}$ projection size on the screen raise very slightly with the increase of the total charge due to increased space charge forces, but this is overcompensated by the charge growing, resulting in higher charge densities for larger charges (Table 4.3). As the dummy cell test has demonstrated that the foil windows can sustain higher bunch charges, it was decided to use bunches up to 1 nC for the experiment.

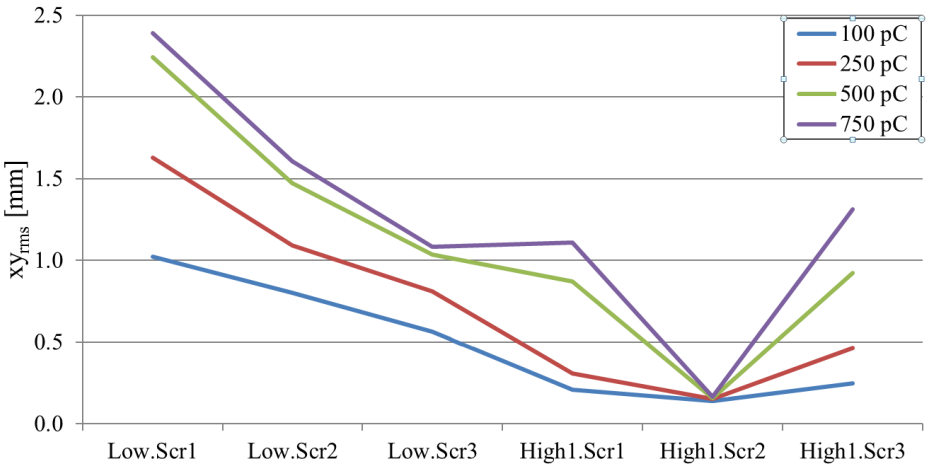

Figure 4.19: xy_{rms} size of electron beams with different charges recorded on the screen stations along the beamline with the electron window installed at $z = 6\,\mathrm{m}$ (distance between screens is not to scale).

Table 4.3: Charge density for different beam charges during the focusing experiment.

Beam charge [pC]	xy_{rms} size on High1.Scr2 [µm]	Charge density [a.u.]
104 ± 4	0.140 ± 0.08	1
250 ± 16	0.153 ± 0.07	2.09
501 ± 21	0.155 ± 0.07	4.05
761 ± 22	0.160 ± 0.06	5.40

4.5 Ionization laser

The ionization laser used for the experiment is a Coherent COMPexPro 201F ArF_2 laser [99]. It was purchased in cooperation with Bernhard Hidding's group (University of Hamburg). Its parameters are listed in Table 4.4. The laser is installed in a separate laser lab, and the laser beam has to be transported down to the accelerator tunnel. The laser beamline is about 12.5 m long and contains six mirrors and three optics boxes (Fig. 4.20) [100].

The first optics box is located close to the laser output and contains four cylindrical lenses with anti-reflection coating for compensation of the laser beam divergence. The second optics box is installed in the accelerator tunnel next to the plasma cell and contains two prisms needed to stretch the beam from the original spot size of $24\,\mathrm{mm} \times 10\,\mathrm{mm}$ to $80\,\mathrm{mm} \times 10\,\mathrm{mm}$ to fill up the whole plasma channel length. The third optics box is installed behind the plasma cell and contains another pair of anamorphic prisms to shrink the beam back in order to send it to an end mirror. The beam reflected by the end mirror travels back and makes a second ionization

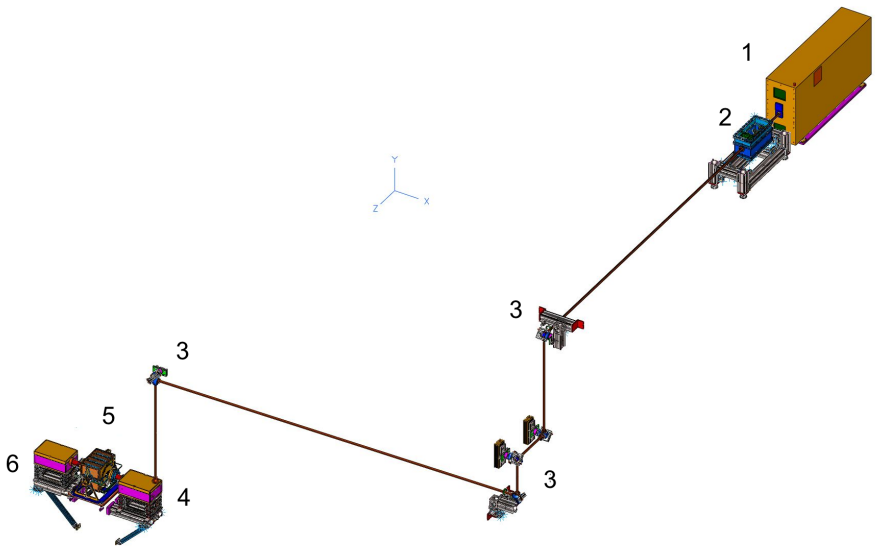

Figure 4.20: The ionization laser beamline. 1 – ionization laser, 2 – the first optics box (divergence compensation), 3 – mirrors, 4 – the second optics box (transverse stretching), 5 – plasma cell, 6 – the third optics box (diagnostics). Image provided by Gerald Koss, see also [100].

pass through the plasma cell resulting in higher plasma density and homogeneity [70]. A small portion of the laser (about 1 % of the initial intensity) which passes the end mirror is sent to diagnostic devices installed in the third optics box: a power meter, a photomultiplier for synchronization tuning, and a CCD camera for real-time profile control. As a final preparation for the experiment, a detailed laser profile measurement was conducted in the tunnel with a power meter mounted on a 2D linear stage (Fig. 4.21 (b)). A Newport 813J-25 power head was mounted behind the plasma cell instead of the third optics box for that measurement. A Newport Model 1825-C power/energy meter was used for readout [101]. As a reference, the transverse laser profile was measured directly next to the laser output aperture (Fig. 4.21 (a)). The profile measured after the plasma cell has an approx. a 4-cm long region of high intensity, and then the intensity decreases to about 50 % of the maximum. The energy of the laser pulse delivered to the plasma cell was 150 mJ, which is sufficient for the ionization [70]. A possible reason for the suboptimal laser beam transport is the laser's multi-mode nature: the laser divergence varies for different modes, so not all the modes can be transported efficiently using the same optical elements in the beamline. The profile homogeneity can be improved by installing a filter which has a variable laser transmission across the ionization port position at the expense of the amount of laser power delivered to the plasma cell.

Table 4.4: Coherent COMPexPro 201F ArF_2 specifications.

Wavelength	193 nm
Photon energy	6.43 eV
Pulse energy (max. according to the specifications)	400 mJ
Pulse energy (max. after gas refill)	480 mJ
Pulse length	25 ns
Max. repetition rate	10 Hz
Beam dimensions (V × H)	24 mm × 10 mm
Beam divergence (V × H)	3 mrad × 1 mrad

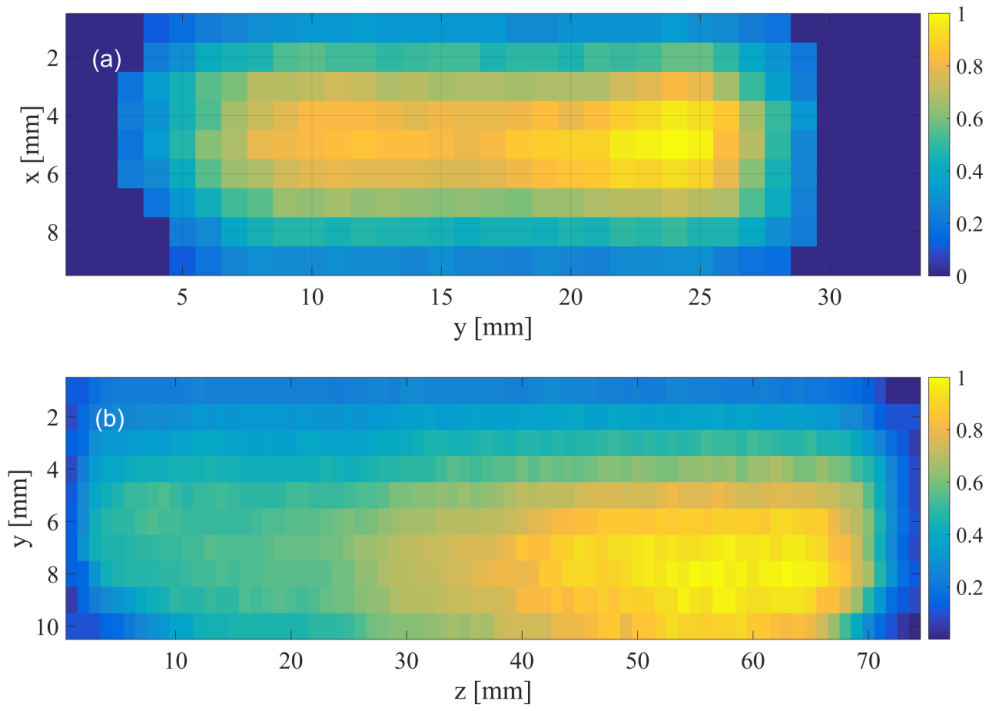

Figure 4.21: The ionization laser profile measured (a) at the laser output aperture, (b) behind the plasma cell. The electron beam comes from the right side for the case (b).

Two MgF_2 windows[3] were forseen as entrance and exit ports of the ionization laser into and out of the plasma cell. Before the plasma cell was installed in the tunnel, the laser transmission through the windows was measured. For one of the windows, the transmission was 84 to 86 % at different measurement points, and the other one

[3]MDC BVPZ100MGF2-NM [102]

demonstrated transmission of only about 25 %. The latter window was exchanged with a quartz window (measured transmission of 86 to 88 %). After the experiment, the laser transmission was measured again. Both windows were coated with a very thin layer of lithium, which was visible on the window surface under certain viewing angles. The transmission was approximately 5 to 10 % worse, depending on the measurement point. After the windows were cleaned with water and alcohol, the transmission restored to the respective initial values.

4.6 Lithium vapor density measurements

Several methods for lithium vapor density measurements are described in [67], two optical methods described therein were used at PITZ. The UV absorption and the white light absorption methods were used to measure lithium vapor density and homogeneity of the density along the ionization channel of the PITZ plasma cell. A sketch of the measurement setup is shown in Fig. 4.22.

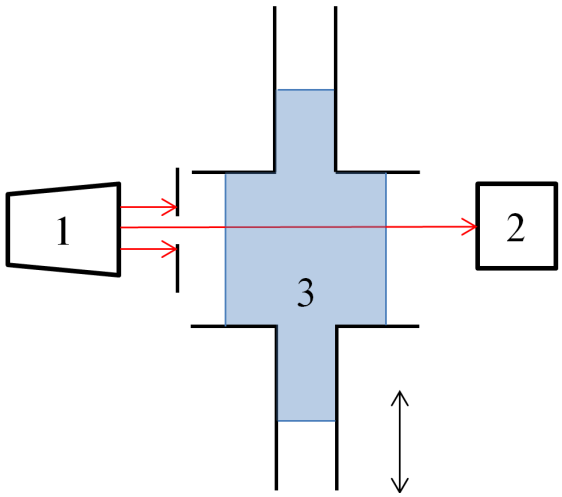

Figure 4.22: Sketch of the vapor density measurement setup. 1 – laser or white light source with an aperture installed in front of it, 2 – power meter or the spectrometer, 3 – lithium vapor inside the plasma cell. See text for description.

Both methods are conceptually similar: the UV absorption method allows one to deduce the linearly integrated vapor density $n_v L$ by measuring the amount of laser power $E_{\text{transmitted}}$ that is transmitted through a vapor column of length L:

$$n_v L = -\frac{1}{\sigma} \ln\left(\frac{E_{\text{transmitted}}}{E_{\text{incident}}}\right), \tag{4.2}$$

where n_v is the vapor density, E_{incident} is the energy of the laser pulse sent into the vapor, $\sigma = 1.8 \times 10^{-18}\,\text{cm}^{-2}$ is the ionization cross section for a photon energy of

6.42 eV (corresponds to $\lambda = 193$ nm) [74]. Low energy laser pulses were generated by the COMPexPro 201F and measured with the Newport Model 1825-C power meter and the Newport 813J-25 power head.

The white light absorption method is based on the measurement of the transition line of lithium around $\lambda_{ij} = 670.8$ nm. The analytical formula for the relative intensity absorption is given [67] as

$$\gamma(\omega) \simeq \frac{-N_i e^2}{2c\varepsilon_0 m_e} \frac{f_{ij}\Delta\omega/2}{(\omega_{ij}-\omega)^2 + (\Delta\omega/2)^2}, \tag{4.3}$$

where ω is the frequency of the absorbed light, N_i is the plasma density at the ground atomic state i, e is the electron charge, c is the speed of light, ε_0 is the vacuum permittivity, m_e is the electron mass, f_{ij} is the absorption oscillator strength of the transition $i \to j$, ω_{ij} is the frequency of the absorption line, and $\Delta\omega$ is the effective line width. The plasma density is deduced then by fitting the calculated curve to the measured absorption spectrum. A continuous white light spectrum was generated by a halogen lamp and measured with an OceanOptics HR2000+ spectrometer [103] with an optical resolution of 0.5 nm FWHM.

Vapor density measurements were conducted for the test heat pipe using the UV absorption method and for the second generation plasma cell with the improved insulation the white light method was used. The measurement results are shown in Fig. 4.23 together with the lithium saturated vapor pressure curve.

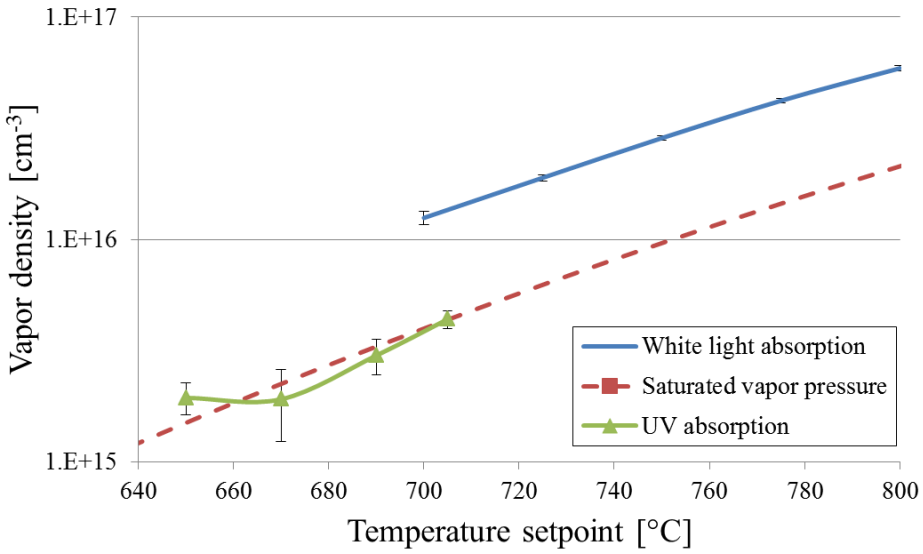

Figure 4.23: Lithium vapor density measurements

The UV absorption method yields the linearly integrated vapor density, and to get the direct vapor values one needs to estimate the vapor column length, assuming

that the vapor density remains constant along the vapor column. The vapor column length was estimated from the length of the heat pipe surface coloration, as shown in Fig. 4.6 (c), and from the condensation borders visible through the viewports. The white light absorption method yields unphysically high density values, however, the measurement curve trend is in agreement with the saturated pressure curve. It's mentioned in [67] that this method seems to overestimate the value of plasma density when compared to other methods and depends critically on the estimation of the effective linewidth $\Delta\omega$ (its value was taken from [67]). Although the absolute values delivered by that method are too high, the method is still valid for homogeneity measurements.

Homogeneity along the ionization channel was measured with a setup as illustrated in Fig. 4.22: the plasma cell was moved with respect to the fixed setup of the light/laser source and the measurement device, and the vapor density was measured through the plasma cell side arms at several positions.

Figure 4.24 shows lithium density profiles for the second generation plasma cell at a buffer gas pressure of 1.4 mbar. This measurement was carried out using the UV absorption method. For the set point of 705 °C, the peak to peak vapor density inhomogeneity is about 22 %. The vapor column length can be estimated from clearly visible condensation borders in the side arms and it is roughly equal to 24 cm, which gives a vapor density of $n_v = 4.4 \pm 0.4 \times 10^{15}\,\mathrm{cm}^{-3}$. The vapor homogeneity measurement for the setup with the improved heat insulation was conducted using the white light absorption method (Fig. 4.25).

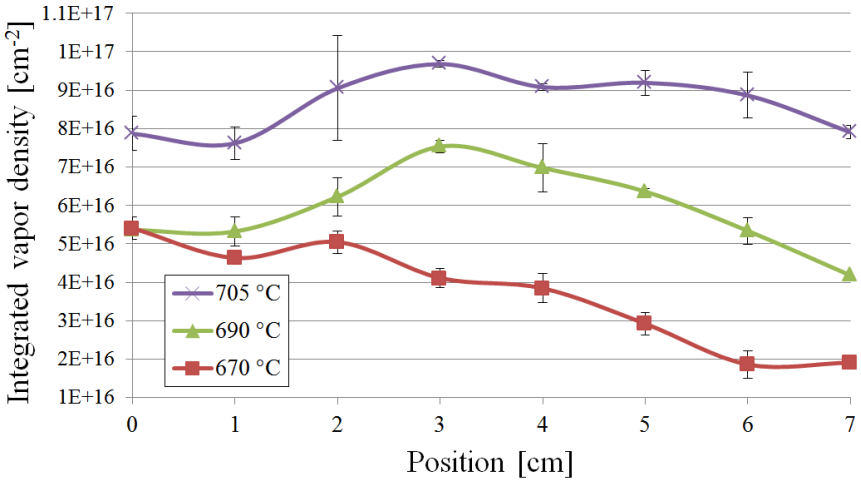

Figure 4.24: Linearly integrated lithium vapor density measured with the UV absorption method. The density is measured along the ionization channel of the 2nd generation plasma cell. The buffer gas pressure was set to 1.4 mbar for this measurement

For that measurement, the buffer gas pressure was set to 1.7 mbar. As mentioned above, the absolute density values obtained via the white light absorption are evidently

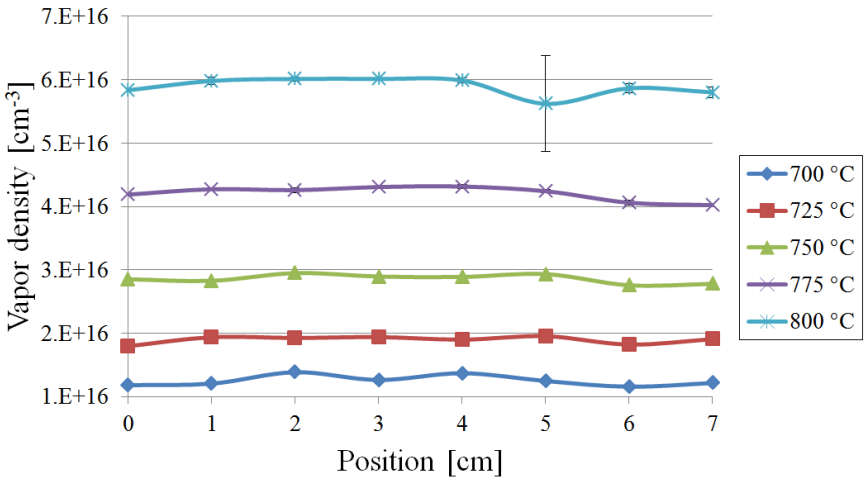

Figure 4.25: Lithium vapor density measured with the white light absorption method. The density is measured along the ionization channel of the 2nd generation plasma cell with the improved side arms insulation. The buffer gas pressure was set to 1.7 mbar for this measurement

too high. Nevertheless, the measurement shows that the vapor density inhomogeneity is less than 10 % for the setup with the improved heat insulation at all temperatures the measurement was conducted for.

4.7 Conclusions

Over the course of the preparatory experiments several technical tasks and studies were completed:

- Plasma cell oven preparations:
  - Heat pipe oven properties studies: geometry, wicking structures, operating parameters and procedures;
  - Electron windows: gas permeation measurements, durability studies and implementation of the interlock system;
  - Measurements of the metal vapor and the ionization laser profiles.
- The electron beam trajectory from the gun to the plasma cell

This work provided a necessary foundation for the SMI experiment. The experimental run with the first generation plasma cell revealed the shortcomings of that design: the funnel-shaped side arms together with the wire mesh led to the accumulation of solid lithium in the cold zones of the plasma cell. The second generation plasma cell has

demonstrated a much better performance, but the goal plasma density was not reached and its operation period was still limited by the lithium condensation issue. Nevertheless, parameters of the plasma reached with that setup were sufficient for experimental observation of the SMI which is described in the following chapter. The improvements introduced after the main experiment provide substantially higher lithium vapor densities and stable operation at laboratory conditions; the updated setup will be used in the follow-up experiments.

The side ionization scheme shown in Fig. 4.2 allows one to manipulate plasma channel parameters: it is possible to introduce a plasma density variation along the electron beam propagation direction by means of installing an optical filter with the required laser transmission variation. Another possibility is to install a movable screen that blocks a part of the ionization laser profile, effectively shortening the plasma channel length. The latter option is especially attractive, as it allows to measure the self-modulation amplitude as a function of the distance propagated in plasma, and thus observe the stages of the instability development described in Section 2.7. These options were not implemented for the measurement described in this thesis and are planned for the follow-up experiments.

Chapter 5

The SMI experiment

This chapter is dedicated to the experiment conducted in order to demonstrate the self-modulation of a long electron bunch in a lithium plasma. It describes experimental conditions and presents experiment results including the longitudinal phase space of the electron bunch after interaction with plasma. Figure 5.1 shows the PITZ beamline layout and highlights devices and measurement stations which were used for the experiment.

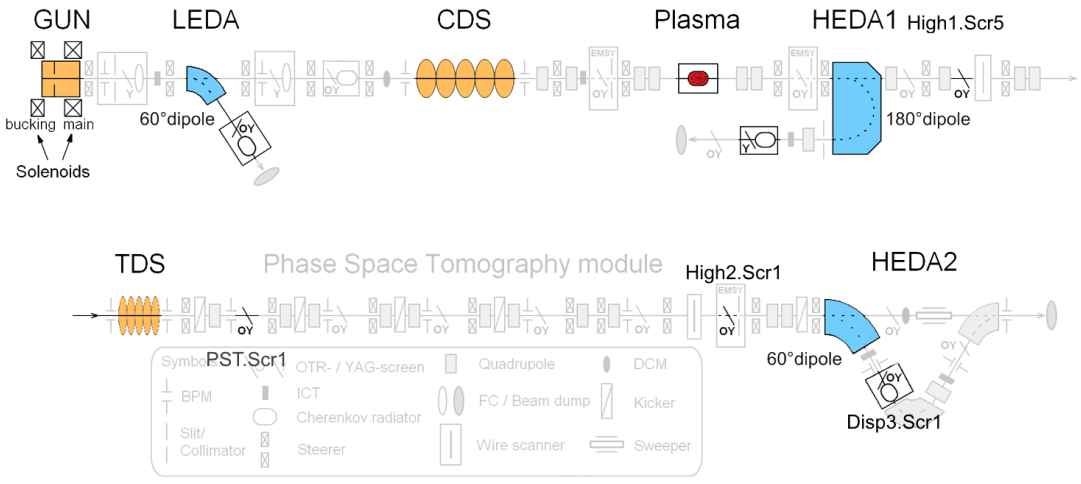

Figure 5.1: Devices and screen stations for the measurements of the SMI. Based on Fig. 3.1 from [51].

5.1 Experimental conditions

Measurements were performed using accelerator parameters similar to the nominal parameters for the emittance measurements, see e.g. [104]. The transverse laser distribution during the experiment was uniform (Fig. 5.2 (a)). A temporal flat-top laser distribution with a rise time of 2 ps was set. As the OSS was not available during the experiment, there were no means to measure the laser temporal profile directly. Instead, the electron beam temporal profile was taken at PST.Scr1 with help of the TDS (Fig. 5.2 (b)). The longitudinal expansion of the electron beam compared to the laser pulse length (24 ps FWHM) is attributed to the space charge forces. Although there were no ways to measure laser pulse length directly, its length could be deduced from the temporal structure of the electron beam profile measured with the TDS. By changing parameters of the laser pulse shaper, it is possible to expose individual Gaussian peaks and to verify that all birefringent crystals contribute to the elongation of the flattop profile).

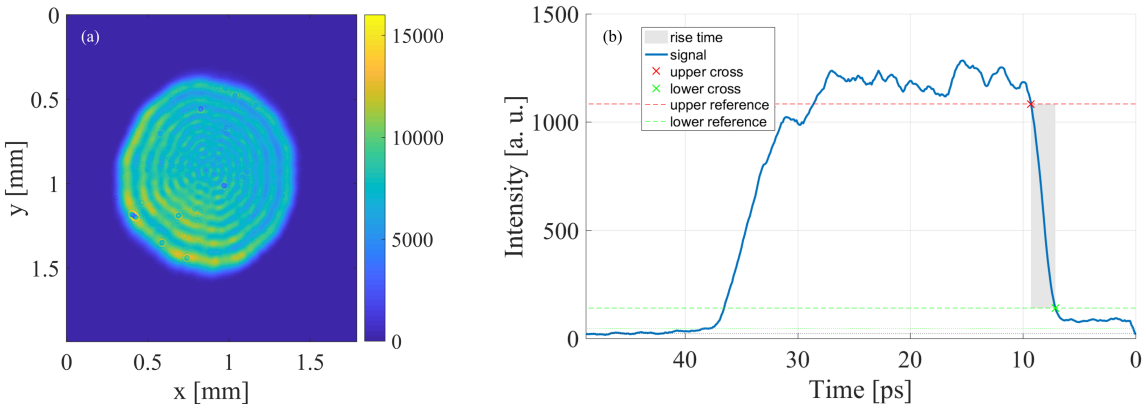

Figure 5.2: (a) Transverse laser profile recorded at VC2; (b) Temporal electron beam profile measured at PST.Scr1 after passing the TDS.

The gun accelerating gradient was set to 60 MV/m and the average mean momentum of the electron beam after the gun was 6.54 MeV/c at the gun maximum mean momentum gain (MMMG) phase. The average beam momentum after the booster cavity was 22.3 MeV/c with the rms momentum spread measured to be 0.1 MeV/c at the booster MMMG phase. Beam momentum and cavity MMMG phases were defined using the LEDA, HEDA1 and HEDA2 dipole spectrometers. The TDS deflecting voltage was set to 0.5 MV for measurements at PST.Scr1 and to 0.25 MV for measurements at Disp3.Scr1. The beam transport to the plasma cell, especially the focusing into the cell, was determined during the pre-experiments and remained unchanged for all subsequent measurements ($xy_{\mathrm{rms}} \approx 160\,\mu\mathrm{m}$ at the beginning of the plasma channel). Downstream of the plasma cell, the beam was focused on the measurement screens PST.Scr1 and Disp3.Scr1. To avoid beam losses during beam transport to the measurement stations,

the beam charge was controlled with the ICT devices: steering and focusing of the beam were adjusted so that High1.ICT1 ($z = 5.18\,\mathrm{m}$, upstream of the plasma cell) and High2.ICT1 ($z = 17.08\,\mathrm{m}$, downstream of the TDS and upstream of the HEDA2 dipole) in the main beamline and Disp3.ICT1 ($z = 20.82\,\mathrm{m}$, downstream of the Disp3.D1 dipole) in the HEDA2 section all measured the same electron beam charge. The ionization laser triggering time was initially tuned to synchronize arrival times of the laser (a signal measured by a photomultiplier installed in the diagnostics box behind the plasma cell) and of the electron beam (a signal measured with the Faraday cup Low.FC1). Later the ionization laser timing was fine-tuned by observing the strength of the beam-plasma interaction on the measurement screens. The ionization laser profile at the position of the plasma cell is shown in Fig. 4.21 (b). The ionization laser energy was measured with a power meter installed in the diagnostics box behind the plasma cell and is approximately equal to 150 mJ at the plasma cell entrance. The plasma cell temperature initially was set to 700 °C and for the longitudinal phase space measurements it was raised to 710 °C in order to increase the lithium vapor density, and hence the plasma density and maximize the number of visible modulations.

5.2 The measurements

5.2.1 Beam transverse profile

The transverse beam profile with plasma off and plasma on was observed on High1.Scr5 (Fig. 5.3). The defocusing of the beam that passed through plasma was similar to the halo formation of the beam demonstrated at FACET [27]. The halo indicates the presence of transverse defocusing fields, while an absence of a tight core (opposed to what has been observed at FACET) can indicate a phase slippage intrinsic to the self-modulation instability. At FACET, the propagation distance in plasma is much larger than that at PITZ, so as the self-modulation instability develops and saturates, the electron beam sub-bunches (already focused by the SMI) can be subjected to further self-focusing in the nonlinear regime [105]. Another possible reason is that, although some parts of the self-modulated beam are strongly focused, the overall projected charge on the YAG screen in the central region of the beam projection is smaller and, subsequently, the measured light signal is lower compared to that of the initial non-modulated electron beam.

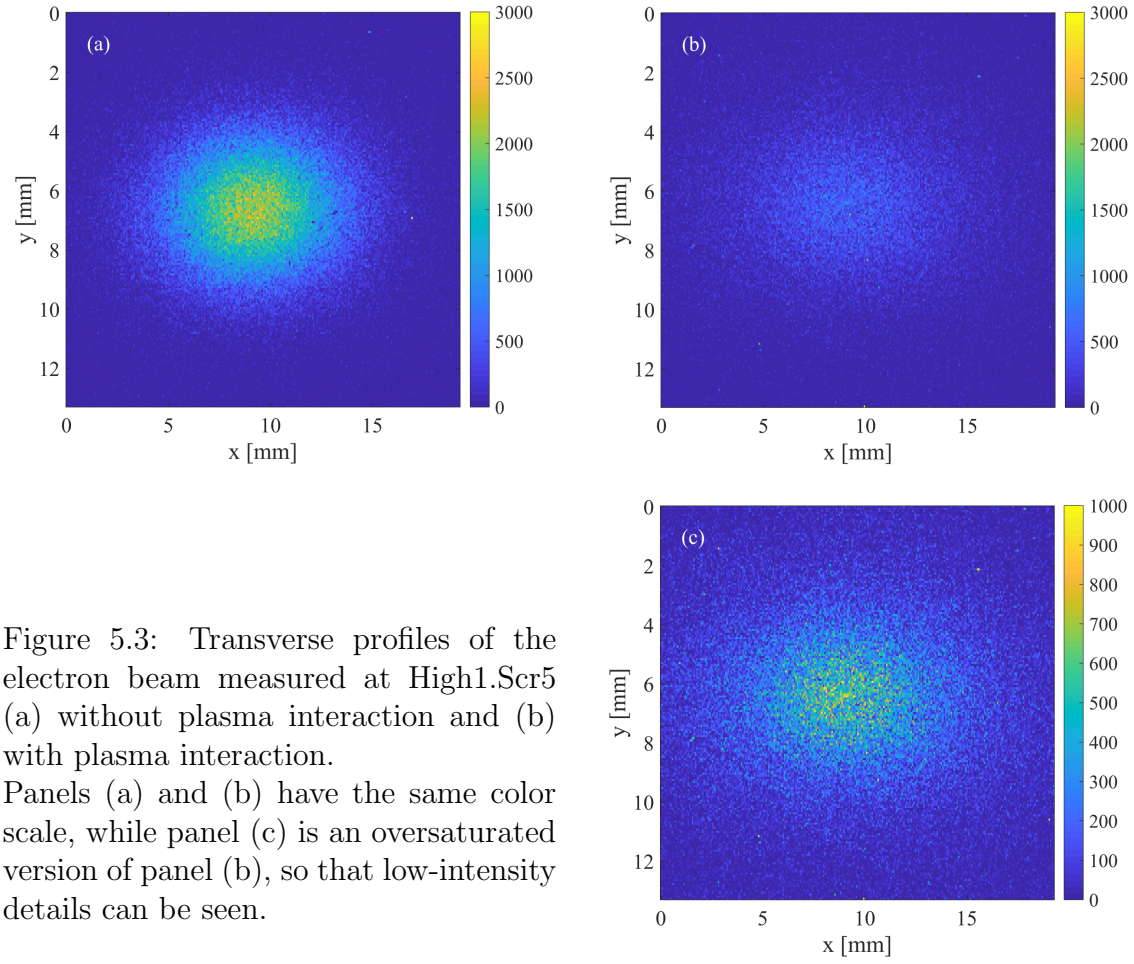

Figure 5.3: Transverse profiles of the electron beam measured at High1.Scr5 (a) without plasma interaction and (b) with plasma interaction.
Panels (a) and (b) have the same color scale, while panel (c) is an oversaturated version of panel (b), so that low-intensity details can be seen.

5.2.2 Time-resolved profile measurements

These measurements were conducted with the TDS on PST.Scr1 (Fig. 5.4). In order to achieve a high temporal resolution, the beam was tightly focused on the measurement screen with the TDS switched off. Then the TDS power was set to the maximal useful level which is relatively low (0.5 MW) and is mainly limited by the streaked beam intensity on the screen (only one electron bunch can be used since the plasma density is changing significantly during the 1 µs temporal spacing between the two consecutive bunches) and by the clipping of the beam on the beamline apertures during the TDS phase scan that is necessary for the TDS calibration (see Chapter 3). As a result, the bunch was streaked to approximately of the screen height.

This measurement gives a better insight into the beam-plasma interaction process compared to the transverse profile measurements. Figure 5.4 (a) shows an initial flat-top longitudinal profile of the beam with a sharp front (on the right) and only slightly changing intensity along the beam (a similar 1-d intensity profile of a TDS measurement

is shown in Fig. 5.2 (b)). Figure 5.4 (b) shows the most pronounced effect of beam-plasma interaction (i.e., the ionization laser timing was tuned so that the electron beam arrives immediately after the ionization of lithium vapor and interacts with plasma of the highest possible density). It can be seen that the beam head remains tightly focused, while the rest of the beam experiences a quasi-sinusoidal modulation under the action of the transverse wakefields. Following the first defocussing region, the focusing region has a significantly larger diameter compared to that of the beam head, and that is the reason for the transverse profile observed on the HIGH.Scr5. The second defocusing region of approximately the same amplitude is seen, while the tail of the beam is distorted and the next focusing region cannot be seen.

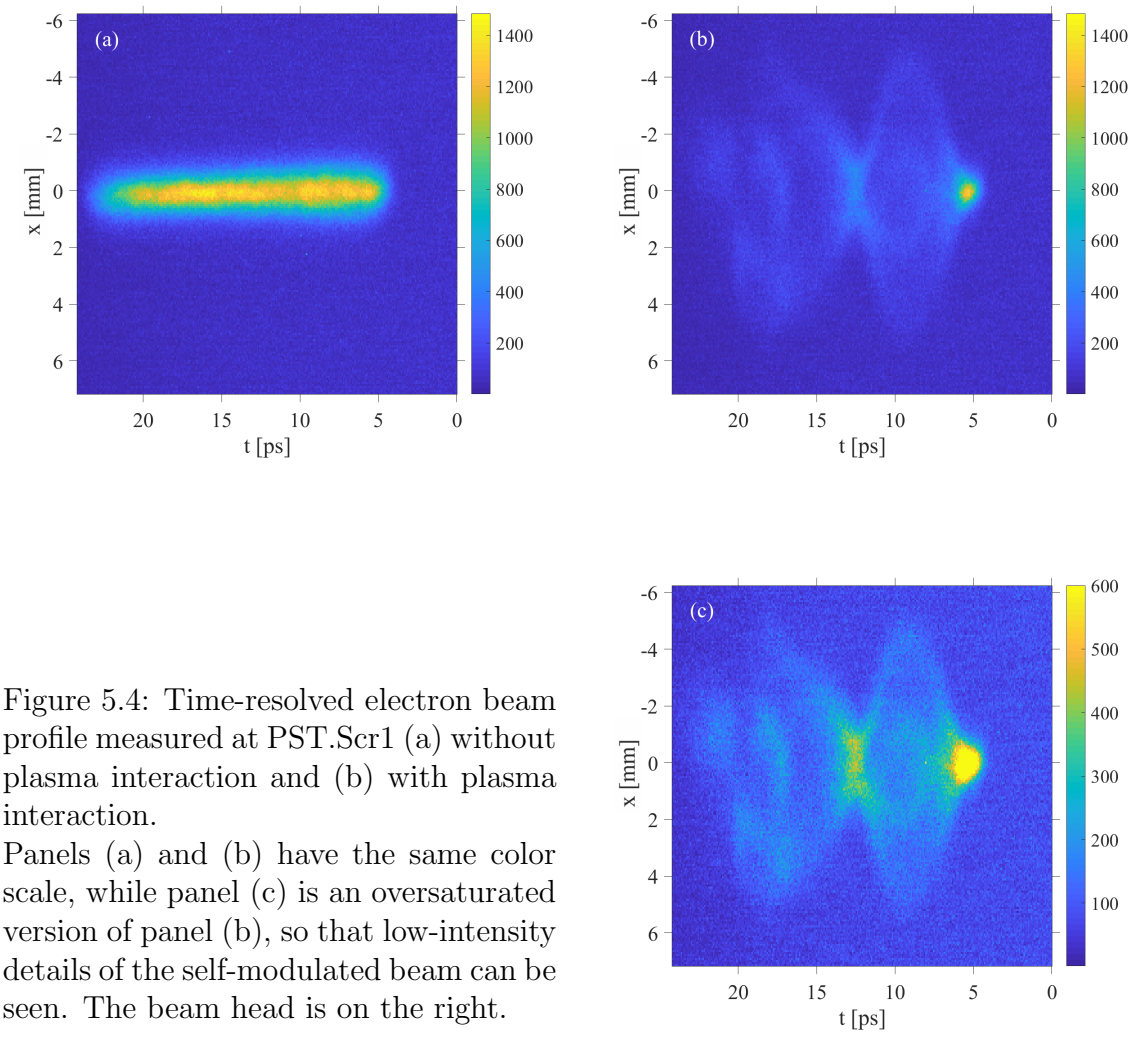

Figure 5.4: Time-resolved electron beam profile measured at PST.Scr1 (a) without plasma interaction and (b) with plasma interaction.
Panels (a) and (b) have the same color scale, while panel (c) is an oversaturated version of panel (b), so that low-intensity details of the self-modulated beam can be seen. The beam head is on the right.

The wavelength of the modulation allows to estimate the plasma density with the

aid of the approximation $n[\mathrm{cm}^{-3}] \approx 1 \times 10^{15}/(\lambda[\mathrm{mm}])^2$ [13]. The distance between the beam head and the first focusing region is approximately 10 ps, and that corresponds to a plasma wavelength of approximately 3 mm or a plasma density of about $1 \times 10^{14}\,\mathrm{cm}^{-3}$ and the electron beam density to plasma density ratio $n_b/n_p \approx 0.2$ (overdense plasma).

5.2.3 Energy modulation

Momentum measurements were conducted using HEDA2 (Fig. 5.5). For this measurement the booster launching phase was changed to -7° with respect to the MMMG phase, resulting in a more pronounced separation of the peaks in the momentum spectrum. For this phase, the measured average momentum was 22.1 MeV/c with an rms momentum spread of 0.24 MeV/c. As can be observed, the central peak of the self-modulated beam energy spectrum has lower energy than the non-modulated beam spectrum. That is because the electron beam acts as a driver and part of its energy is transferred to the plasma. Panel (b) shows how the TDS induced energy spread effects on the momentum projection. Individual momentum peaks are smeared on the projection, but still can be distinguishable on the time-resolved measurement (see below). Note that the induced momentum spread is low for the case without plasma. In that case, the whole beam is focused and goes through the TDS structure close to its axis, while for the self-modulated beam, some parts of the beam are defocused, and thus have larger radii and get higher induced momentum spread in the TDS.

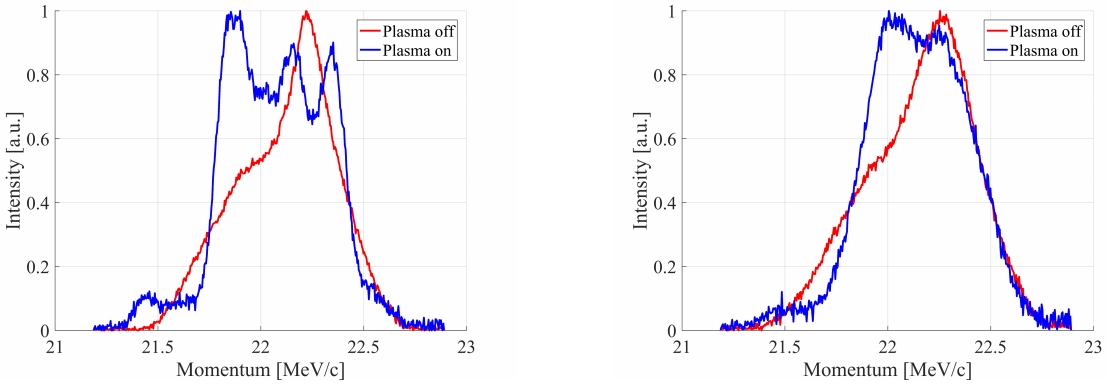

(a) TDS is off (b) TDS is on

Figure 5.5: Electron beam momentum spectra measured with HEDA2.

5.2.4 Longitudinal phase space

The longitudinal phase space (LPS) was measured at Disp3.Scr1. This measurement uses the TDS and HEDA2 spectrometer in order to obtain both temporal and

momentum projections on the screen. For this measurement, the plasma cell temperature was set to 710 °C, so that the lithium vapor density was increased to about $5 \times 10^{15}\,\mathrm{cm}^{-3}$. Without plasma, the LPS of the beam is almost linear, and with plasma, the beam is evidently modulated (Fig. 5.6). An alternation of focused and defocused regions caused by the transverse wakefield component is seen along with the momentum modulation caused by the longitudinal wakefield component. 3 modulation periods correspond to a plasma density of about $1.3 \times 10^{14}\,\mathrm{cm}^{-3}$. The peak to peak momentum modulation is about 400 keV/c.

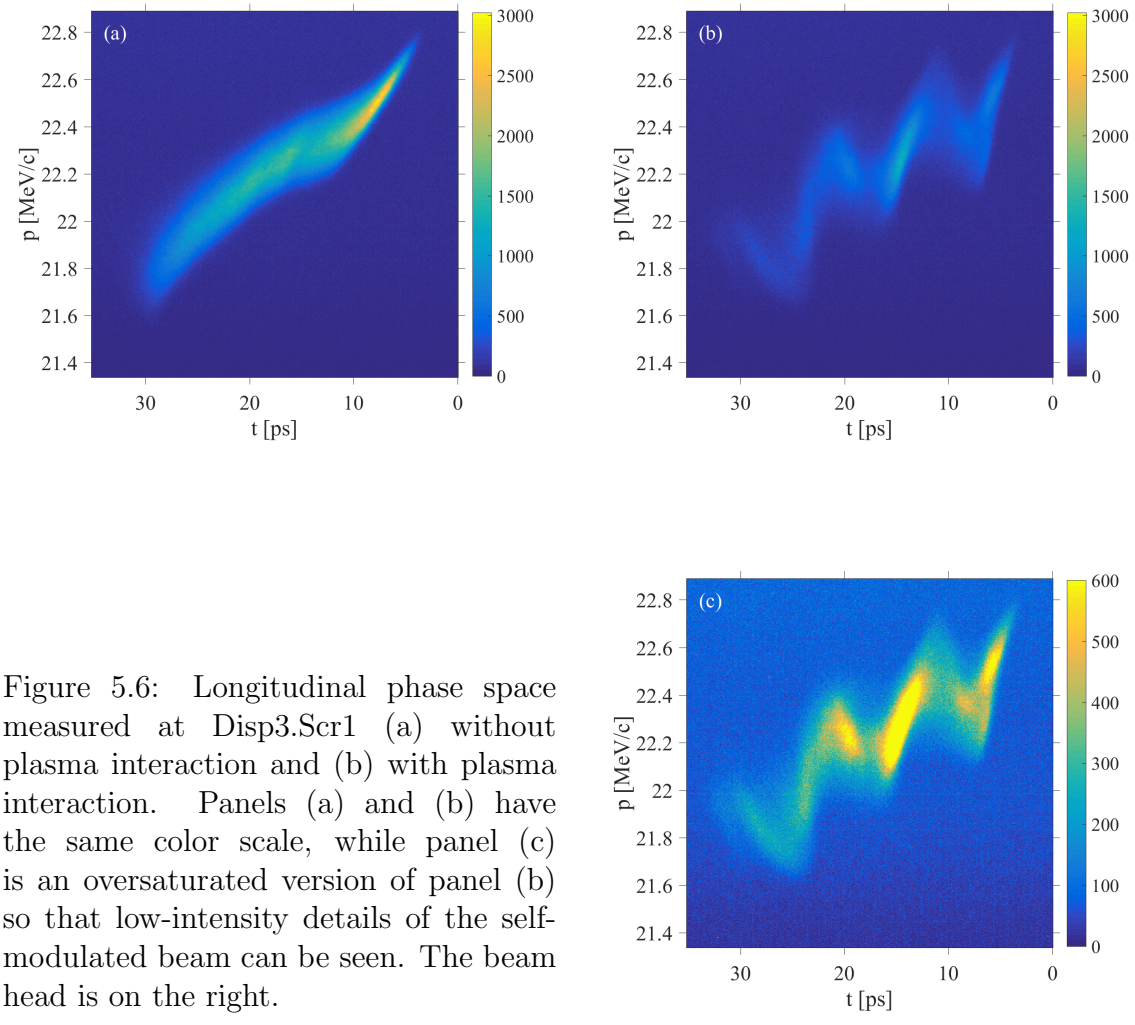

Figure 5.6: Longitudinal phase space measured at Disp3.Scr1 (a) without plasma interaction and (b) with plasma interaction. Panels (a) and (b) have the same color scale, while panel (c) is an oversaturated version of panel (b) so that low-intensity details of the self-modulated beam can be seen. The beam head is on the right.

5.2.5 Plasma density versus laser timing

The ionization laser timing was scanned starting from the initial value in order to vary the delay between plasma generation and the electron beam arrival. Figure 5.7 shows the slice averaged momentum modulation along the electron bunch with respect to the momentum of the beam which has not interacted with plasma (laser delay $= -1\,\mu s$, i.e. the electron beam arrives before the lithium vapor is ionized). It can be seen that the beam head (on the right side) loses energy, while the tail gets accelerated with respect to the energy of the beam that has not interacted with plasma.

At the moment that the plasma is generated, the free electrons have an excess energy of about 1 eV (the lithium ionization potential is 5.39 eV and the energy of the ionization laser photons is 6.43 eV). Thermalization with the neutrals takes place, and then the electrons and ions start to recombine. The energy modulation period follows the plasma density and gets longer with higher delay times. For lower delays, the measured momentum modulation is higher, and thus the maximum longitudinal accelerating field is achieved for highest plasma density.

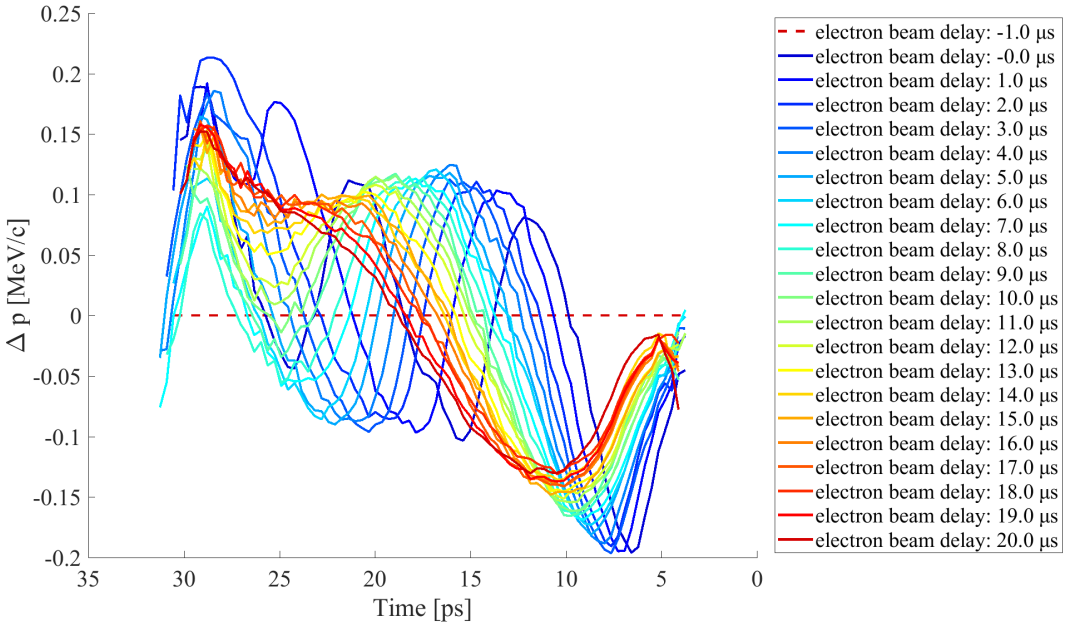

Figure 5.7: Average slice momentum of the self-modulated electron beam with respect to the average slice momentum of the initial beam (dashed line) for different delays between the ionization laser and the electron beam. The electron beam head is on the right.

The plasma density decrease rate depends on the initial neutral vapor density and the ionization rate. Figure 5.8 shows the exponential decrease of the plasma density over time after ionization. Maximum plasma density achieved is about $1.3 \times 10^{14}\,cm^{-3}$,

which is about an order of magnitude lower than the goal density, but sufficient for the SMI to be observed.

The time-resolved transverse beam profile observed on PST.Scr1 exhibits the same behavior: the modulation period grows with the decrease of the plasma density. Several transverse beam profiles are shown on Figs. C.1 and C.2 in Appendix C.

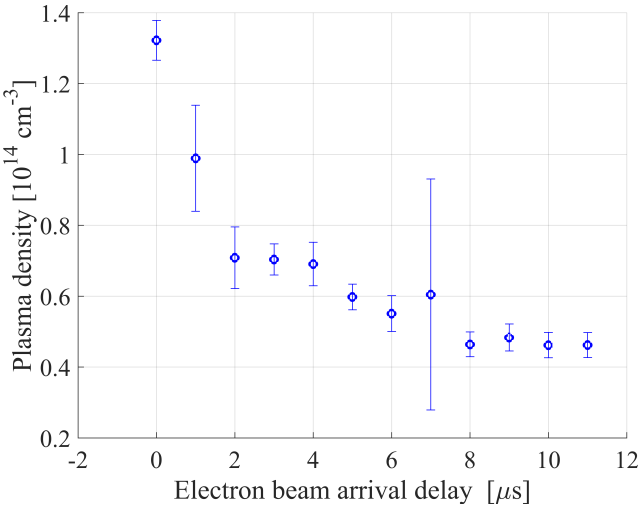

Figure 5.8: Plasma density as a function of the delay between the ionization laser and electron beam arrival times.

5.2.6 Hosing

The hosing instability arguably could be the reason for the modulations observed on Disp3.Scr1 [106]. In case it would be true, the observed modulations represent not a momentum modulation, but a displacement of the electrons due to hosing. A measurement on High2.Scr1 (a screen station located in vicinity of the HEDA2 dipole, $z = 16.303\,\mathrm{m}$) was carried out in order to check the presence of the hosing instability. Figure 5.9 shows electron bunches streaked with the TDS for different plasma densities. The delay indicates the time difference between arrival times of the ionization laser and the electron bunch with respect to the maximum plasma density. No TDS calibration was conducted for these measurements, so there is no timescale for the vertical axis. The beam head is on the top. Some hosing is apparent, but it is evident only on the last third of the beam and cannot be considered as a reason for the modulations along the full bunch as observed in the spectrometer (Fig. 5.6).

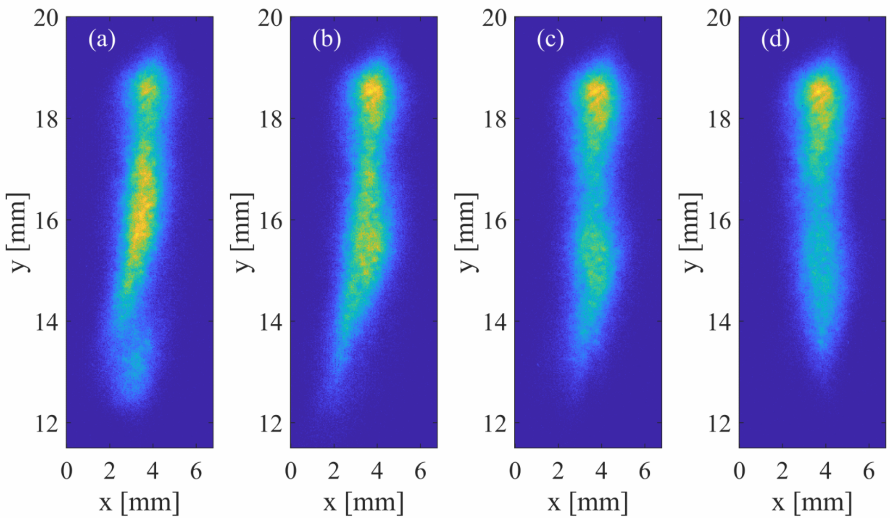

Figure 5.9: Hosing instability observed on High2.Scr1. The delay between the ionization laser and the electron bunch arrival time with respect to the laser timing tuned for the maximum plasma density is 0 µs (a), 1 µs (b), 2 µs (c) and 4 µs (d). The bunch head is on top.

5.3 Conclusions

The experimental results described above are the first direct evidence of the self-modulation of a long (with respect to the plasma wavelength) particle beam in plasma. This has direct importance for the AWAKE experiment, whose working scheme is based on the self-modulation instability. Follow-up experiments can improve understanding of the underlying physics and serve as input for more accurate simulations and analytical models. Table 5.1 gives a comparison of PITZ and AWAKE experimental parameters.

As can be seen, the beam density is small compared to the plasma density in both cases (overdense beam-plasma interaction). The accelerating fields will be determined by the normalized charge per unit length $(n_b/n_p)(k_p\sigma_r)^2$ [108]. In both cases, $(n_b/n_p)(k_p\sigma_r)^2 \approx 0.01$, and excited wakefield is in the linear regime. Since the bunches are long compared to the plasma wavelength (a factor of 2.5 for PITZ and 95 for AWAKE), self-modulation will occur for both cases, seeded by the head of the bunch for PITZ and the ionization front within the bunch for AWAKE. The seed wakefield grows quadratically with respect to the propagation distance and triggers self-modulation instability (see Section 2.7). The number of e-foldings N of the instability growth rate is much larger than one at the end of the bunch for both experiments: $N = 16$ for PITZ and $N = 36$ for AWAKE. Hence, the saturation of the self-modulation instability is expected for both experiments.

While the number of the beam modulations in the PITZ experiment is too low to directly observe the exponential growth of the modulation amplitude, the evolution

Table 5.1: Particle bunch and plasma parameters of the PITZ and AWAKE experiments. The AWAKE parameters are taken from [24, 107]

Parameter	Definition	PITZ	AWAKE
n_b/n_p	Ratio of beam density to plasma density	0.2	0.01
k_p [mm^{-1}]	Plasma wavenumber	2.1	5
L_b [mm] L_b [c/ω_p]	Bunch length	7.5 16	120 600
L_p [mm] L_p [c/ω_p]	Plasma channel length	80 172	10 000 49 795
γ	Lorentz factor of the beam	44.6	427
m_e/M_b	Ratio of electron mass to the mass of the beam particles	1	1/1863
σ_r [mm] σ_r [c/ω_p]	Transverse beam size at the plasma entrance	0.1 0.2	0.2 1
ϵ [mm mrad]	Normalized rms emittance	1	3.5
$\Delta p/p$	Relative momentum spread	0.5 %	0.035 %
β^*_{xy} [mm]	Beta function	200	4900

of the transverse beam profile (Fig. 5.4) strongly indicates the presence of the self-modulation instability. In general, whenever self-modulation is initiated it leads to the SMI development, if the beam is not destroyed by other mechanisms [26]. Figures 5.4 and 5.6 demonstrate the coexistence of the transverse and longitudinal fields, which leads to the seeding if the SMI. The maximum beam radius in the defocusing regions is significantly larger than that of the initial beam. Initial transverse forces in overdense plasma are always focusing (plasma lensing [109]). Since the initial bunch radius (≈ 0.16 mm) is larger than the matched radius in the plasma (0.05 mm), one expects the bunch radius to be less than the initial radius as it undergoes betatron motion [14]. The fact the minimum beam radius in the first focusing region is larger than the initial beam radius indicates that there is a phase slippage between the electron beam and the wakefield, resulting in a sequential action of different phases of the wakefield on the same beam slice. For the experimental parameters, the beam Lorentz factor γ_b is 44.6, while the self-modulation wake Lorenz factor can be estimated (see Section 2.7.2) as $\gamma_p = 2.5$. After a propagation of about 2 cm in plasma the wakefield phase is retarded by π, which prevents tight focusing. The measured ionization laser profile (Fig. 4.21 (b)) indicates that there was a decrease of the plasma density in the second half on the ionization channel. The negative density step results in an elongation of the plasma wavelength and further dephasing.

Besides of the first direct observation of the self-modulation of a long electron beam the experiment at PITZ has also demonstrated strong evidence of the self-modulation instability acting on the beam, which also agrees with the theoretical model for the

PITZ electron beam parameters.

Chapter 6

Simulations

In this chapter, the simulations performed for the self-modulation experiment are presented, including preliminary simulations, which were conducted in order to prepare the first successful experiment, to compare with the obtained experimental results and to optimize the experimental setup for future experiments.

6.1 Preparatory simulations

Initial pre-experiment simulations performed with the particle-in-cell code OSIRIS [110,111] have proven that a successful self-modulation experiment is possible for PITZ-generated long electron beams in $1 \times 10^{15}\,\mathrm{cm}^{-3}$ plasma density and that the properties of the self-modulation are measurable with the combination of the TDS and the HEDA2 dipole [57, 71]. Next, a study regarding a suitable plasma cell position in the PITZ beamline was performed [98] using the particle tracking code ASTRA [112]. The goal of this study was to define a plasma cell location that provides the highest beam density achieved by means of a smooth transverse focusing with quadrupole magnets. The existing PITZ diagnostics infrastructure necessary for other experiments had to be preserved in its place. This study has shown that the optimal position for the plasma cell is 6.1 m downstream of the cathode plane, provided that a second pair of quadrupoles is installed in addition to the existing one upstream of the plasma cell installation place. For this setup, the maximum achievable electron density was $9 \times 10^{12}\,\mathrm{cm}^{-3}$ ($n_b/n_p = 0.01$) for a 100 pC beam. A study of the self-modulation instability development was performed [113] using a particle-in-cell code HiPACE [114]. This study shows that the transverse modulations of the electron beam due to the self-modulation instability are more pronounced for higher electron beam charges, higher plasma densities, and smaller electron beam transverse sizes. Start-to-end simulations of the beam transport for the optimal plasma cell position were performed [115]. Further matching studies with four quadrupole magnets were conducted [85]. In these studies, a 100 pC beam was matched to the plasma cell using MAD-X [116]. Obtained results were verified with the ASTRA code, and only a small discrepancy was found. The

beam scattering effect of the electron windows (Section 4.4.1) was considered in this study. It was shown that without scattering effects a 100 pC beam can be focused down to $xy_{rms} \approx 20\,\mu m$. With an introduced scattering of 0.2 mrad, the minimum matched rms size is about 50 µm. The dependence of the self-modulation instability properties on beam parameters, especially on beam emittance, was considered for a number of experimental setups to find the limitations for the self-modulation instability growth. It was found that the PITZ setup is best suited to avoid emittance-driven erosion [117]. During the preparation experiments (Section 4.4.3), the smallest achievable xy_{rms} beam size was 140 µm for a 100 pC beam and 160 µm for a 750 pC beam. Possible reasons for the discrepancy are a suboptimal beam transport (not ideal alignment of the quadrupoles) in the experiment and limited resolution of the screen (estimated to be about 50 µm [62]). During the experiment, the plasma density was about $1 \times 10^{14}\,cm^{-3}$ and the electron beam charge was 970 pC, while the preliminary SMI simulations were conducted for electron beam charges in the range of 50 to 200 pC and plasma densities between $0.1 \times 10^{15}\,cm^{-3}$ and $4 \times 10^{15}\,cm^{-3}$. The goal of the simulation studies presented in the following sections of this chapter is a comparison with experimentally measured data and the defined optimal conditions for upcoming experiments.

6.2 Simulations of the experiment

In order to track the beam from the cathode position towards the plasma cell, simulations were performed using the particle tracking code ASTRA. Simulations of beam-plasma interactions were performed then using the particle-in-cell code HiPACE with ASTRA particle distributions as input. Particle distributions obtained from the HiPACE simulation were afterwards converted back into the ASTRA format and tracked downstream of the plasma cell to the measurement stations PST.Scr1 and Disp3.Scr1. Scattering at the entrance foil of the plasma cell was not included for ease of the simulation. Modern day computers are not powerful enough to simulate the evolution of an ensemble consisting of 5×10^9 electrons (1 nC). In order to speed up computation, simulations are performed with macroparticles. Each macroparticle represents a group of particles and has the same charge to mass ratio as a single particle. Most of the simulations were done with 200 000 macroparticles, while some of the final simulations were repeated with 1 000 000 macroparticles. These simulations showed similar results as the ones with the lower number of macroparticles, demonstrating that 200 000 macroparticles is a sufficiently high number to avoid significant numerical errors.

6.2.1 Beam transport to the plasma cell

ASTRA (A Space charge TRacking Algorithm) code performs tracking of charged particles through user-defined external fields: electromagnetic fields in RF cavities,

solenoid, dipole and quadrupole magnetic fields. The code considers not only external fields but also the internal space charge field of the particle cloud. The space charge field can be calculated in 2D-cylindrical symmetry or in 3D. The 2D-cylindrical space charge mode was used to track the beam to the position $z = 4.61\,\mathrm{m}$ (booster exit), as all input parameters and fields are cylindrically symmetric until that point. Downstream of the booster exit the full 3D space charge routine was enabled, as the beam was focused with quadrupole magnets. For the start-to-end simulation, the ideal temporal flat-top distribution was modified accordingly to the TDS measurement of the current distribution on PST.Scr1. Figure 6.1 (a) shows the electron beam temporal profile measured during the experiment (Chapter 5). The rise time (the time the signal takes to increase from 10 % to 90 % reference levels) is 2 ps. Figure 6.1 (b) shows the temporal distribution of the ASTRA input beam. Simulation parameters were set to repeat experimental conditions: the bunch charge was set to 970 pC, the electrical fields in the gun and the booster were tuned so that the beam momentum was 6.5 MeV/c after the gun at the MMMG phase and 22.3 MeV/c after the booster at the MMMG phase, the initial High1.Q1-High1.Q4 quadrupole settings were adopted from [85] and fine-tuned to find the optimum focusing at the beginning of the plasma channel and fixed. Figure 6.2 shows the x_{rms} and y_{rms} sizes along the beamline for the gun solenoid current of 390 A (a) and the x_{rms} and y_{rms} sizes and the electron beam density at the beginning of the plasma channel ($z = 6.21\,\mathrm{m}$) as a function of the main solenoid current (b). The beam density is calculated as the ratio of the total number of electrons in the beam to the beam volume, $n_b = n/V$, where the total number of electrons is $n = 970\,\mathrm{pC}/e$, and the beam volume is $V = \pi \cdot xy_{rms}^2 \cdot z_{rms}/4$. The maximum beam density is achieved for the solenoid current $\mathrm{I_{main}} = 391\,\mathrm{A}$. The electron beam symmetry changes slightly with the solenoid focusing. The maximum absolute difference between the horizontal and vertical sizes is 12 µm, while the highest relative asymmetry $|x_{rms} - y_{rms}|/\max(x_{rms}, y_{rms})$ is about 11 % for $\mathrm{I_{main}} = 392\,\mathrm{A}$. For the solenoid currents of 389 A and 395 A the beam is symmetric. As the simulation does not include scattering on the electron window, the minimum xy_{rms} spot size is lower than that in the experiment: about 80 µm in the simulation compared to 165 µm measured for a 750 pC electron beam.

6.2.2 Simulations of the beam-plasma interaction

The Highly efficient Plasma ACcelerator Emulation (HiPACE) is a quasi-static and fully parallelized particle-in-cell (PIC) code [114, 118]. In PIC codes, the simulation space is split on a 3D grid. Maxwell's equations are solved on the grid for initial conditions: macroparticle distributions and currents and initial electromagnetic fields. As Maxwell's equations are solved, the fields are updated on the grid and particles are moved according to the equations of motion in the electromagnetic fields. Together with the motion of the particles, new charge density distributions and currents are obtained. They serve as initial conditions for the next step of the simulation. In fully explicit PIC codes Maxwell's equations are solved by means of the finite-difference time-

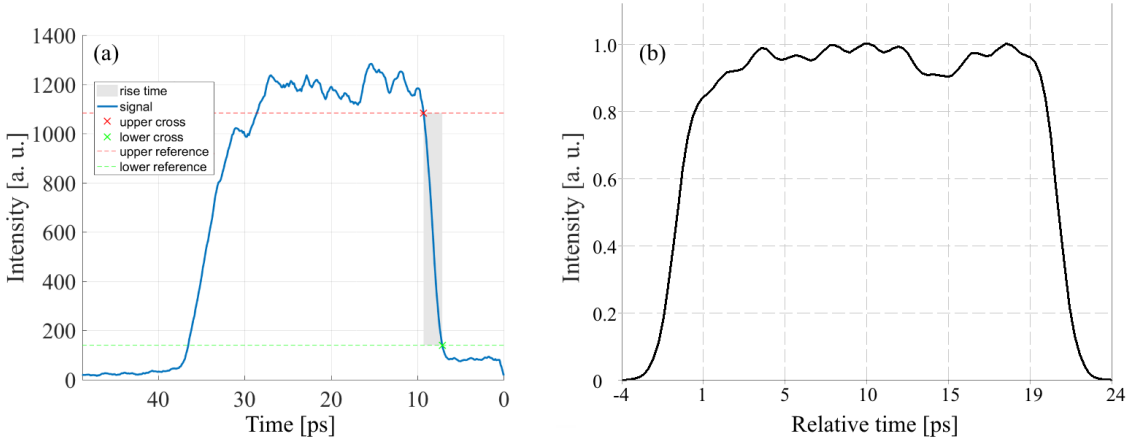

Figure 6.1: (a): The temporal electron beam distribution measured at the screen station PST.Scr1 during the experiment (same shown in Figure 5.2 (b)). The rise time is about 2 ps. (b): The initial temporal electron beam distribution for ASTRA simulations. The temporal profile is tailored to repeat the experimentally measured beam profile. Bunch heads are on the right.

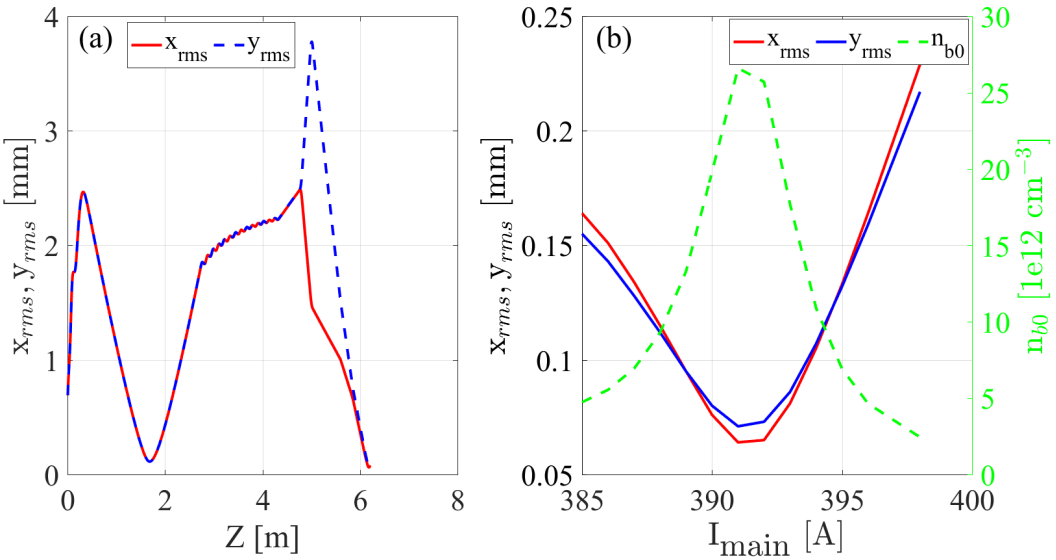

Figure 6.2: (a): Transverse electron beam sizes along the beamline for the beam transport to the plasma cell. Solenoid current $I_{main} = 390$ A. (b): Transverse electron beam sizes and electron beam density n_{b0} at the beginning of the plasma channel as a function of the main solenoid current. Emittance optimization was not performed. Scattering at the entrance foil of the plasma cell was not included for ease of simulation.

domain method [119]; spatial and temporal resolutions are coupled and the maximum simulation time step is limited by the stability requirements of the partial differential

equations solutions – the Courant-Friedrichs-Lewy condition [120]. In the quasi-static approach [121] plasma and beam macroparticles are treated separately. This is possible if the particle beam charge distribution does not evolve significantly as it traverses a plasma volume element. In this case, the time step size can be larger than in the explicit PIC codes. The HiPACE code employs the difference between the characteristic response time of plasma ($1/\omega_p$) and the characteristic response time of a relativistic beam ($1/\omega_\beta \sim \sqrt{2\gamma}/\omega_p$ [122], where ω_β is the betatron frequency). For a simulation step, first the beam particles are considered static, while the evolution of the plasma particles and fields is calculated, then the plasma particles and fields are frozen, and the beam particles are propagated [114]. HiPACE dynamically adjusts the time step to maintain consistent beam dynamics at the lowest amount of computation work. At the beginning of the simulation, the particle beam is initialized directly within the plasma, and self-consistent field information is calculated for its initial position. The natural unit of length in the HiPACE simulation is the inverse plasma wavenumber $k_p^{-1} = c/\omega_p$. A moving window algorithm is implemented in HiPACE: the window (the simulation box) moves with the same speed as the electron beam, so the beam position remains fixed within the window, while plasma particles are moved backwards with respect to the window. The simulations were performed for the particle distributions obtained from ASTRA for different solenoid strengths. Electron beams were propagated through plasma channels with densities n_p of $1 \times 10^{14}\,\mathrm{cm}^{-3}$ and $1 \times 10^{15}\,\mathrm{cm}^{-3}$ – these values correspond to experimentally achieved and goal densities, respectively. Basic parameters of the simulations are listed in Table 6.1. Certain parameters are listed both in metric and plasma units. The range of values shows how much a parameter changes for different input distributions (electron beams tracked by ASTRA with $\mathrm{I_{main}}$ from 385 A to 398 A). Transverse beam radius $\sigma_r = xy_{rms}$, the FWHM length, the beam momentum p_z, the momentum spread $\Delta p_z/p_z$, the Lorenz factor γ, and electron densities n_b are obtained from the ASTRA distributions mentioned previously. The maximum length of the plasma channel L_{plasma} is defined by the plasma cell design. The simulation window size is selected to accommodate the beam even if it is heavily modulated transversely. The simulation resolution is derived from the simulation windows size and the simulation grid size of $512 \times 256 \times 256$.

Table 6.1: Parameter range for the HiPACE simulations. See text for explanations of the parameters.

n_p [cm^{-3}]	1×10^{14}	1×10^{15}
σ_r [µm] σ_r [c/ω_p]	67 - 223 0.13 - 0.42	67 - 223 0.4 - 1.32
FWHM length [mm] FWHM length [c/ω_p]	6.9 13	6.9 41
p_z [MeV/c] $\Delta p_z/p_z$ [%] γ	22.3 0.35 44.4	22.3 0.35 44.4
n_b [cm^{-3}] n_b/n_p	2.7×10^{13} - 2.7×10^{12} 0.27-0.027	2.7×10^{13} - 2.7×10^{12} 0.027-0.0027
L_{plasma} [mm] L_{plasma} [c/ω_p]	80 150	80 480
Moving window size [mm^3]	$10.6 \times 2.1 \times 2.1$	$10.8 \times 3.4 \times 3.4$
Resolution $[k_p\Delta z, k_p\Delta x, k_p\Delta y]$	0.039, 0.016, 0.016	0.125, 0.078, 0.078

Although Fig. 6.2 (b) shows that the highest beam density at $\mathrm{I_{main}} = 391\,\mathrm{A}$, a comparison of profiles for different solenoid currents (see Figs. C.3 and C.4 in Appendix C) indicates that $\mathrm{I_{main}} = 393\,\mathrm{A}$ has a waist in the middle of the beam and its peak charge density is only slightly lower than that of the 391 A beam. Figure 6.3 shows beam density distributions at the beginning of the plasma channel for three solenoid currents: 385 A, 393 A, and 396 A. The electron beam density is normalized to the plasma density of $1 \times 10^{14}\,\mathrm{cm^{-3}}$. These distributions represent three focusing cases and they will be reviewed in the following sections. All conducted simulations generally fall within one of the possible focusing cases: underfocused beams ($\mathrm{I_{main}}$ =385 to 392 A) with two focused regions along the beam, a tightly focused beam ($\mathrm{I_{main}} = 393\,\mathrm{A}$) with one focused region in the middle, and overfocused beams ($\mathrm{I_{main}} = 394$ to 398 A) with a nearly homogenous charge density distribution along the beam. For $\mathrm{I_{main}} = 385\,\mathrm{A}$ (Fig. 6.3 (a)), the beam charge distribution in the middle part of the bunch has a low ($n_b/n_p < 0.3$) and uniform density, while beam head and tail are tightly focused ($n_b/n_p > 2$). For $\mathrm{I_{main}} = 393\,\mathrm{A}$ (Fig. 6.3 (b)), the beam is tightly focused, a large part of the beam has a density $n_b/n_p > 1$ with an about 3 k^{-1} long region in the middle with a charge density of about $1 \times 10^{15}\,\mathrm{cm^{-3}}$. For $\mathrm{I_{main}} = 396\,\mathrm{A}$ (Fig. 6.3 (c)), the beam is overfocused, it has low charge density and the charge density distribution along the beam is almost uniform. For the underfocused and tightly focused beams, longitudinal variations of charge density lead to a non-linear evolution of the wakefields in plasma.

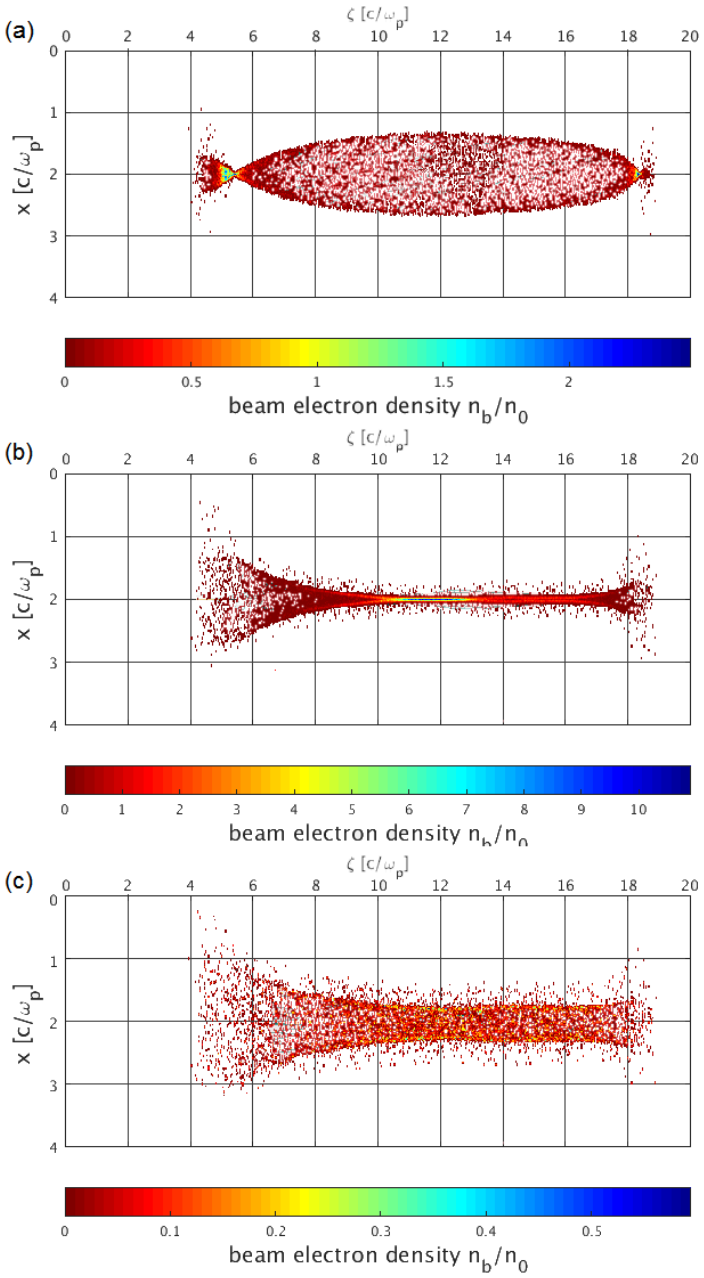

Figure 6.3: Longitudinal electron beam profiles for different solenoid strengths at the beginning of the plasma channel obtained from ASTRA simulations. Beam head is on the right. The beam electron density is normalized to $n_p = 1 \times 10^{14}\,\mathrm{cm}^{-3}$. Length units are given for a plasma density of $1 \times 10^{14}\,\mathrm{cm}^{-3}$. (a): Solenoid current $\mathrm{I_{main}} = 385\,\mathrm{A}$, the electron beam is underfocused, but its head and tail are tightly focused and have densities up to $2.5 \times 10^{14}\,\mathrm{cm}^{-3}$. (b): For $\mathrm{I_{main}} = 393\,\mathrm{A}$, the beam is tightly focused and the maximum beam density is higher than $1 \times 10^{15}\,\mathrm{cm}^{-3}$. (c): For $\mathrm{I_{main}} = 396\,\mathrm{A}$, the beam is overfocused and its density does not change significantly along the beam.

The divergence/convergence of the input beams does not change significantly within the solenoid scan range, and the beam evolution is dominated by the plasma focusing. The next sub-chapters mostly deal with the three focusing cases described above, while the HiPACE simulation results for various solenoid currents are shown in Appendix C. The $1 \times 10^{14}\,\mathrm{cm}^{-3}$ case was studied in details, as it is closer to the experimental conditions.

6.2.2.1 Longitudinal accelerating fields

Figure 6.4 shows longitudinal accelerating fields E_z directly after the initialization of the electron beam in plasma (the propagation distance in plasma is zero). For $1 \times 10^{14}\,\mathrm{cm}^{-3}$ plasma density, the maximum initial E_z field amplitude is driven by the tightly focused beam ($\mathrm{I_{main}} = 393\,\mathrm{A}$). It can be seen that the wakefield generated by the underfocused beam ($\mathrm{I_{main}} = 385\,\mathrm{A}$) develops a bit earlier along the beam. The beam head is tightly focused in this case and serves as a better seed for the initial field. For $1 \times 10^{15}\,\mathrm{cm}^{-3}$ plasma density, the initial field profiles differ markedly. The density of the beam front for the overfocused beam ($\mathrm{I_{main}} = 396\,\mathrm{A}$) is the lowest among the examined cases and it generates the lowest initial field amplitude. The density of the tightly focused beam ($\mathrm{I_{main}} = 393\,\mathrm{A}$) rises smoothly from its front to the middle, so the whole first half of the beam acts like a driver and the beam front is not very sharp which results in a moderate initial field amplitude. The underfocused beam ($\mathrm{I_{main}} = 385\,\mathrm{A}$) has a dense head which seeds the wakefield very effectively in comparison to other cases.

Figure 6.5 shows the evolution of the first maximum of the E_z field behind the electron beam as a function of the distance propagated in plasma.

For the underfocused beam ($\mathrm{I_{main}} = 385\,\mathrm{A}$), the field amplitude grows fast with the propagation of the beam through the plasma, but decreases almost to initial values soon. The seed wakefield starts the instability, however, the inhomogeneity of the beam density profile quickly prevents the instability growth.

For the ($\mathrm{I_{main}} = 393\,\mathrm{A}$) case, the field amplitude does not evolve significantly in $1 \times 10^{14}\,\mathrm{cm}^{-3}$ plasma, as the self-modulation instability does not start for the overdense beam. The beam density in its middle part is $n_b/n_p > 10$ resulting in expulsion of plasma electrons and formation of an ion channel along the beam axis and entering a non-linear regime where the theory described in Chapter 2 is not valid. As mentioned above, the scattering on the electron windows was not taken into account for the simulation, and in the experiment the xy_{rms} spot size is estimated to be twice as large than that for the $\mathrm{I_{main}} = 393\,\mathrm{A}$ simulation case, so this case does not correspond to the experimental conditions and no overdense beam interaction was observed in the experiment. In $1 \times 10^{15}\,\mathrm{cm}^{-3}$ plasma, the E_z field amplitude grows rapidly and saturates after propagating about 20 mm in the plasma.

The overfocused beam ($\mathrm{I_{main}} = 396\,\mathrm{A}$) demonstrates a behavior similar to that shown in [57, 113]: exponential growth and saturation after having traveled some distance through plasma, although in $1 \times 10^{15}\,\mathrm{cm}^{-3}$ plasma, after the instability

saturates at the propagation distance of about 40 mm and E_z reaches its maximum, the amplitude decreases similarly to the simulation results shown for uniform plasma profiles in [42]. It is possible to mitigate such a decrease of the established wakefield amplitude with density steps in the plasma channel [42].

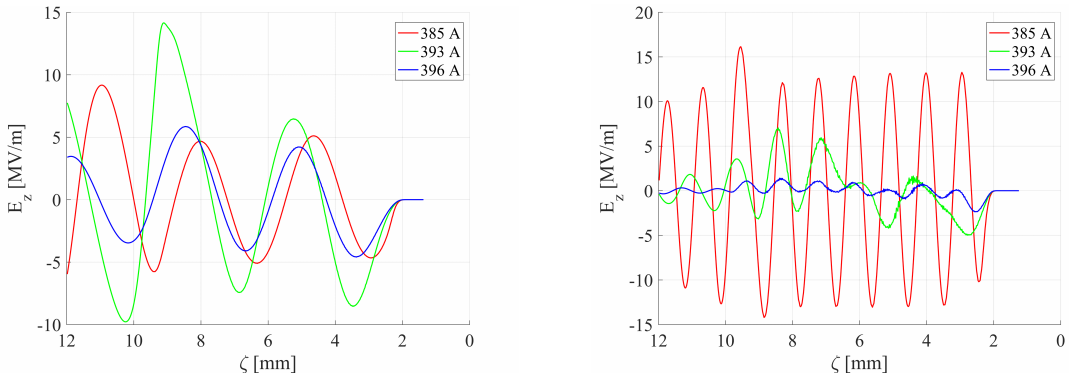

(a) Plasma density is $1 \times 10^{14}\,\mathrm{cm}^{-3}$ (b) Plasma density is $1 \times 10^{15}\,\mathrm{cm}^{-3}$

Figure 6.4: Initial longitudinal accelerating electric fields E_z for different beam focusing. The beam head is on the right. The beam starts at $\zeta \approx 2\,\mathrm{mm}$.

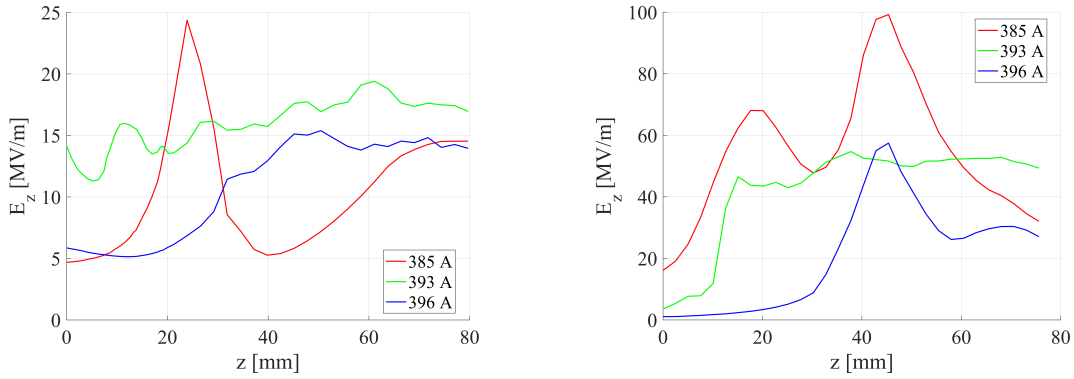

(a) Plasma density is $1 \times 10^{14}\,\mathrm{cm}^{-3}$ (b) Plasma density is $1 \times 10^{15}\,\mathrm{cm}^{-3}$

Figure 6.5: Evolution of the first maximum of the longitudinal electric field E_z behind the electron beam as a function of the distance propagated in plasma.

Dephasing with respect to the initial phase at the position of the first E_z field peak behind the electron beam as a function of the distance propagated in plasma is shown in Fig. 6.6. The strongest dephasing corresponds to the exponential growth of the field during the SMI development.

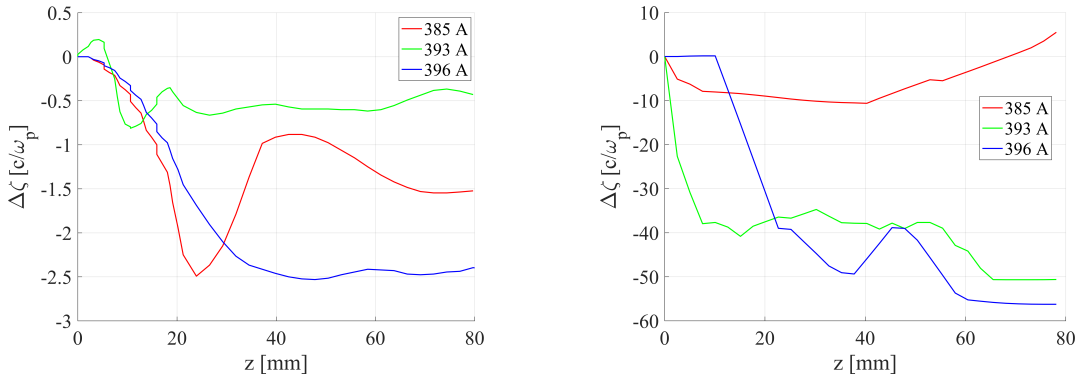

(a) Plasma density is $1 \times 10^{14}\,\mathrm{cm}^{-3}$ (b) Plasma density is $1 \times 10^{15}\,\mathrm{cm}^{-3}$

Figure 6.6: Dephasing at the position of the first maximum of the longitudinal electric field E_z behind the electron beam as a function of the distance propagated in plasma.

Dephasing indicates the instability development for the tightly focused beam ($\mathrm{I_{main}} = 393\,\mathrm{A}$) in $1 \times 10^{15}\,\mathrm{cm}^{-3}$ plasma and for the overfocused beam ($\mathrm{I_{main}} = 396\,\mathrm{A}$) in both plasma density cases.

6.2.2.2 Transverse wakefields

Initial transverse $E_x - B_y$ field profiles are shown in Fig. 6.7. The fields are normalized to the cold-nonrelativistic wavebreaking field $E_0 = \omega_p mc/e$ [123]. Negative field values correspond to focusing, and positive values correspond to defocusing. The initial fields and their evolution strongly depend on the initial charge density distribution and differ a lot for the aforementioned focusing cases.

For the underfocused beam ($\mathrm{I_{main}} = 385\,\mathrm{A}$), the initial transverse fields are of a sinusoidal shape, but due to the inhomogeneous beam density profile, the instability feedback mechanism does not work properly. Additionally, in $1 \times 10^{14}\,\mathrm{cm}^{-3}$ plasma, the fields generated by the overdense beam head are not linear. The tightly focused beam ($\mathrm{I_{main}} = 393\,\mathrm{A}$) is subjected only to focusing fields for the $1 \times 10^{14}\,\mathrm{cm}^{-3}$ case (underdense plasma lensing [109]). In $1 \times 10^{15}\,\mathrm{cm}^{-3}$ plasma, the profile of initial transverse fields is sinusoidal only in the second half of the beam. As the beam density grows from the head to the middle, the whole first half of the beam acts as a driver, and the self-modulation instability develops only over the second half of the beam. For the overfocussed beam ($\mathrm{I_{main}} = 396\,\mathrm{A}$), the initial transverse fields are of low amplitude and of regular sinusoidal shapes.

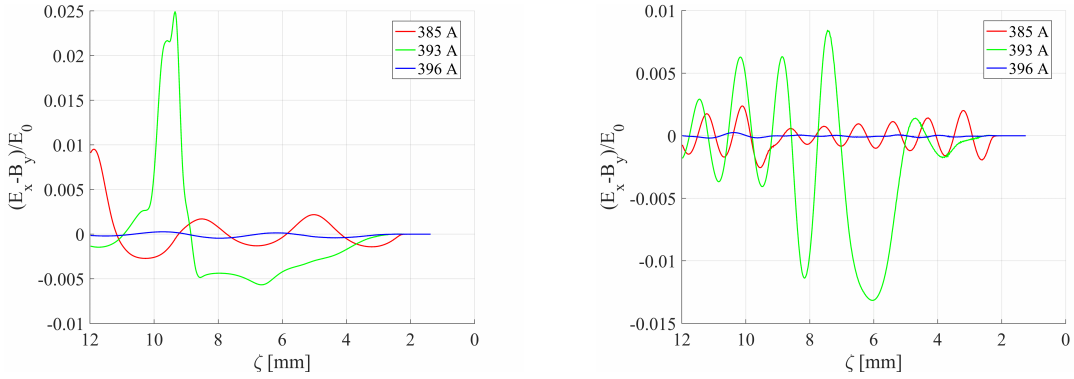

(a) Plasma density is $1 \times 10^{14}\,\mathrm{cm}^{-3}$ (b) Plasma density is $1 \times 10^{15}\,\mathrm{cm}^{-3}$

Figure 6.7: Initial transverse focusing field profiles for three different focusing cases. The beam head is on the right. The beam starts at $\zeta \approx 2\,\mathrm{mm}$. Negative values correspond to focusing fields.

Figure 6.8 shows initial transverse wakefields for three overfocused beams (distribution shapes correspond to Fig. 6.3 (c), the transverse beam size increases and the charge density decreases with growing solenoid current). This range is interesting since the sinusoidal shape indicates that these cases are in the linear regime. The field amplitudes are of the same order, while for lower solenoid currents they are higher.

Figure 6.9 shows the evolution of the transverse wakefields for these beams. The evolution of the longitudinal electric field as a function of the distance propagated in plasma is shown in thin dashed lines in the same plots. It is seen that the character of the transverse wakefield component evolution is similar to that of the longitudinal wakefield component. In the $1 \times 10^{15}\,\mathrm{cm}^{-3}$ plasma, the exponential growth of the SMI for the beam distributions obtained with higher main solenoid values is less pronounced and takes more distance since the beam density n_b/n_p is an order of magnitude lower compared to the $1 \times 10^{14}\,\mathrm{cm}^{-3}$ case and the transverse beam sizes are larger with respect to the plasma wavelength ω_p. For $\mathrm{I_{main}} = 398\,\mathrm{A}$, the $k_p\sigma_r \ll 1$ condition is not fulfilled and the current filamentation instability dominates over the SMI (see Fig. C.10 in Appendix C).

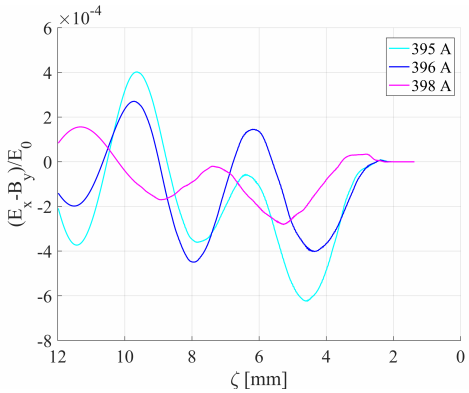

(a) Plasma density is $1 \times 10^{14}\,\mathrm{cm}^{-3}$

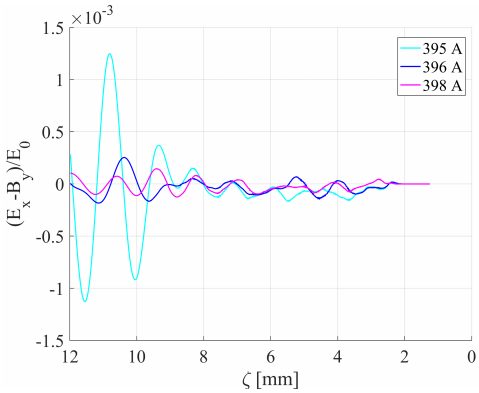

(b) Plasma density is $1 \times 10^{15}\,\mathrm{cm}^{-3}$

Figure 6.8: Initial transverse focusing field profiles for three overfocused beams. Beam head in on the right. A complete simulation box is shown, the beam starts at $\zeta \approx 2\,\mathrm{mm}$. Negative values correspond to focusing fields.

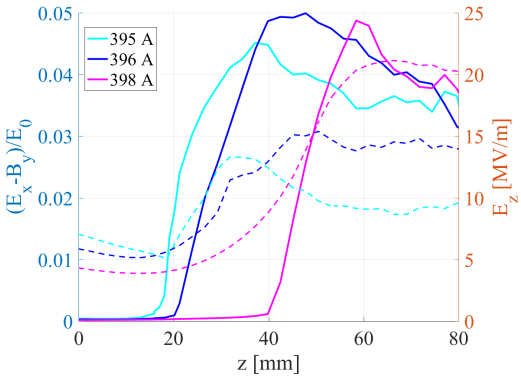

(a) Plasma density is $1 \times 10^{14}\,\mathrm{cm}^{-3}$

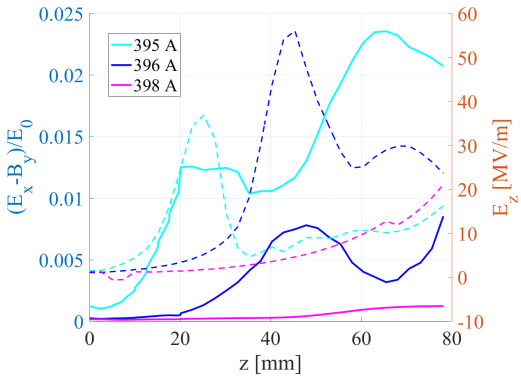

(b) Plasma density is $1 \times 10^{15}\,\mathrm{cm}^{-3}$

Figure 6.9: Maximum transverse wakefields along the simulation box as a function of distance propagated in plasma (solid lines) compared to the evolution of the first maximum of the E_z field behind the electron beam (dashed lines).

6.2.2.3 Hosing instability

Theory predicts comparable growth rates for the SMI and hosing instabilities for long electron beams in overdense plasmas [38]. In order to render predominance of the SMI over the hosing instability, the former instability is strongly seeded by a sharp rise front of the electron beam, while the seeding of the latter should be avoided by means of minimizing the beam tilt with respect to its direction of propagation in plasma and symmetrizing the beam (see Chapter 2 and [14]). Only slight hosing was observed in the experiment (Section 5.2.6). In the simulations, the hosing instability develops faster for tightly focused beams and is less pronounced for overfocused beams. In $1 \times 10^{14}\,\mathrm{cm}^{-3}$

plasma, the distance to develop strong hosing instability is much larger than the plasma channel length, however, in $1 \times 10^{15}\,\mathrm{cm}^{-3}$ plasma, hosing develops within the plasma channel length (see Fig. C.9 in Appendix C). Figure 6.10 shows the evolution of two beam slices close to the beam tail with their propagation through the plasma channel (horizontal axis). Error bars represent rms transverse slice sizes.

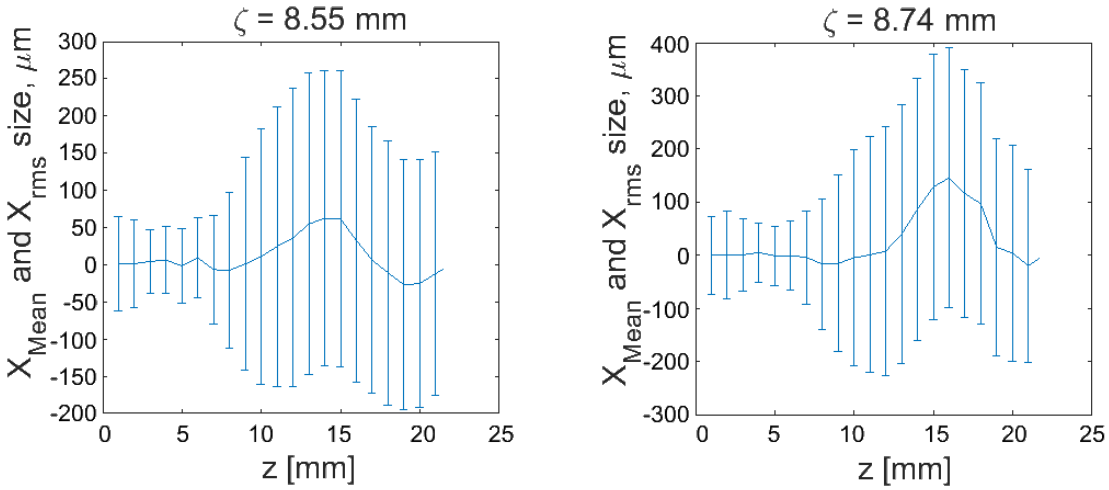

Figure 6.10: The hosing instability development in the tail of the tightly focused beam ($\mathrm{I_{main}} = 393\,\mathrm{A}$) in $1 \times 10^{15}\,\mathrm{cm}^{-3}$ plasma. The distance propagated in plasma is plotted on the horizontal axis. Error bars show the slice rms transverse size.

No special optimizations were carried out to mitigate the hosing development. Possible hosing seeds are slight asymmetries of input distributions. To ensure that hosing is not caused by a numerical instability, simulations were repeated with 1×10^6 macroparticles. Additional simulations were conducted with perfectly symmetric input distributions, and no hosing was observed.

6.2.3 Evolution of the transverse size and the longitudinal phase space of the electron beam after the plasma cell

In this section the measurement for the $1 \times 10^{14}\,\mathrm{cm}^{-3}$ case are simulated. The measurements were carried out at the PST.Scr1 and Disp3.Scr1 stations, and the HiPACE particle distributions after passing through plasma were converted back to the ASTRA format and tracked down the beamline to these measurement stations. The exact beam trajectory from the experiment was not reproduced, as the goal of the simulation was to only reproduce beam sizes at the positions of the PST.Scr1 and High2.Scr2 screen stations, while keeping reasonable beam sizes inside the TDS and the HEDA2 dipole [51].

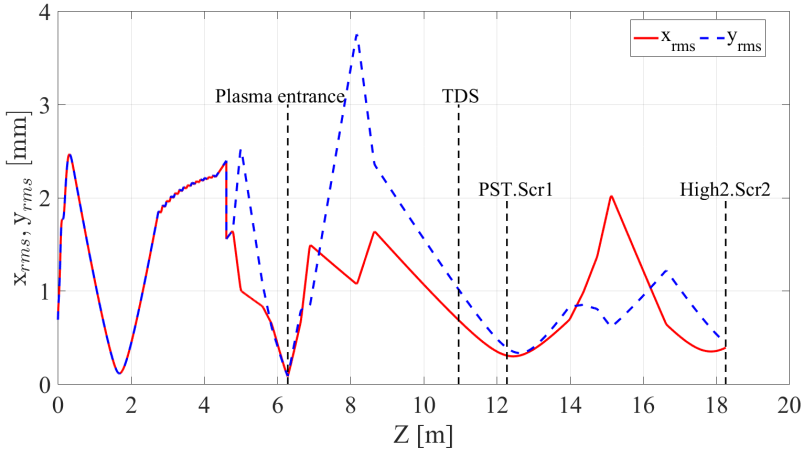

Figure 6.11: Transverse beam sizes along the beamline for the beam transport to the measurement screens PST.Scr1 and High2.Scr2 for the $I_{main} = 393\,A$ beam. Corresponding xy_{rms} sizes: at the plasma entrance ($z = 6.21\,m$) $\rightarrow$ 80 µm, at the TDS ($z = 10.96\,m$) $\rightarrow 1.3\,mm$, at PST.Scr1 ($z = 12.28\,m$) $\rightarrow 0.343\,mm$, at High2.Scr2 ($z = 18.26\,m$) $\rightarrow 0.41\,mm$.

6.2.4 Simulating the measurements of the longitudinal particle distribution and the longitudinal phase space

In the following sections simulations of measurements at PST.Scr1 and Disp3.Scr1 are presented. There are two types of figures presented in these sections: ones with white background show beam properties rendered directly from ASTRA output distributions tracked to certain positions without the TDS streaking and the dipole magnetic field applied and others with blue background show beam properties obtained from the simulated measurement, i.e., they represent the X-Y projections of ASTRA output distributions tracked down to measurement stations with the TDS streaking (for measurements at both screen stations) enabled and the sector bending magnet transfer matrix [124] (for Disp3.Scr1 measurements) applied. For these figures, the image resolution and intensity range are the same as characteristics of the corresponding measurement station's optical systems. No noise is included in the simulated images; instead, a background of these images is shown blue, so low-intensity parts of the images are less evident. These simulations were carried out in order to confirm that the obtained experimental data properly represent features of the beam-plasma interaction which takes place several meters upstream of the measurement stations.

6.2.4.1 Longitudinal particle distribution at PST.Scr1

Figure 6.12 shows the simulation of the TDS measurement for electron beams without plasma interaction. Beam distributions at the entrance of the plasma channel

($z = 6.21\,\mathrm{m}$) are shown in the first row. The second row shows the corresponding beam distributions at the PST.Scr1 position ($z = 12.278\,\mathrm{m}$) without the TDS switched on, and the last row shows transverse beam distributions at the PST.Scr1 position obtained with the TDS switched on.

The projections are similar to the initial distributions shown in Fig. 6.3, however, for $\mathrm{I_{main}} = 393\,\mathrm{A}$ the beam is not tightly focused in the middle anymore because of strong space-charge forces. It can be seen that all beam features are present on the images obtained from the simulated measurement, although some low-intensity details, like the beam halo for the $\mathrm{I_{main}} = 393\,\mathrm{A}$ case, may be lost.

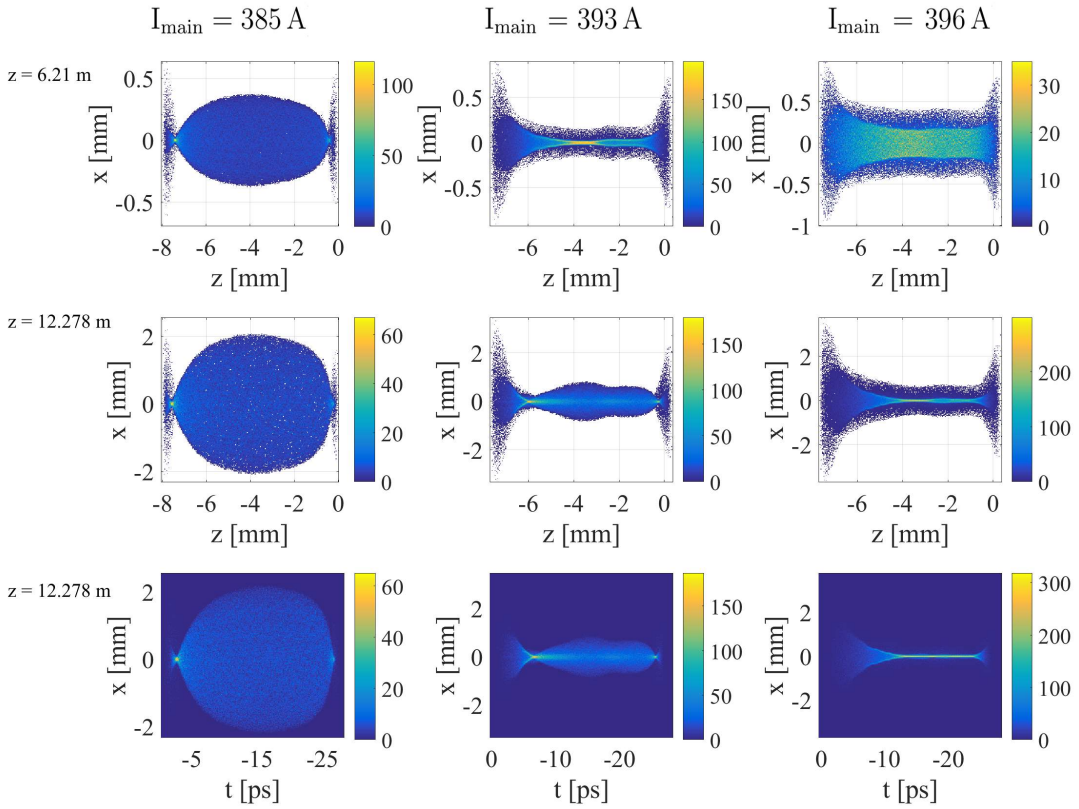

Figure 6.12: Simulated longitudinal beam profile measurement at PST.Scr1 without beam-plasma interaction. The beam head is on the right. Compare with charge density profiles in Fig. 6.3.

Figure 6.13 shows the simulation of the TDS measurement for electron beams after propagating 80 mm in $1 \times 10^{14}\,\mathrm{cm^{-3}}$ plasma. Beam distributions at the exit of the plasma channel ($z = 6.29\,\mathrm{m}$) are shown in the first row. The second row shows corresponding beam distributions at the PST.Scr1 position ($z = 12.278\,\mathrm{m}$) without the TDS switched on, and the last row shows transverse beam distributions at the PST.Scr1 position obtained with the TDS switched on.

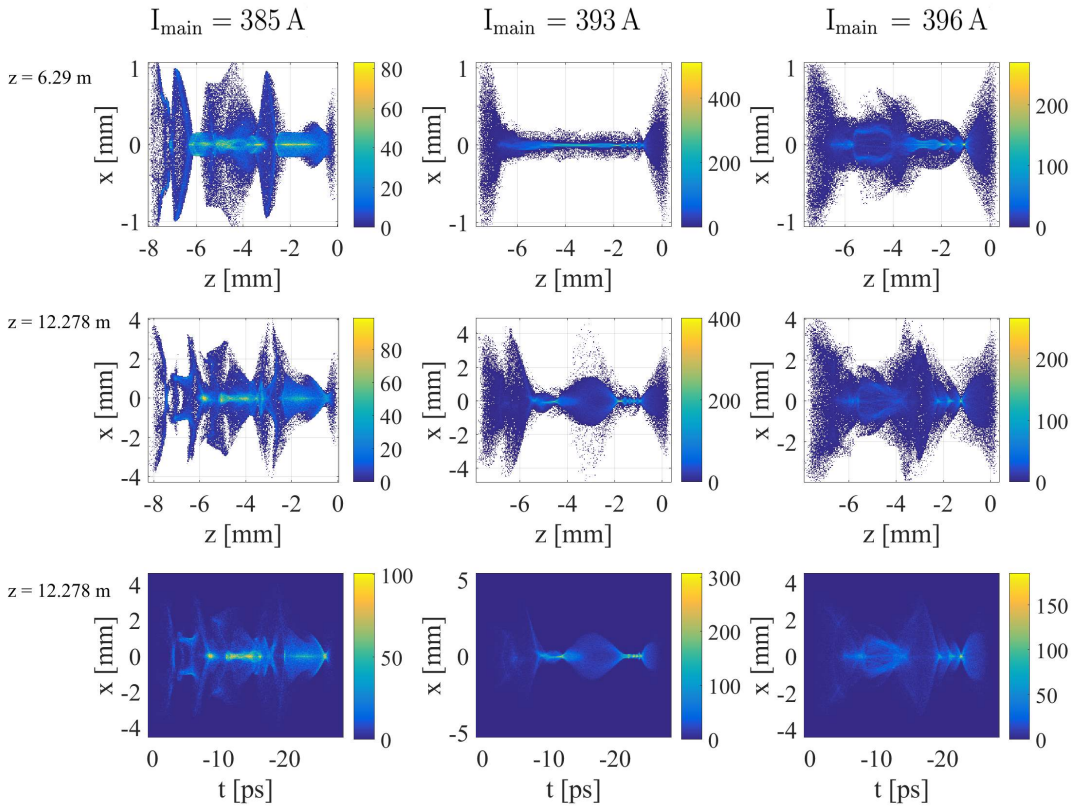

Figure 6.13: Beam profiles with plasma interaction obtained from ASTRA output distributions (upper and middle rows) and from simulated TDS measurements (lower row) at the PST.Scr1 position. The beam head is on the right. Some features (such as defocused and low-intensity halos) of the particle distributions are not seen in the simulated measurement images.

The overall transverse beam profiles in the simulated measurement images are the same as they are seen in the images rendered directly from ASTRA particle distributions; some low-intensity details are not seen and blended into the background. For the $I_{main} = 385\,A$ case, the distribution shows traces of a non-linear beam-plasma interaction driven by the overdense beam head. The 393 A distribution is not self-modulated, but even more tightly focused by plasma, with the maximum charge density $n_b/n_p \approx 17$ in the middle of the beam at the exit of the plasma channel. This overdense region of the beam is blown up on the way to the measurement screen due to space charge forces, while other regions remain well-focused. The $I_{main} = 396\,A$ case shows transverse modulations (caused by the self-modulation instability) along with a ripple structure closer to the beam head. This simulated measurement does not fit well with experimental results (Fig. 5.4). A possible explanation is that the beam profile (especially its head, which is responsible for the wakefield seeding) does not match

exactly to that of a real electron beam, which results in a different transverse profile evolution (compare to Fig. 6.1 (a) and Figs. C.3 and C.4 in Appendix C).

6.2.4.2 Longitudinal phase space at Disp3.Scr1

Figure 6.14 shows the simulation of the TDS measurement for electron beams after propagating 80 mm in $1 \times 10^{14}\,\mathrm{cm}^{-3}$ plasma. Beam distributions at the exit of the plasma channel ($z = 6.29\,\mathrm{m}$) are shown in the first row. The second row shows the corresponding beam distributions upstream of the DISP3.D1 entrance (at $z = 17\,\mathrm{m}$) without the TDS switched on, and the last row shows transverse beam distributions at the Disp3.Scr1 position obtained with the TDS switched on and the dipole transport matrix applied. The second row shows that the energy spread is increased after passing through the TDS (compare to **??**). The beam transverse profile (Fig. 6.13) is "imprinted" in the longitudinal phase space, i.e., beam slices of different radius have different induced momentum spread. That is seen, e.g., for the the ripple structure behind the beam head for the $\mathrm{I_{main}} = 396\,\mathrm{A}$ case: the ripples after passing the plasma are present on the beam transverse profile (Fig. 6.13, right column), but are not seen on the longitudinal phase space distribution at $z = 6.29\,\mathrm{m}$ (Fig. 6.14, top right image). As the electron beam passes through the TDS, the defocused parts of the ripple structure get higher induced longitudinal momentum spread compared to that of the focused parts of the ripple structure and that is seen both in the longitudinal phase space distribution at $z = 17\,\mathrm{m}$ and in the simulated measurement at $z = 17.97\,\mathrm{m}$ (Fig. 6.14, right column, middle and bottom images).

The simulated measurements properly represent the longitudinal phase space distribution, but low-intensity details are not depicted clearly. The phase velocity of the wakefields decreases with respect to the beam velocity with the increase of ζ (see Section 2.7.2); therefore, the electron momentum modulation takes a the non-ideal sinusoidal shape and there are more distortions of that kind closer to the beam tail. The phase slippage is clearly seen for the under- and overfocused cases, while for the $\mathrm{I_{main}} = 393\,\mathrm{A}$ case the phase slippage is almost unobservable and the longitudinal phase space distribution shape remains nearly perfectly sinusoidal – as demonstrated in Section 6.2.2, for that case the self-modulation instability does not develop, and therefore there is no dephasing between the electron beam and the wakefield.

6.3 Conclusions

The simulation studies presented here do not cover all the complexity of the self-modulation instability phenomena. Several aspects and experiment-specific conditions were not included: beam emittance evolution and beam matching into the plasma for emittance preservation (the beam was only focused into the plasma channel instead), effects of plasma density ramps, additional beam scattering by the electron windows. However, the studies have shown a general dependence of the SMI growth on the beam

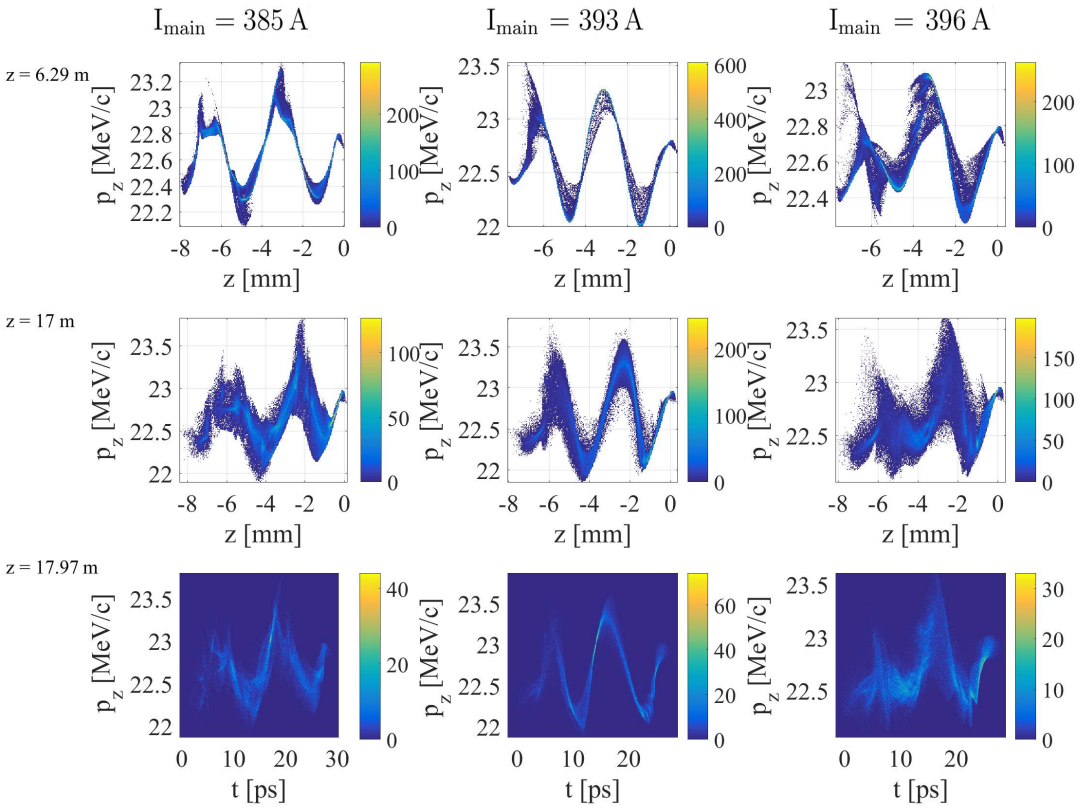

Figure 6.14: Beam profiles obtained from ASTRA output distributions (upper and middle row) and from simulated longitudinal phase space measurements (lower row) at the Disp3.Scr1 position.

charge density profile and demonstrated good agreement between raw simulated data and simulated measurements, and, for overfocused beams, between the simulation and the experiment. The simulated spectrometer measurements demonstrate a measurable phase slippage for the under- and overfocused beam distributions and almost no slippage for a tightly focused beam, while the simulated transverse profile measurement allows to clearly distinguish between different focusing cases (Fig. 6.12). For overfocused beams (homogeneous beam charge density distributions), the HiPACE simulations have shown the SMI development, which agrees with the theory [32] and which is similar to previous simulation studies [57,113]. The measured longitudinal beam profile (homogenous flat-top charge density distribution) combined with the longitudinal phase space measurement (smeared sinusoidal modulations) indicates that the experimentally observed beam-plasma interaction corresponds to the overfocused beam case in the simulations described above and that the electron beam in the experiment is subjected to the SMI.

In the simulations, the highest momentum modulation of about 1 MeV/c was seen

for the tightly focused ($I_{main} = 393\,A$) beam, and the reason for that is the highest seed wakefield amplitude (see Section 6.2.2.1), i.e., not the self-modulation instability. For the overfocused beams ($I_{main} = 395\,A - 398\,A$), the peak-to-peak momentum modulation ranges from 500 keV/c to 900 keV/c, and the lower modulation amplitude corresponds to the higer solenoid current. For the $I_{main} = 398\,A$ case, the xy_{rms} size of the electron beam at the beginning of the plasma channel is 220 µm, while in the experiment it was estimated to be $\gtrsim 160\,\mu m$ (see Section 4.4.3), and the maximum observed peak-to-peak momentum modulation was about 400 keV/c. Several factors besides the xy_{rms} size can be accounted for that discrepancy: different beam head profiles in the experiment and the simulation (compare Fig. 5.4 (a) and Fig. 6.3 (c)), different plasma densities in the experiment and in the simulation, the use an ideal plasma profile in the simulation as opposed to the presence of a density step expected from the ionization laser profile (Fig. 4.21 (b)) in the experiment.

Beam dynamics simulations demonstrate that higher beam charge densities (lower transverse size with the same total charge) would result in higher initial wakefield amplitudes in plasma; the self-modulation instability develops and saturates faster for higher charge densities. However, the growth of the instability is limited by the n_b/n_p ratio, as the instability feedback mechanism works only in the linear regime. Higher plasma density allows to achieve higher wakefield amplitudes and to have more modulation periods along the electron beam, which is important for a more precise characterization of the SMI. The transverse beam size is especially important for higher plasma densities, as it gets larger in the plasma wavelength units c/ω_p with the increase of plasma density, and for certain regimes, the $k_p\sigma_r \ll 1$ condition may not be fulfilled anymore resulting in a current filamentation instability development. The simulations have shown that the hosing instability poses a threat to a successful experiment, especially at higher plasma densities. In experiments, the hosing seed should be avoided by minimization of beam asymmetries and tilts. Since the experiment described in this thesis has been conducted, two additional options became available at PITZ: a pair of gun quadrupole magnets allowing to minimize electron beam asymmetries associated with the RF gun coupler and the main solenoid field aberrations [125], as well as a plasma channel length control, the latter of which would allow to separate the self-modulation and hosing instability growths thanks to uneven seeds of these instabilities and, therefore, different distances in plasma required for their full development. The resolution of the measurements could be a limiting factor for future experiments, especially at higher plasma densities. In the simulations presented here, as well as in the experiment, the beam transport was not fully optimized in order to minimize the TDS-induced energy spread and to increase the dipole spectrometer resolution.

Chapter 7

Conclusions and Outlook

A self-modulation experiment was conducted at PITZ [126], utilizing transverse deflecting cavity and a dipole spectrometer for the measurements. Direct evidences of the self-modulation of a long beam in plasma were observed: time-resolved transverse profiles and longitudinal phase space measurements have shown the characteristic self-modulation signature, as predicted by the theoretical model. The observed coexistence of the transverse and longitudinal fields is a necessary condition for the growth of the self-modulation instability (SMI), and the phase slippage between the electron beam and the wakefield indicates the presence of the instability. The beam radius around the maximal defocusing phase of the wakefield is substantially increased, which would not occur without the SMI. Beam dynamics simulations confirm that the measured profiles correspond to the conditions for the instability development. Together these arguments give strong evidence that the experimental results are caused by the self-modulation instability. The maximum observed beam momentum modulation was 400 keV/c peak-to-peak for a plasma density of $1.3 \times 10^{14}\,\mathrm{cm}^{-3}$.

In the course of preparations of the self-modulation experiment a novel type of plasma source was designed and commissioned – the cross-shaped lithium heat pipe oven plasma cell. The main advantages of the cross-shaped plasma cell are its relative compactness and the possibility to manipulate and control the plasma channel parameters. The maximum achieved plasma density – $1.3 \times 10^{14}\,\mathrm{cm}^{-3}$ – was lower than the goal density of $1 \times 10^{15}\,\mathrm{cm}^{-3}$, but it was sufficient for measurements of longitudinal phase space profile modulations. Experiments with reduced plasma density have demonstrated the increase of the self-modulation period. Adjustments in the setup for follow-up experiments have been performed and include a controllable ionization channel length and improvements of the heat pipe oven heat insulation and optimization of its operation parameters. The latter modifications result in an order-of-magnitude higher lithium vapor density and therefore would allow to reach the initially designed plasma density.

The experiment described in this work is a proof-of-principle experiment. The demonstration of the SMI at PITZ is the first step to a thorough and comprehensive

study of that phenomenon which eventually could lead to a new particle acceleration technology that will render state-of-the-art RF accelerators obsolete. The AWAKE experiment is ongoing at CERN with the goal to demonstrate acceleration of electron beams in plasma wakefields generated by self-modulated proton beam drivers. Since the physics of the self-modulation is the same for any charged particle beams, the experiments at PITZ can provide valuable insights for AWAKE. Experimental conditions at PITZ and AWAKE are compared in Section 5.3. An advantage of PITZ is a higher repetition rate (10 Hz compared to 0.03 Hz at AWAKE [127]) which allows to carry out parameter scans and optimizations of experimental parameters during the experimental run much faster. Apart from further, more precise characterization of the SMI at higher plasma densities, following topics are of interest for future experiments:

- Saturation length of the SMI,
- Influence of plasma inhomogeneities (ramps, modulations),
- Optimization of the beam parameters including matching into plasma for emittance preservation,
- Tolerances and robustness of the SMI and accompanying instabilities.

The improved hardware for the future SMI experiments at PITZ has been prepared and after the conditioning and commissioning of the next RF gun at PITZ (Gun4.5) more SMI experiments will be performed.

Appendices

Appendix A

Plasma cell and lithium handling

A.1 Lithium handling

As mentioned before, lithium is a chemically active alkali metal, and it requires special handling. Following the handling procedures is a prerequisite of the stable heat pipe oven operation. Lithium reacts quickly with air at normal temperature, humidity, and pressure, rendering an oxide layer on its surface. The layer consists of lithium oxide, lithium hydroxide, lithium hydroxide monohydrate, lithium nitride, and lithium carbonate [128]. Lithium is supplied in the form of 99.9 % pure metal rods sealed under protective atmosphere, approximately 15 cm long and 12.7 mm in diameter. Despite the sealing, the rod surface is initially covered with a thin oxide layer. This layer does not melt at the plasma cell operational temperature and prevents the normal distribution of liquid lithium inside the plasma cell, as pure lithium remains contained inside the oxide "shell" even after the plasma cell temperature surpasses the lithium melting point. The oxide layer is soft, and it can be easily removed with a knife in a manner very similar to peeling vegetables skin off. This operation must be carried out under a protective atmosphere, as a new oxidation layer will be formed immediately in the presence of air. Ammonia, a hazardous gas with a pungent smell, is generated during the oxidation process as a by-product of reaction with moisture contained in the air:

$$3\mathrm{Li} + \mathrm{N_2} \rightarrow 2\mathrm{Li_3N}, \tag{A.1}$$

$$\mathrm{Li_3N} + 3\mathrm{H_2O} \rightarrow 3\mathrm{LiOH} + \mathrm{NH_3}. \tag{A.2}$$

All operations, such as taking lithium rods out of the package, cutting and weighing lithium specimens, are conducted in a glovebox under argon atmosphere. It was found that lithium oxidizes quickly after contact with the gloves, and in order to minimize this effect, all moisture should be removed with alcohol from the surface of the gloves. For the mesh studies, the test oven was relatively compact, so the lithium preparations and lithium loading inside the oven took place in the glovebox. However, the plasma cell or the test heat pipe, if put inside the glovebox, leaves no space required for the lithium preparations. We used the following procedure for lithium loading:

1. The plasma cell or the heat pipe are opened (one of the windows on the main tube dismounted).
2. Lithium prepared for loading under argon atmosphere (cleaning and weighting inside the glovebox).
3. Quickly take the freshly cleaned lithium rod out of the glovebox and load it into the plasma cell through the main tube. The lithium rod should be placed approximately to the middle of the oven.
4. Mount the window back, pump and purge plasma cell with argon several times to ensure that no air components are left inside.
5. Set desired argon pressure.
6. Heat up the oven to at least 400 °C to ensure melting of lithium.

It is important to minimize the loading time and to start heating without delays. From our experience, the oxide layer hardens over time, and if heating was started the next day after loading, the lithium would not leave the oxide shell.

A.2 Window exchange

For initial tests in the lab, simple glass windows were mounted on all four plasma cell viewports. This was done to prevent possible contamination of special windows during the preparatory experiments when the optimal buffer gas and temperature parameters were not yet determined. Once lithium is loaded into the plasma cell, all the following window exchange operations must be carried out in the glovebox under argon atmosphere. These operations include, for example, installation of the MgF_2 windows for lithium vapor density measurements using the UV absorption method (Section 4.6). When the cycle of preparation experiments was over, the main tube glass windows were exchanged with thin foil electron windows. It is not possible to use thin foil electron windows in laboratory conditions, as the foils are too delicate to withstand 1 bar pressure difference on two sides. After the installation of the windows, the atmosphere inside the plasma cell was the same as in the glovebox (argon at the pressure slightly higher than 1 bar). The following procedure was used:

1. Initial conditions: plasma cell is filled with lithium and cooled down, normal glass windows are mounted on the main tube.
2. Put the plasma cell into glovebox, exchange glass windows with foil windows under protective atmosphere.
3. While keeping normal pressure inside the plasma cell, transport in to the accelerator tunnel.

4. Mount the plasma cell in the beamline. At this moment the pressure on neighboring beamline sections is also normal.

5. Connect the plasma cell and the neighboring beamline sections to one vacuum pump, so that pressure can be adjusted simultaneously on both sides of the electron windows, and set the nominal operating pressure (1.7 mbar.

6. Disconnect the plasma cell from the vacuum pump, pump out the neighboring beamline sections completely.

The same procedure in the reverse order is employed to dismount the plasma cell from the beamline after the experiment.

A.3 Cleaning the oven and windows

During the preparatory experiments and the first experimental run, the windows became covered with a thin layer of lithium, resulting in a lower laser transmission through the windows. This layer was very thin and it was possible to remove it with water and an optical tissue, after which the laser transmission was completely restored. Cleaning the oven itself is a more complicated task. The plasma cell can contain up to 25 g of lithium and products of lithium oxidation, which are not easily soluble in water. The plasma cell cleaning was conducted by pumping an acidic water solution through the cell. Acid dissolves non-soluble products of oxidation, and a continuous stream of liquid passing through the cell evacuates heat and gaseous products released in chemical reactions between the cleaning solution and lithium and its oxides. The setup for cleaning includes a canister for the washing liquid, an acid-resistant pump, a metal frame for the fixation of the plasma cell in a vertical position, and connecting hoses. The cell was positioned vertically, and the liquid was pumped through the main tube from bottom to top, and the return hose end was submerged in the washing liquid (canister). This was necessary in order to pass gaseous reaction products (mainly ammonia) through the washing liquid and to dissolve them partially in the liquid instead releasing them directly into the air. A citric acid solution was used for the cleaning, and the amount of acid was selected so that, after all lithium has reacted with the solution, the solution remained slightly acidic (pH of about 5) The considerations for that pH value are following: the pH value of the final solution should be close to the neutral value (pH = 7) for safety of handling, but the solution should remain acidic as the pump we had for the cleaning setup is not suited for alkaline solutions. The CurTiPot tool [129] was used to calculate pH values of the solution. Since it was unknown how much lithium in the cell has reacted with nitrogen (i.e., we could not estimate how much ammonia would be released at the moment the contents of the plasma cell reacted with the washing solution) and what fraction of ammonia would be then dissolved in the cleaning solution, the pH calculations were performed for two extreme cases:

1. No ammonia in the solution at all.

2. The maximum possible amount of ammonia is in the solution (whole amount of lithium participates in the reactions described in Eqs. (A.1) and (A.2)).

For example, for the solution containing 8 litres of water, 420 g of citric acid monohydrate, and 25 g of lithium, the pH value lies in between of 4.75 (case 1) and 5.8 (case 2).

Appendix B

Heat pipe calculations

B.1 Introduction

Some estimations regarding heat transportation capabilities of the plasma cell and feasibility of using axial grooves instead of the metal mesh in the setup are presented in this section. The theory of heat pipes is taken mostly from [65, 130]. A simplified 2-d heat pipe model was considered, as shown in Fig. B.1. The calculations were performed for a constant length of the condenser, i.e. without taking into account the gas loading feature (variable length of the condenser according to the heat load). Drawbacks of this simplified approach are discussed in section B.3.

Transportation limitations of heat pipes. The amount of heat transferred through a heat pipe is limited by the following factors:

- Capillary limitation: if the capillary pressure is insufficient to pump the working fluid back to the evaporator.
- Sonic limitation: if the vapor velocity in the heat pipe reaches the velocity limitation, it causes chocked flow.
- Entrainment limitation: if liquid drops are entrained in the vapor flow, the working fluid circulation can decrease.
- Boiling limitation: if the amount of heat at the evaporator is high enough to cause boiling in the wick, it also prevents normal fluid circulation.
- Viscous limitation: under certain conditions, the viscous forces within the vapor may become greater than the pressure gradient caused by heating and the vapor may stagnate.

Capillary limitation

In order to effectively transport the working fluid from condenser to evaporator, the

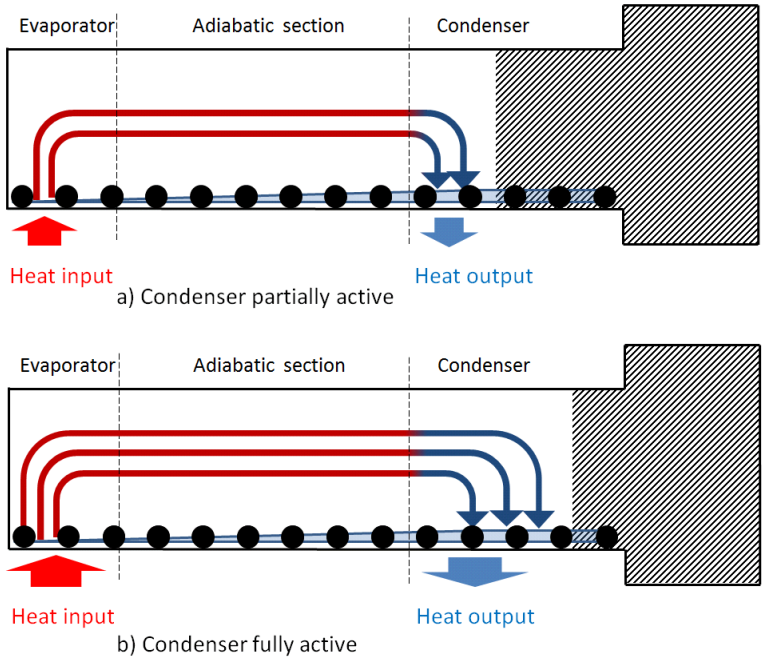

Figure B.1: 2-d model of a gas-loaded heat pipe. Operation principles of gas-loaded heat pipes are described in Section 4.2.

following inequality has to be fulfilled:

$$\Delta P_{c,max} > \Delta P_v + \Delta P_l + \Delta P_{norm} + \Delta P_{axial} \tag{B.1}$$

$\Delta P_{c,max}$ is the maximum capillary pressure difference generated by wick,

$$\Delta P_{c,max} = \frac{2\sigma}{r_{c,e}}, \tag{B.2}$$

where σ is the surface tension of the working fluid, $r_{c,e}$ is the effective capillary radius of the wick. For mesh screens, $r_{c,e} = 1/2N = \frac{w+d}{2}$, where w is wire spacing and d is wire diameter. For rectangular grooves, the effective capillary radius equals the groove width.

Vapor pressure drop

$$\Delta P_v = \frac{C(f_v Re_v)\mu_v}{2r_v^2 A_v \rho_v h_{fg}} L_{eff} q, \tag{B.3}$$

where

f_v = friction factor of vapor,
Re_v = Reynolds number of vapor,

μ_v = absolute viscosity of vapor,
r_v = hydraulic radius of the vapor path,
A_v = cross-sectional area of vapor path,
ρ_v = vapor density,
h_{fg} = latent heat of vaporization,
q = heat transfer rate,
L_{eff} = effective length of the heat pipe, $L_{eff} = L_a + \frac{L_e+L_c}{2}$.

$$Re_v = \frac{4q}{\pi d_v \mu_v h_{fg}}. \tag{B.4}$$

The Mach number of vapor is

$$Ma_v = \frac{q}{\rho_v A_v \mu_v h_{fg} \sqrt{\gamma_v R_v T_v}}, \tag{B.5}$$

where $R_v = R_u/M$ is the gas constant, γ_v is the specific heat ratio, for monoatomic vapors $\gamma_v = 1.67$.

When $Re_v < 2300$ and $Ma_v < 0.2$

$$\begin{aligned} f_v Re_v &= 16, \\ C &= 1. \end{aligned} \tag{B.6}$$

When $Re_v < 2300$ and $Ma_v > 0.2$

$$\begin{aligned} f_v Re_v &= 16, \\ C &= \left[1 + \left(\frac{\gamma_v - 1}{2}\right) Ma_v^2\right]^{-1/2}. \end{aligned} \tag{B.7}$$

When $Re_v > 2300$ and $Ma_v < 0.2$

$$\begin{aligned} f_v Re_v &= 0.038 \left[\frac{2 r_v q}{A_v \mu_v h_{fg}}\right]^{3/4}, \\ C &= 1. \end{aligned} \tag{B.8}$$

When $Re_v > 2300$ and $Ma_v > 0.2$

$$\begin{aligned} f_v Re_v &= 0.038, \\ C &= \left[1 + \left(\frac{\gamma_v - 1}{2}\right) Ma_v^2\right]^{-1/2} \left(\frac{2 r_v q}{A_v \mu_v h_{fg}}\right)^{3/4}. \end{aligned} \tag{B.9}$$

Liquid pressure drop

$$\Delta P_l = \frac{\mu_l}{K A_w \rho_l h_{fg}} L_{eff} q, \tag{B.10}$$

where

μ_l = absolute viscosity of liquid,
K = wick permeability,
A_w = wick cross-sectional area,
ρ_l = liquid density,
q = heat transfer rate,
L_{eff} = effective length of the heat pipe, $L_{eff} = L_a + \frac{L_e+L_c}{2}$.

For rectangular grooves, the permeability is

$$K = \frac{2\varepsilon r_{h,l}^2}{f_l Re_l} \tag{B.11}$$

where ε = wick porosity, $r_{h,l}$ = hydraulic radius, $r_{h,l} = 2\omega\delta/(\omega+2\delta)$, ω = groove width, δ = groove depth, $f_l Re_l = 16$ assuming laminar flow. For wire screens the permeability is

$$K = \frac{d^2\varepsilon^3}{122(1-\varepsilon)^2} \tag{B.12}$$

where $\varepsilon = 1 - (\pi N d/4)$, N = mesh number, d = wire diameter.

Normal hydrostatic pressure drop
If circumferential communication of the working liquid in the wicks is possible, the body force acting perpendicular to the longitudinal axis of the heat pipe occurs:

$$\Delta P_{norm} = \rho_l g d_v \cos\Psi, \tag{B.13}$$

where d_v is the diameter of the vapor portion of the pipe and Ψ is the angle the heat pipe makes with respect to the horizontal.

Axial hydrostatic pressure drop

$$\Delta P_{axial} = \rho_l g L \sin\Psi, \tag{B.14}$$

where L is the overall length of the heat pipe.

Sonic limitation

$$q_{s,max} = A_v \rho_v h_{fg} \sqrt{\frac{\gamma_v R_v T_v}{2(\gamma_v+1)}}. \tag{B.15}$$

Entrainment Limitation

$$q_{s,max} = A_v h_{fg} \sqrt{\frac{\sigma\rho_v}{2r_{h,w}}}, \tag{B.16}$$

where $r_{h,w}$ is the hydraulic radius of the wick, $r_{h,w} = D_h/2 = \frac{2A}{P}$, where A is the cross-flow area and P is the wetted perimeter.

Boiling Limitation

$$q_{b,max} = \frac{4\pi L_e k_{eff} T_v \sigma}{h_{fg} \rho_v \ln(r_i/r_v)} \left(\frac{1}{r_n} - \frac{1}{r_{c,e}} \right), \tag{B.17}$$

where r_n is the nucleation radius, $r_n = 0.254$ μm, k_{eff} is the effective thermal conductivity of the liquid-saturated wick. For mesh screens

$$k_{eff} = \frac{k_l \left[(k_l + k_w) - (1-\varepsilon)(k_l - k_w) \right]}{(k_l + k_w) + (1-\varepsilon)(k_l - k_w)}, \tag{B.18}$$

where k_l is the liquid thermal conductivity, k_w is the wick thermal conductivity. For rectangular grooves

$$k_{eff} = \frac{(w_f k_l k_w \delta) + w k_l (0.185 w_f k_w + \delta k_l)}{(w + w_f)(0.185 w_f k_f + \delta k_l)}, \tag{B.19}$$

where w_f is the groove fin thickness.

Viscous Limitation

$$q_{vis,max} = \frac{A_v r_v^2 h_{fg} \rho_v P_v}{16 \mu_v L_e} \tag{B.20}$$

As an alternative, a relationship between the overall pressure drop in the vapor phase and the absolute pressure in the vapor phase was suggested as

$$\frac{\Delta P_v}{P_v} < 0.1. \tag{B.21}$$

B.2 Calculation

The physical properties of Lithium were taken from [75, 128] and are shown in Table B.1. Table B.2 describes the heat pipe parameters, which were used for the calculations (as our heat pipe is symmetric, the calculations are performed for one half of the existing heat pipe).

Table B.1: Lithium properties at 973 K.

Heat of vaporization	h_{fg}	$2.1182 \times 10^7\,\mathrm{J/kg}$
Liquid density	ρ_l	$468\,\mathrm{kg/m^3}$
Vapor density	ρ_v	$5.1993 \times 10^{-5}\,\mathrm{kg/m^3}$
Surface tension	σ	$0.3173\,\mathrm{N/m}$
Liquid viscosity	μ_l	$2.5566 \times 10^{-4}\,\mathrm{Pa\,s}$
Vapor viscosity	μ_v	$9.5230 \times 10^{-6}\,\mathrm{Pa\,s}$
Saturated pressure	P	$57.8349\,\mathrm{Pa}$
Heat conductivity	k_l	$0.0545\,\mathrm{W/(mK)}$

Table B.2: Heat pipe parameters.

Evaporator length	L_e	$0.115\,\mathrm{m}$
Adiabatic length	L_a	$0.02\,\mathrm{m}$
Condenser length	L_c	$0.02\,\mathrm{m}$
Heat pipe inner diameter	d_i	$0.036\,\mathrm{m}$
Heat conductivity	k	$21\,\mathrm{W/(mK)}$
Mesh wire diameter	d	$0.28\,\mathrm{mm}$
Mesh wire spacing	w	$0.71\,\mathrm{mm}$
Groove width	w	$0.15\,\mathrm{mm}$
Groove depth	h	$0.5\,\mathrm{mm}$
Groove pitch	s	$0.15\,\mathrm{mm}$

Mesh case

Capillary Limit. Since the heat pipe is in a horizontal position, the axial hydrostatic pressure drop will be zero. Equation (B.1) gives

$$\Delta P_{c,max} > \Delta P_v + \Delta P_l + \Delta P_{norm}. \tag{B.22}$$

From Eq. (B.2),

$$\Delta P_{c,max} = \frac{2\sigma}{r_{c,e}} = \frac{4 \times 0.3173\,\mathrm{N/m}}{0.000\,28\,\mathrm{m} + 0.000\,71\,\mathrm{m}} = 1282.1\,\mathrm{Pa}. \tag{B.23}$$

The Reynolds number is

$$Re_v = \frac{4q}{\pi d_v \mu_v h_{fg}} = \\ = \frac{4 \times 450\,\mathrm{J/s}}{\pi \times 3.49 \times 10^{-2}\,\mathrm{m} \times 9.5230 \times 10^{-6}\,\mathrm{Pa\,s} \times 2.1182 \times 10^7\,\mathrm{J/kg}} = 81.4752, \tag{B.24}$$

where

$$d_v = d_{tube} - 4d_w = 0.036\,\mathrm{m} - 4 \times 2.8 \times 10^{-4}\,\mathrm{m} = 3.49 \times 10^{-2}\,\mathrm{m}. \tag{B.25}$$

The Mach number is

$$\begin{aligned} Ma_v &= \frac{q}{\rho_v A_v \mu_v h_{fg} \sqrt{\gamma_v R_v T_v}} = \\ &= \frac{450\,\mathrm{J/s}}{5.1993 \times 10^{-5}\,\mathrm{kg/m^3} \times 9.5553 \times 10^{-4}\,\mathrm{m^2} \times 9.5230 \times 10^{-6}\,\mathrm{Pa\,s} \times 2.1182 \times 10^{7}\,\mathrm{J/kg}} \times \\ &\times \frac{1}{\sqrt{1.67 \times \frac{8.3145\,\mathrm{J/(K\,mol)}}{6.94 \times 10^{-3}\,\mathrm{kg/mol}} \times 973\,\mathrm{K}}} = 0.3554, \end{aligned} \tag{B.26}$$

where $A_v = \frac{\pi d_v^2}{4} = \frac{\pi \times (0.0349\,\mathrm{m})^2}{4} = 9.5553 \times 10^{-4}\,\mathrm{m^2}$. Hence, according to Eq. (B.7),

$$\begin{aligned} f_v Re_v &= 16 \\ C &= \left[1 + \left(\frac{\gamma_v - 1}{2}\right) Ma_v^2\right]^{-1/2} = \\ &= \left[1 + \left(\frac{1.67 - 1}{2}\right) 0.3554^2\right]^{-1/2} = 0.9795. \end{aligned} \tag{B.27}$$

The vapor pressure drop using Eq. (B.3) is

$$\begin{aligned} \Delta P_v &= \frac{C(f_v Re_v)\mu_v}{2 r_v^2 A_v \rho_v h_{fg}} L_{eff} q = \\ &= \frac{0.9795 \times 16 \times 9.523 \times 10^{-6}\,\mathrm{Pa\,s} \times 0.0875\,\mathrm{m} \times 450\,\mathrm{J/s}}{2(1.75 \times 10^{-2}\,\mathrm{m})^2 \times 9.5553 \times 10^{-4}\,\mathrm{m^2} \times 5.1993 \times 10^{-5}\,\mathrm{kg/m^3} \times 2.1182 \times 10^{7}\,\mathrm{J/kg}} = \\ &= 9.1171\,\mathrm{Pa}, \end{aligned} \tag{B.28}$$

where

$$L_{eff} = L_a + \frac{L_e + L_c}{2} = 0.02\,\mathrm{m} + \frac{0.115\,\mathrm{m} + 0.02\,\mathrm{m}}{2} = 0.0875\,\mathrm{m}. \tag{B.29}$$

The liquid pressure drop using Eq. (B.10) is

$$\Delta P_l = \frac{\mu_l}{K A_w \rho_l h_{fg}} L_{eff} q, \tag{B.30}$$

where A_w is the cross-sectional area of the wick, so

$$A_w = \frac{\pi(d_{tube}^2 - d_v^2)}{4} = \frac{\pi((3.6 \times 10^{-2}\,\mathrm{m})^2 - (3.49 \times 10^{-2}\,\mathrm{m})^2}{4} = 6.2349 \times 10^{-5}\,\mathrm{m^2}. \tag{B.31}$$

The wick permeability K is

$$K = \frac{d^2\varepsilon^3}{122(1-\varepsilon)^2} = \frac{(2.8\times10^{-4}\,\mathrm{m})^2\times0.7779^3}{122(1-0.7779)^2} = 6.1294\times10^{-9}\,\mathrm{m}^2, \tag{B.32}$$

where ε is

$$\varepsilon = 1-(\pi Nd/4) = 1-\frac{\pi d}{4(w+d)} = 1-\frac{\pi\times0.28\,\mathrm{mm}}{4(0.28\,\mathrm{mm}+0.71\,\mathrm{mm})} = 0.7779, \tag{B.33}$$

$$\begin{aligned}\Delta P_l &= \frac{2.5566\times10^{-4}\,\mathrm{Pa\,s}\times0.0875\,\mathrm{m}\times450\,\mathrm{J/s}}{6.1294\times10^{-9}\,\mathrm{m}^2\times6.2349\times10^{-5}\,\mathrm{m}^2\times468\,\mathrm{kg/m}^3\times2.1182\times10^7\,\mathrm{J/kg}} = \\ &= 2.6572\,\mathrm{Pa}.\end{aligned} \tag{B.34}$$

The normal hydrostatic pressure drop is

$$\begin{aligned}\Delta P_{norm} &= \rho_l g d_v\cos\Psi = 468\,\mathrm{kg\,m^{-3}}\times9.8196\,\mathrm{m\,s^{-2}}\times3.49\times10^{-2}\,\mathrm{m}\times\cos(0) = \\ &= 160.3855\,\mathrm{Pa}.\end{aligned} \tag{B.35}$$

Now, inserting Eqs. (B.23), (B.28), (B.34) and (B.35) into Eq. (B.22) yields

$$\begin{aligned}1282.1\,\mathrm{Pa} &> 9.1171\,\mathrm{Pa}+2.6572\,\mathrm{Pa}+160.3855\,\mathrm{Pa} \\ 1282.1\,\mathrm{Pa} &> 172.1598\,\mathrm{Pa}.\end{aligned} \tag{B.36}$$

Sonic Limit. Using Eq. (B.15), the sonic limit is

$$\begin{aligned}q_{s,max} &= A_v\rho_v h_{fg}\sqrt{\frac{\gamma_v R_v T_v}{2(\gamma_v+1)}} = \\ &= 9.5553\times10^{-4}\,\mathrm{m}^2\times5.1993\times10^{-5}\,\mathrm{kg/m}^3\times2.1182\times10^7\,\mathrm{J/kg}\times \\ &\times\sqrt{\frac{1.67\times\frac{8.3145\,\mathrm{J/(K\,mol)}}{6.94\times10^{-3}\,\mathrm{kg/mol}}\times973\,\mathrm{K}}{2(1.67+1)}} = 635.2543\,\mathrm{J/s}\end{aligned} \tag{B.37}$$

Entrainment Limit. Using Eq. (B.16), the entrainment limit is

$$\begin{aligned}q_{s,max} &= A_v h_{fg}\sqrt{\frac{\sigma\rho_v}{2r_{h,w}}} = \\ &= 9.5553\times10^{-4}\,\mathrm{m}^2\times2.1182\times10^7\,\mathrm{J/kg}\sqrt{\frac{0.3173\,\mathrm{N/m}\times5.1993\times10^{-5}\,\mathrm{kg/m}^3}{2\times5.5984\times10^{-4}\,\mathrm{m}}} = \\ &= 2457\,\mathrm{J/s},\end{aligned} \tag{B.38}$$

where $r_{h,w}$ is

$$r_{h,w} = \frac{2A}{P} = \frac{2A_w}{\pi(d_i + d_v)} = \frac{2 \times 6.2349 \times 10^{-5}\,\mathrm{m}^2}{\pi(3.6 \times 10^{-2}\,\mathrm{m} + 3.49 \times 10^{-2}\,\mathrm{m}} = 5.5984 \times 10^{-4}\,\mathrm{m}. \tag{B.39}$$

Boiling Limit. Using Eq. (B.17), the boiling limit will be

$$q_{b,max} = \frac{4\pi L_e k_{eff} T_v \sigma}{h_{fg}\rho_v \ln(\frac{r_i}{r_v})}\left(\frac{1}{r_n} - \frac{1}{r_{c,e}}\right), \tag{B.40}$$

where

$$\begin{aligned} k_{eff} &= \frac{k_l\left[(k_l + k_w) - (1-\varepsilon)(k_l - k_w)\right]}{(k_l + k_w) + (1-\varepsilon)(k_l - k_w)} = \\ &= \frac{0.0545 \times \left[(0.0545 + 21) - (1 - 0.7779)(0.0545 - 21)\right]}{(0.0545 + 21) + (1 - 0.7779)(0.0545 - 21)} = 0.0854\,\mathrm{W/(mK)}, \end{aligned} \tag{B.41}$$

$$\begin{aligned} q_{b,max} &= \frac{4\pi \times 0.115\,\mathrm{m} \times 0.0854\,\mathrm{W/(mK)} \times 973\,\mathrm{K} \times 0.3173\,\mathrm{N/m}}{2.1182 \times 10^7\,\mathrm{J/kg} \times 5.1993 \times 10^{-5}\,\mathrm{kg/m^3} \times \ln(\frac{(3.6 \times 10^{-2}\,\mathrm{m})/2}{(3.49 \times 10^{-2}\,\mathrm{m})/2})} \times \\ &\times \left(\frac{1}{0.254\,\mathrm{um}} - \frac{2}{0.28\,\mathrm{mm} + 0.71\,\mathrm{mm}}\right) = 4.387 \times 10^6\,\mathrm{J/s}. \end{aligned} \tag{B.42}$$

Viscous Limit. Using Eq. (B.17), the boiling limit will be

$$\begin{aligned} q_{vis,max} &= \frac{A_v r_v^2 h_{fg}\rho_v P_v}{16\mu_v L_e} = \\ &= \frac{9.56 \times 10^{-4}\,\mathrm{m}^2 \times (3.49 \times 10^{-2}\,\mathrm{m}/2)^2 \times 2.12 \times 10^7\,\mathrm{J/kg} \times 5.12 \times 10^{-5}\,\mathrm{kg/m^3} \times 57.83\,\mathrm{Pa}}{16 \times 9.52 \times 10^{-6}\,\mathrm{Pa\,s} \times 0.115\,\mathrm{m}} = \\ &= 1043\,\mathrm{J/s}. \end{aligned} \tag{B.43}$$

Axial grooves case

Capillary Limit. Since the heat pipe is in a horizontal position, the axial hydrostatic pressure drop will be zero. As the grooves are placed longitudinally, there is no circumferential communication of the working liquid in the wick, hence there is no ΔP_{norm}. Equation (B.1) gives

$$\Delta P_{c,max} > \Delta P_v + \Delta P_l. \tag{B.44}$$

From Eq. (B.2),

$$\Delta P_{c,max} = \frac{2\sigma}{r_{c,e}} = \frac{2 \times 0.3173\,\mathrm{N/m}}{0.000\,15\,\mathrm{m}} = 4230.7\,\mathrm{Pa}. \tag{B.45}$$

The Reynolds number is

$$\begin{aligned} Re_v &= \frac{4q}{\pi d_v \mu_v h_{fg}} = \\ &= \frac{4 \times 450\,\mathrm{J/s}}{\pi \times 3.6 \times 10^{-2}\,\mathrm{m} \times 9.5230 \times 10^{-6}\,\mathrm{Pa\,s} \times 2.1182 \times 10^{7}\,\mathrm{J/kg}} = 78.9004, \end{aligned} \tag{B.46}$$

where

$$d_v = d_{tube} = 0.036\,\mathrm{m}. \tag{B.47}$$

The Mach number is

$$\begin{aligned} Ma_v &= \frac{q}{\rho_v A_v \mu_v h_{fg} \sqrt{\gamma_v R_v T_v}} = \\ &= \frac{450\,\mathrm{J/s}}{5.1993 \times 10^{-5}\,\mathrm{kg/m^3} \times 0.001\,\mathrm{m^2} \times 9.5230 \times 10^{-6}\,\mathrm{Pa\,s} \times 2.1182 \times 10^{7}\,\mathrm{J/kg}} \times \\ &\frac{1}{\sqrt{1.67 \times \frac{8.3145\,\mathrm{J/(K\,mol)}}{6.94 \times 10^{-3}\,\mathrm{kg/mol}} \times 973\,\mathrm{K}}} = 0.3442, \end{aligned} \tag{B.48}$$

where $A_v = \frac{\pi d_v^2}{4} = \frac{\pi \times (0.036\,\mathrm{m})^2}{4} = 0.001\,\mathrm{m}^2$. Hence, according to Eq. (B.7),

$$\begin{aligned} f_v Re_v &= 16 \\ C &= \left[1 + \left(\frac{\gamma_v - 1}{2}\right) Ma_v^2\right]^{-1/2} = \\ &= \left[1 + \left(\frac{1.67 - 1}{2}\right) 0.3442^2\right]^{-1/2} = 0.9807. \end{aligned} \tag{B.49}$$

The vapor pressure drop using Eq. (B.3) is

$$\begin{aligned} \Delta P_v &= \frac{C(f_v Re_v)\mu_v}{2 r_v^2 A_v \rho_v h_{fg}} L_{eff} q = \\ &= \frac{0.9807 \times 16 \times 9.523 \times 10^{-6}\,\mathrm{Pa\,s} \times 0.0875\,\mathrm{m} \times 450\,\mathrm{J/s}}{2(1.8 \times 10^{-2}\,\mathrm{m})^2 \times 0.001\,\mathrm{m^2} \times 5.1993 \times 10^{-5}\,\mathrm{kg/m^3} \times 2.1182 \times 10^{7}\,\mathrm{J/kg}} = \\ &= 8.0998\,\mathrm{Pa}. \end{aligned} \tag{B.50}$$

The liquid pressure drop using Eq. (B.10) is

$$\Delta P_l = \frac{\mu_l}{K A_w \rho_l h_{fg}} L_{eff} q, \tag{B.51}$$

where A_w is the cross-sectional area of the wick, so

$$A_w = \frac{\pi((d_{tube}+h)^2 - d_v^2)}{4} = \frac{\pi((3.6\times10^{-2}\,\mathrm{m} + 5\times10^{-4}\,\mathrm{m})^2 - (3.6\times10^{-2}\,\mathrm{m})^2}{4} = \\ = 2.8471\times10^{-5}\,\mathrm{m}^2. \tag{B.52}$$

The wick permeability K is

$$K = \frac{2\varepsilon r_{h,l}^2}{f_l Re_l} = \frac{2\times0.5\times(0.1304\times10^{-3}\,\mathrm{m})^2}{16} = 1.0628\times10^{-9}\,\mathrm{m}^2, \tag{B.53}$$

where ε is

$$\varepsilon = \frac{w}{w+s} = \frac{0.15\,\mathrm{mm}}{0.15\,\mathrm{mm}+0.15\,\mathrm{mm}} = 0.5, \tag{B.54}$$

and $r_{h,l}$ is

$$r_{h,l} = \frac{2wh}{w+2h} = \frac{2\times0.15\,\mathrm{mm}\times0.5\,\mathrm{mm}}{0.15\,\mathrm{mm}+2\times0.5\,\mathrm{mm}} = 0.1304\,\mathrm{mm} = 0.1304\times10^{-3}\,\mathrm{m}. \tag{B.55}$$

$$\Delta P_l = \frac{2.5566\times10^{-4}\,\mathrm{Pa\,s}\times0.0875\,\mathrm{m}\times450\,\mathrm{J/s}}{1.0628\times10^{-9}\,\mathrm{m}^2\times2.8471\times10^{-5}\,\mathrm{m}^2\times468\,\mathrm{kg/m}^3\times2.1182\times10^7\,\mathrm{J/kg}} = \\ = 33.7976\,\mathrm{Pa}. \tag{B.56}$$

Now, inserting Eqs. (B.45), (B.50) and (B.56) into Eq. (B.22) yields

$$\begin{aligned} 4230.7\,\mathrm{Pa} &> 8.0998\,\mathrm{Pa} + 33.7976\,\mathrm{Pa} \\ 4230.7\,\mathrm{Pa} &> 41.8974\,\mathrm{Pa} \end{aligned} \tag{B.57}$$

Sonic Limit. Using Eq. (B.15), the sonic limit is

$$\begin{aligned} q_{s,max} &= A_v\rho_v h_{fg}\sqrt{\frac{\gamma_v R_v T_v}{2(\gamma_v+1)}} = \\ &= 0.001\,\mathrm{m}^2\times5.1993\times10^{-5}\,\mathrm{kg/m}^3\times2.1182\times10^7\,\mathrm{J/kg}\times \\ &\times\sqrt{\frac{1.67\times\frac{8.3145\,\mathrm{J/(K\,mol)}}{6.94\times10^{-3}\,\mathrm{kg/mol}}\times973\,\mathrm{K}}{2(1.67+1)}} = 676.6564\,\mathrm{J/s} \end{aligned} \tag{B.58}$$

Entrainment Limit. Using Eq. (B.16), the entrainment limit is

$$\begin{aligned} q_{s,max} &= A_v h_{fg}\sqrt{\frac{\sigma\rho_v}{2r_{h,w}}} = \\ &= 0.001\,\mathrm{m}^2\times2.1182\times10^7\,\mathrm{J/kg}\sqrt{\frac{0.3173\,\mathrm{N/m}\times5.1993\times10^{-5}\,\mathrm{kg/m}^3}{2\times0.1304\times10^{-3}\,\mathrm{m}}} = \\ &= 5.4228\times10^3\,\mathrm{J/s}, \end{aligned} \tag{B.59}$$

Table B.3: Heat pipe transport limitations.

Limitation	Mesh screen	Axial grooves
Capillary limitation	$1282.1\,\mathrm{Pa} > 172.1598\,\mathrm{Pa}$	$4230.7\,\mathrm{Pa} > 41.8974\,\mathrm{Pa}$
Sonic Limit	$635.25\,\mathrm{J/s}$	$676.66\,\mathrm{J/s}$
Entrainment Limit	$2457\,\mathrm{J/s}$	$5422\,\mathrm{J/s}$
Boiling Limit	$4.387 \times 10^6\,\mathrm{J/s}$	$5.7295 \times 10^7\,\mathrm{J/s}$
Viscous Limit	$1043\,\mathrm{J/s}$	$1198.7\,\mathrm{J/s}$

Boiling Limit. Using Eq. (B.17), the boiling limit will be

$$q_{b,max} = \frac{4\pi L_e k_{eff} T_v \sigma}{h_{fg}\rho_v \ln(\frac{r_i}{r_v})}\left(\frac{1}{r_n} - \frac{1}{r_{c,e}}\right), \tag{B.60}$$

where

$$\begin{aligned} k_{eff} &= \frac{(w_f k_l k_w \delta) + w k_l (0.185 w_f k_w + \delta k_l)}{(w + w_f)(0.185 w_f k_w + \delta k_l)} = \\ &= \frac{(0.15 \times 0.0545 \times 21 \times 0.5) + 0.15 \times 0.0545(0.185 \times 0.015 \times 21 + 0.5 \times 0.0545)}{(0.15 + 0.15)(0.185 \times 0.15 \times 21 + 0.5 \times 0.0545)} = \\ &= 0.4963\,\mathrm{W/(mK)}. \end{aligned} \tag{B.61}$$

$$\begin{aligned} q_{b,max} &= \frac{4\pi \times 0.115\,\mathrm{m} \times 0.4963\,\mathrm{W/(mK)} \times 973\,\mathrm{K} \times 0.3173\,\mathrm{N/m}}{2.1182 \times 10^7\,\mathrm{J/kg} \times 5.1993 \times 10^{-5}\,\mathrm{kg/m^3} \times \ln(\frac{(0.0365\,\mathrm{m})/2}{(0.036\,\mathrm{m})/2})} \times \\ &\times \left(\frac{1}{0.254\,\mathrm{um}} - \frac{1}{0.15\,\mathrm{mm}}\right) = 5.7295 \times 10^7\,\mathrm{J/s}. \end{aligned} \tag{B.62}$$

Viscous Limit. Using Eq. (B.17), the boiling limit will be

$$\begin{aligned} q_{vis,max} &= \frac{A_v r_v^2 h_{fg} \rho_v P_v}{16 \mu_v L_e} = \\ &= \frac{0.001\,\mathrm{m^2} \times (3.6 \times 10^{-2}\,\mathrm{m}/2)^2 \times 2.12 \times 10^7\,\mathrm{J/kg} \times 5.12 \times 10^{-5}\,\mathrm{kg/m^3} \times 57.83\,\mathrm{Pa}}{16 \times 9.52 \times 10^{-6}\,\mathrm{Pa\,s} \times 0.115\,\mathrm{m}} = \\ &= 1198.7\,\mathrm{J/s}. \end{aligned} \tag{B.63}$$

B.3 Discussion

As shown in the Table B.3, both mesh and grooves cases are feasible. In both cases the heat pipe does not comply with the alternative requirement of the viscous limitation (Eq. (B.21)):

Viscous Limitation	Mesh screen	Axial grooves
$\frac{\Delta P_v}{P_v} < 0.1$	$\frac{\Delta P_v}{P_v} = 0.1576$	$\frac{\Delta P_v}{P_v} = 0.1401$

But in our case, it seems that the transportation of the liquid, not the vapor could be problematic. The only parameter that we can change and that affects directly the liquid transport is the wick permeability K. The permeability depends on the wick geometry, and can vary a lot for the considered parameter range, as shown in Figs. B.2 to B.5. For the mesh case, the wire diameter and wire spacing was estimated with an empiric formula from [78]:

$$d = -8.65 + 12637/N - 84867/N^2, \tag{B.64}$$

where d is expressed in micrometers and N is in inch^{-1}. However, as a rule of thumb, [78] suggests to use mesh with $N > 40$ for alkali metals.

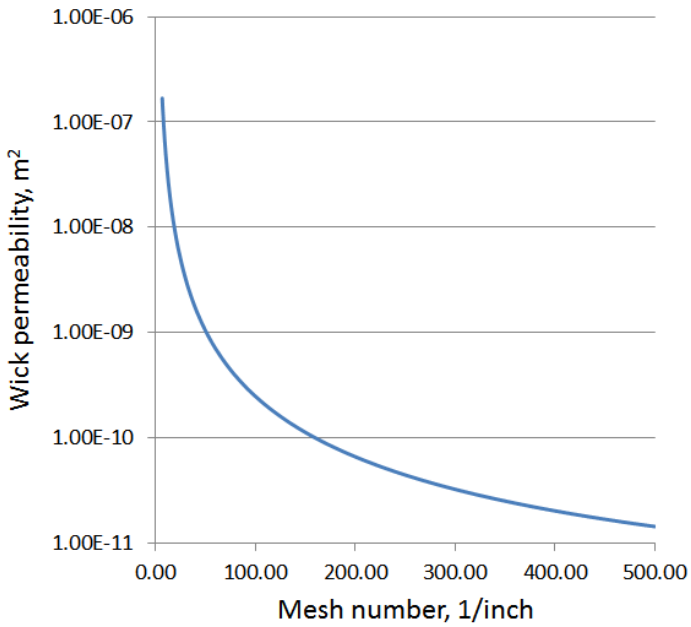

Figure B.2: Mesh permeability vs. mesh number

The simplified 2-d heat pipe model was used for the calculations. However, if we assume that the cross-shaped structure has no effect on the vapor and the liquid flow (i.e., orthogonal flows do not cause additional turbulence), then the requirements for the

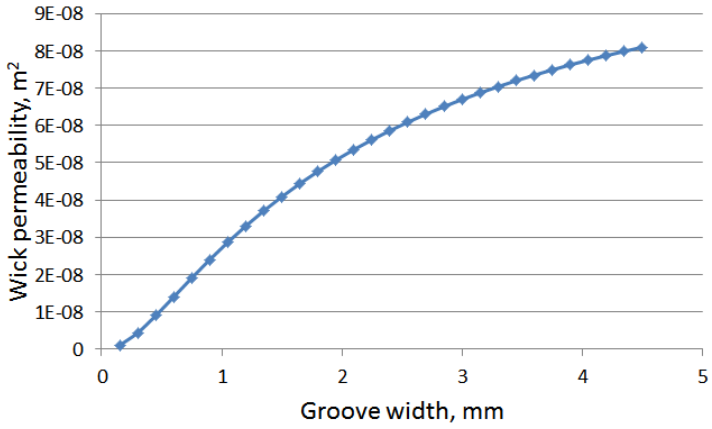

Figure B.3: Axial grooves permeability vs. groove width. $s = 0.15\,\text{mm}, h = 0.5\,\text{mm}$

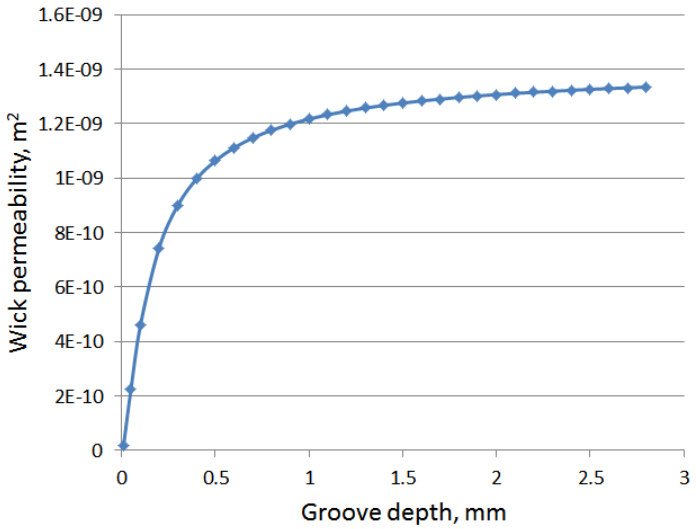

Figure B.4: Axial grooves permeability vs. groove depth. $s = 0.15\,\text{mm}, w = 0.15\,\text{mm}$

heat pipe become more relaxed: the heat input is split in four directions, so every piece of the heat pipe receives less than 450 J/s heat, for the side arms L_{eff} is shorter and A_v and A_w are greater, so the required ΔP_v and ΔP_l are lower. If the gas buffer expands and therefore the vapor column length decreases, it also facilitates the circulation of the working fluid and vapor. With the funnel-shaped plasma cell, we have an additional component for the capillary limit in the side arms, the axial hydrostatic pressure drop,

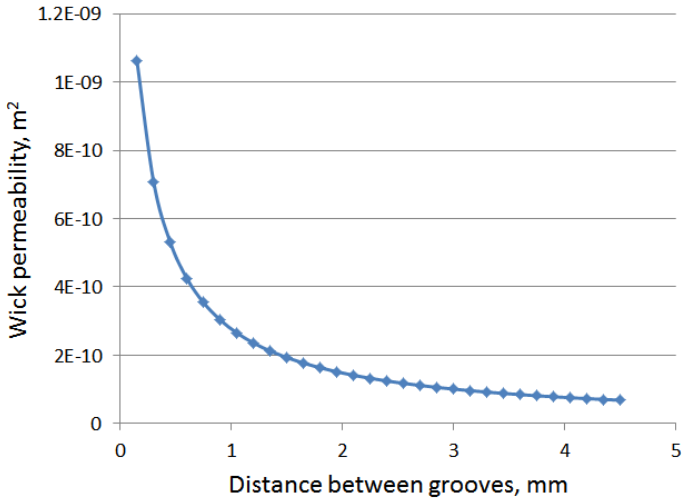

Figure B.5: Axial grooves permeability vs. distance between grooves. $w = 0.15\,\mathrm{mm}, h = 0.5\,\mathrm{mm}$

however, it is not high enough to prevent the normal circulation of liquid:

$$\Delta P_{axial} = \rho_l g L \sin\Psi = 468\,\mathrm{kg/m^3} \times 9.8196\,\mathrm{ms^{-2}} \times 0.108\,\mathrm{m} \times \frac{0.033\,\mathrm{m}}{0.108\,\mathrm{m}} = 150.7\,\mathrm{Pa}. \tag{B.65}$$

The heat pipe calculations confirm that the groove-based heat pipe will perform well in the desired parameter range. As a result, the test heat pipe setup and the second generation of the PITZ plasma cell were built using the axial groove design (see Sections 4.2 and 4.3).

Appendix C

Additional measurements and beam dynamics simulations results

This appendix shows several illustrations not included in Chapters 5 and 6 of the main text.

Figures C.1 and C.2 demonstrate the time-resolved transverse profiles of the electron beam measured at PST.Scr1 for various plasma densities. It is seen that the modulation period follows the plasma density. For more details refer to Sections 5.2.2 and 5.2.5.

Figures C.3 and C.4 show longitudinal electron beam profiles at the beginning of the plasma channel simulated with the ASTRA code for the solenoid current range of 385 A – 398 A. The beam distributions can be grouped into three cases: underfocused beams (I_{main} =385 to 392 A) with two focused regions along the beam, a tightly focused beam (I_{main} = 393 A) with one focused region in the middle, and overfocused beams (I_{main} = 395 to 398 A) with a nearly homogenous charge density distribution along the beam. Results of the HiPACE simulations for I_{main} =385 A, 394 A and 396 A are described in Sections 6.2.2.1 and 6.2.2.2, while Figs. C.5 to C.8 show the HiPACE simulation results obtained for the whole range of the main solenoid current.

Figure C.9 demonstrates the development of the hosing instability in $1 \times 10^{14}\,\mathrm{cm}^{-3}$ and $1 \times 10^{15}\,\mathrm{cm}^{-3}$ plasmas simulated with HiPACE. The I_{main} = 393 A case is shown, as for the the lower density case the self-modulation instability does not develop for that distribution and hosing can be seen more clearly. For $1 \times 10^{14}\,\mathrm{cm}^{-3}$ plasma density hosing develops only on a large propagation distance, while for $1 \times 10^{15}\,\mathrm{cm}^{-3}$ plasma density the hosing and self-modulation instabilities develop on the length of the PITZ plasma cell. For more details refer to Section 6.2.2.3.

Figure C.10 shows the development of the filamentation instability simulated with HiPACE. It is only observed for the I_{main} = 398 A beam in $1 \times 10^{15}\,\mathrm{cm}^{-3}$ plasma. For that case, the beam transverse size $k_p\sigma_r$ = 1.32 and the plasma return current flows through the electron beam, resulting in filamentation.

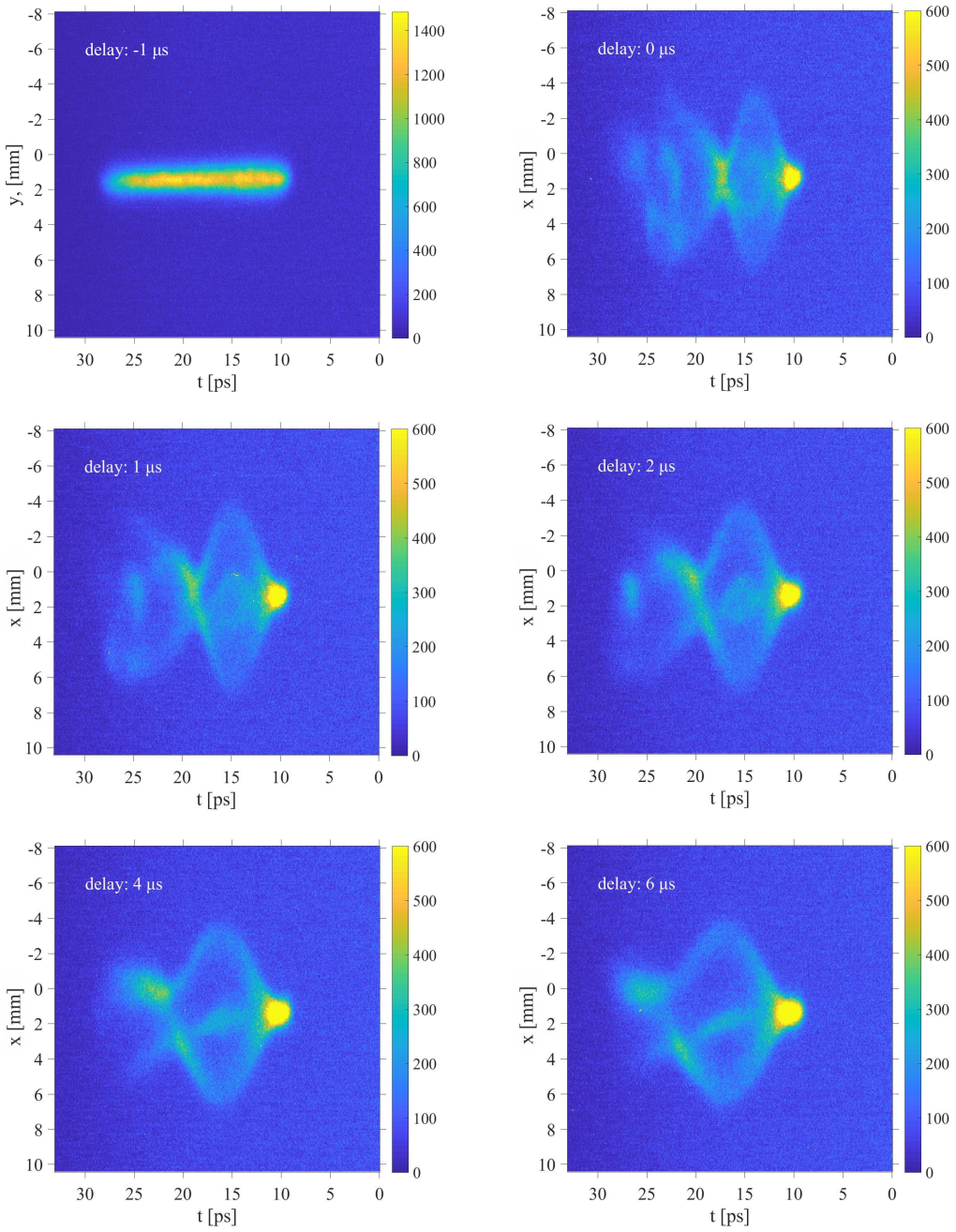

Figure C.1: Time-resolved electron beam profile measured at PST.Scr1 for different ionization laser delays. Delay time of $-1\,\mu s$ corresponds to the case without plasma. The modulation period follows the plasma density. The beam head is on the right. Images are oversaturated, so that low-intensity details of the self-modulated beam can be observed. For more details refer to Chapter 5.

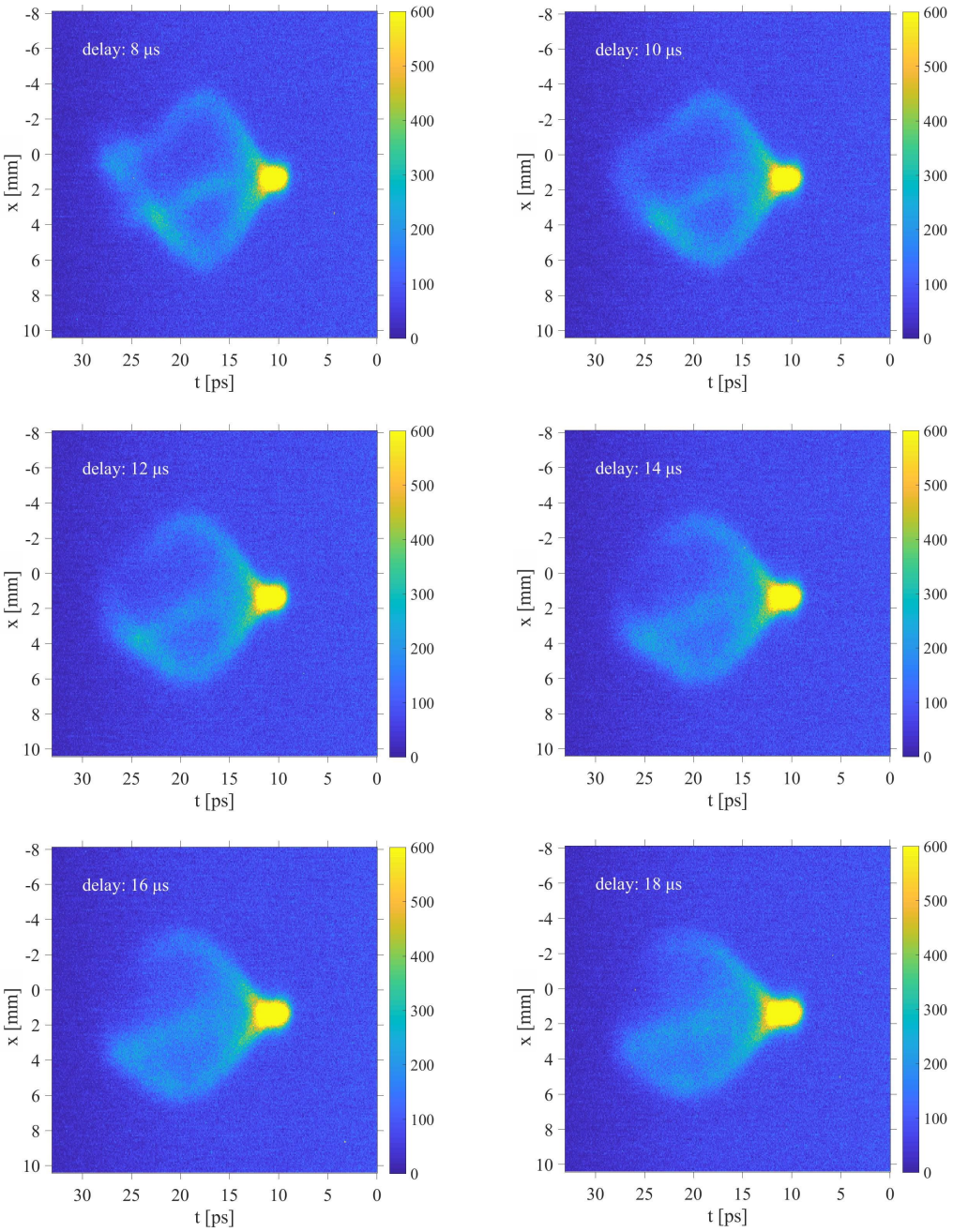

Figure C.2: Time-resolved electron beam profile measured at PST.Scr1 for different ionization laser delays. Delay time of $-1\,\mu s$ corresponds to the case without plasma. The modulation period follows the plasma density. The beam head is on the right. Images are oversaturated, so that low-intensity details of the self-modulated beam can be observed. For more details refer to Chapter 5.

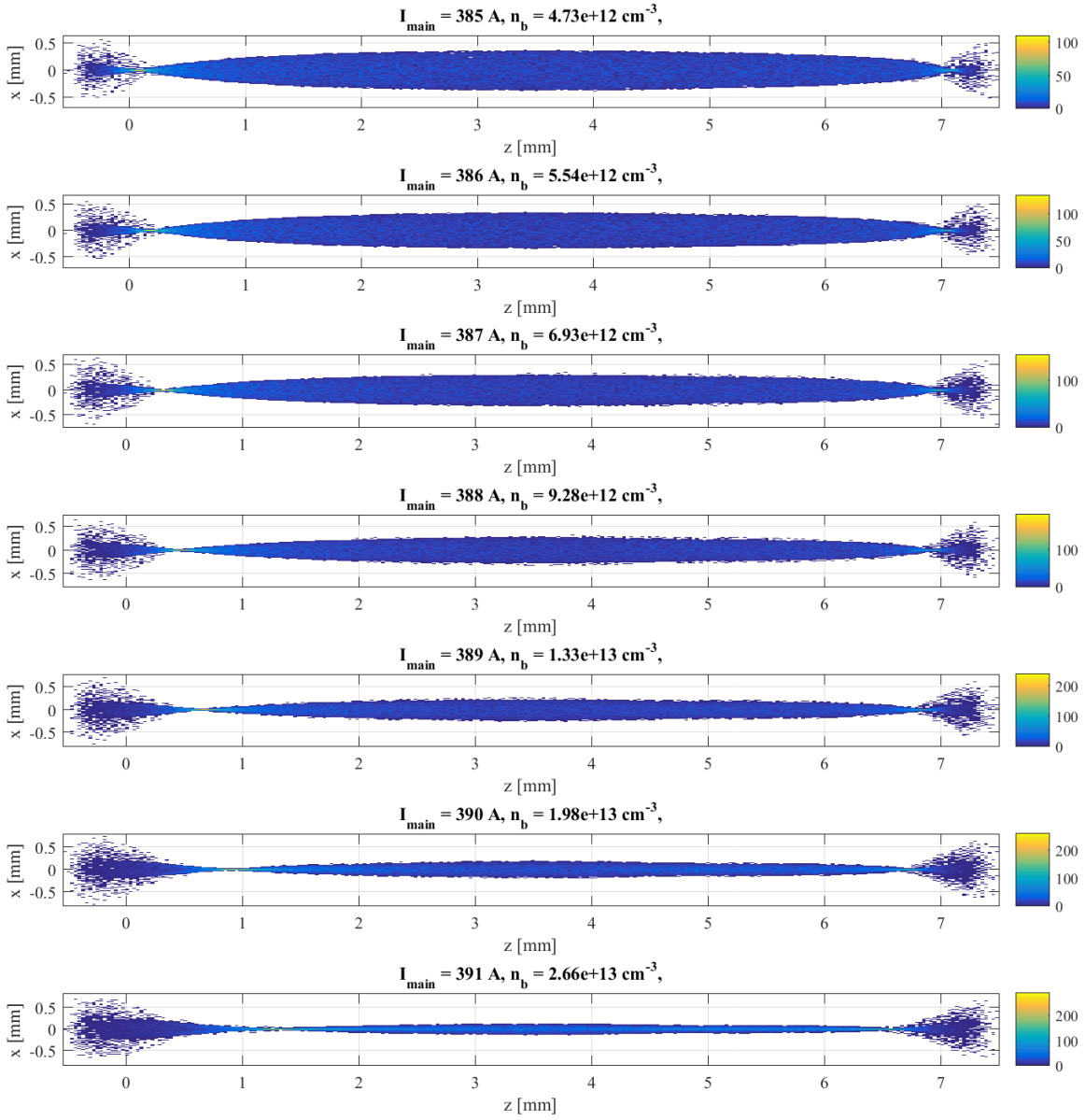

Figure C.3: Longitudinal electron beam profiles at the beginning of the plasma channel for different main solenoid currents, simulated with ASTRA. The beam head is on the right. For the solenoid current range of 385 A – 392 A, the electron beam is focused in its head and tail, while in the middle part it has lower charge density. See more profiles in the next figure.

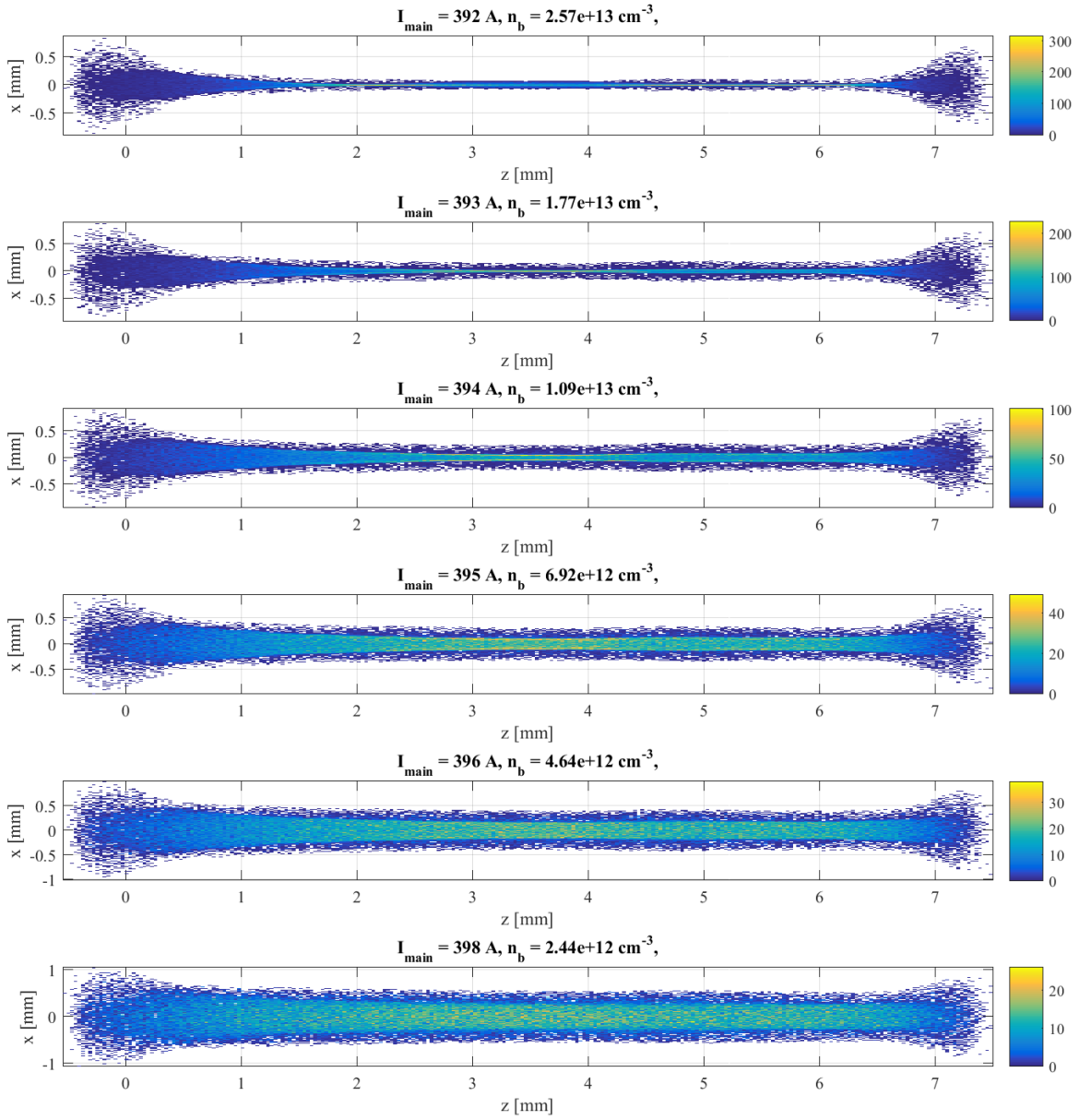

Figure C.4: Longitudinal electron beam profiles at the beginning of the plasma channel for different main solenoid currents, simulated with ASTRA. The beam head is on the right. For the solenoid current of $I_{main} = 393\,A$, the electron beam is focused in the middle. For higher solenoid currents, the electron beam is overfocused and has nearly homogenous charge density distribution.

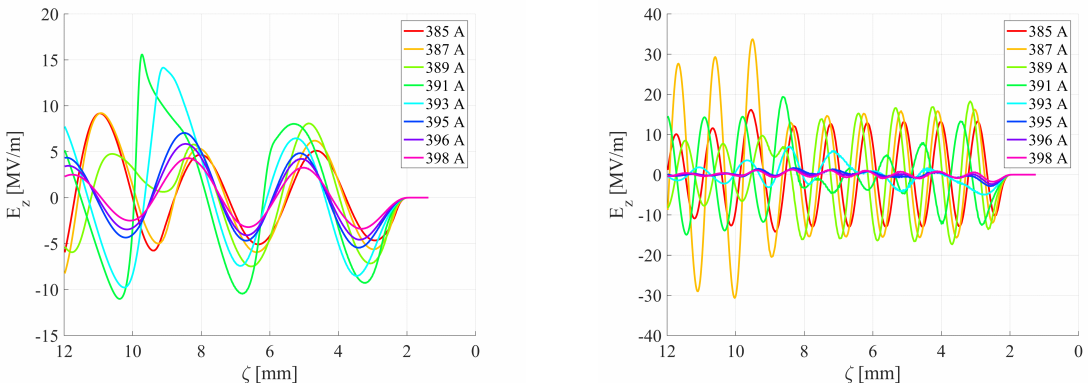

(a) Plasma density is $1 \times 10^{14}\,\mathrm{cm}^{-3}$

(b) Plasma density is $1 \times 10^{15}\,\mathrm{cm}^{-3}$

Figure C.5: Initial longitudinal accelerating electric fields E_z for different beam focusing. Simulated with HiPACE. The beam head is on the right. The beam starts at $\zeta \approx 2\,\mathrm{mm}$.

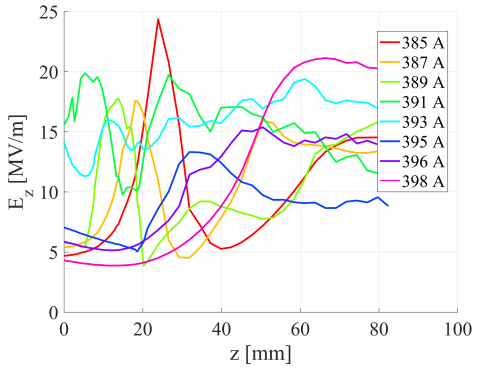

(a) Plasma density is $1 \times 10^{14}\,\mathrm{cm}^{-3}$

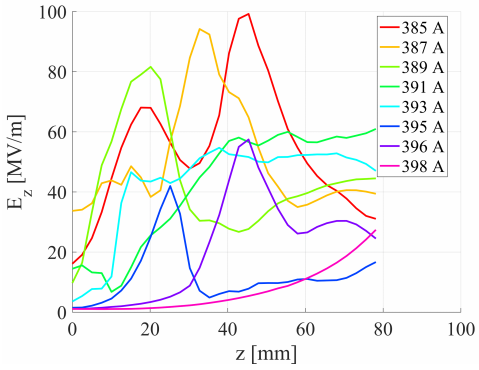

(b) Plasma density is $1 \times 10^{15}\,\mathrm{cm}^{-3}$

Figure C.6: Evolution of the first maximum of the longitudinal electric field E_z behind the electron beam as a function of the distance propagated in plasma.

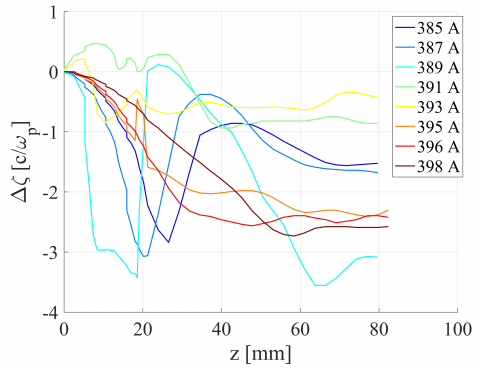

(a) Plasma density is $1 \times 10^{14}\,\mathrm{cm}^{-3}$

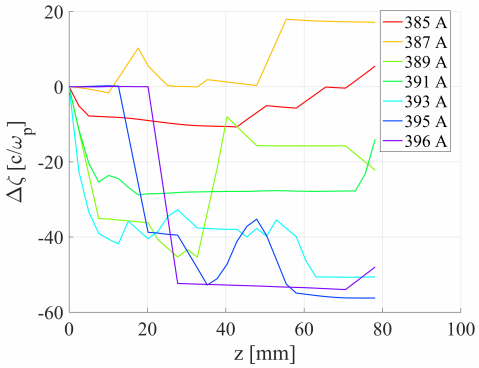

(b) Plasma density is $1 \times 10^{15}\,\mathrm{cm}^{-3}$

Figure C.7: Dephasing of the first maximum of the longitudinal electric field E_z behind the electron beam as a function of the distance propagated in plasma.

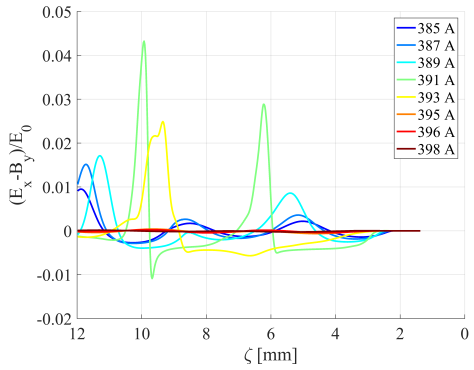

(a) Plasma density is $1 \times 10^{14}\,\mathrm{cm}^{-3}$

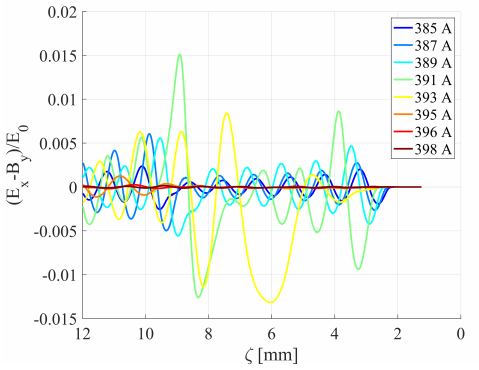

(b) Plasma density is $1 \times 10^{15}\,\mathrm{cm}^{-3}$

Figure C.8: Initial transverse focusing field profiles for three different focusing cases. The beam starts at $\zeta \approx 2\,\mathrm{mm}$

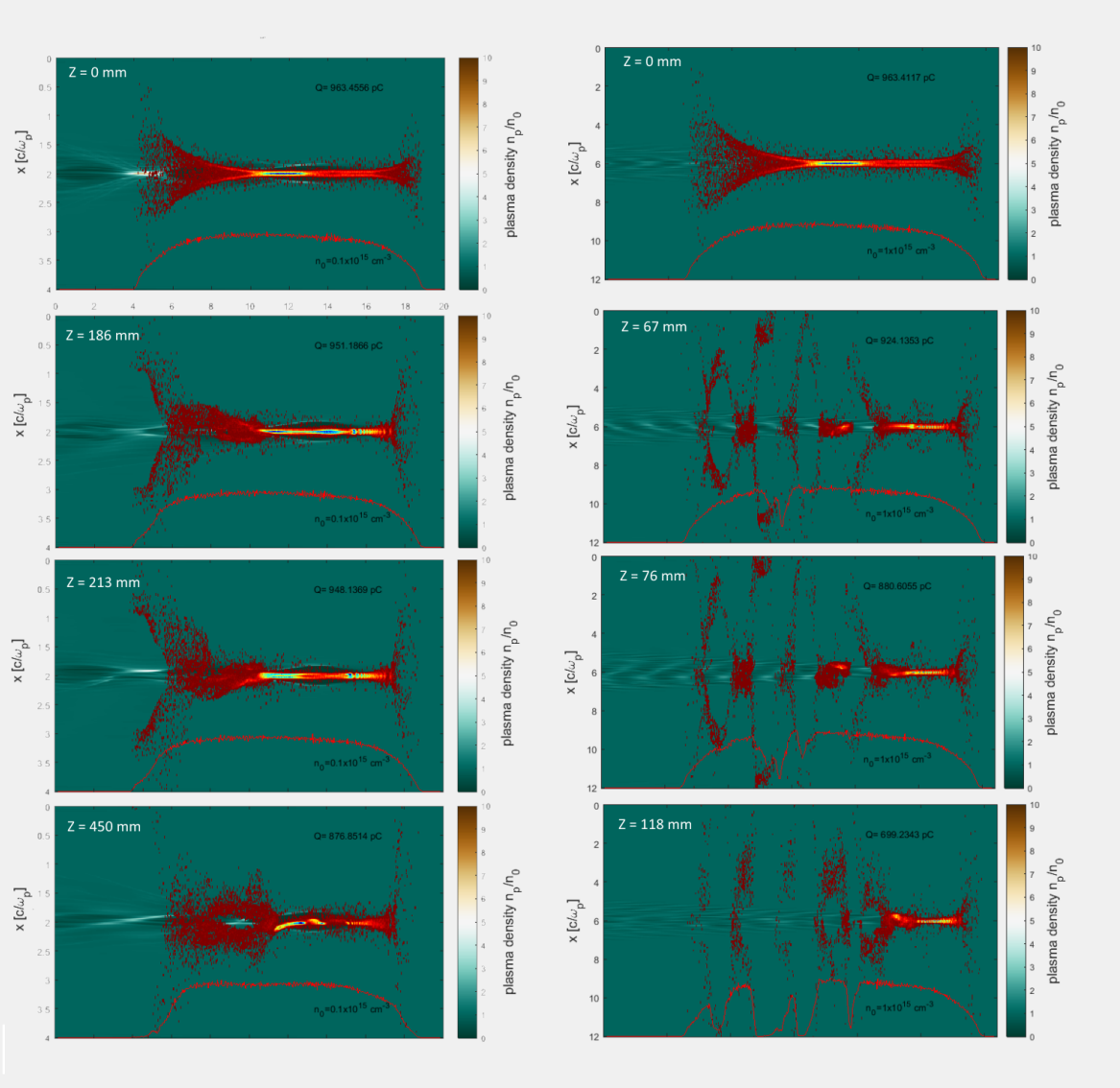

Figure C.9: Development of the hosing instability for the tightly focused beam (I_{main} = 393 A) over long propagation distance in plasma. On the left side plasma density is $1 \times 10^{14}\,\mathrm{cm}^{-3}$ and the SMI development is suppressed, while a noticeable hosing develops over the distances substantially larger than achievable in the experiment: approximately one half of the beam is affected by the hosing instability after propagating 45 cm in plasma. For $1 \times 10^{15}\,\mathrm{cm}^{-3}$ plasma density (on the right side) the self-modulation and hosing instabilities develop in parallel, and the beam is half destroyed due to hosing already after propagating 76 mm in plasma.

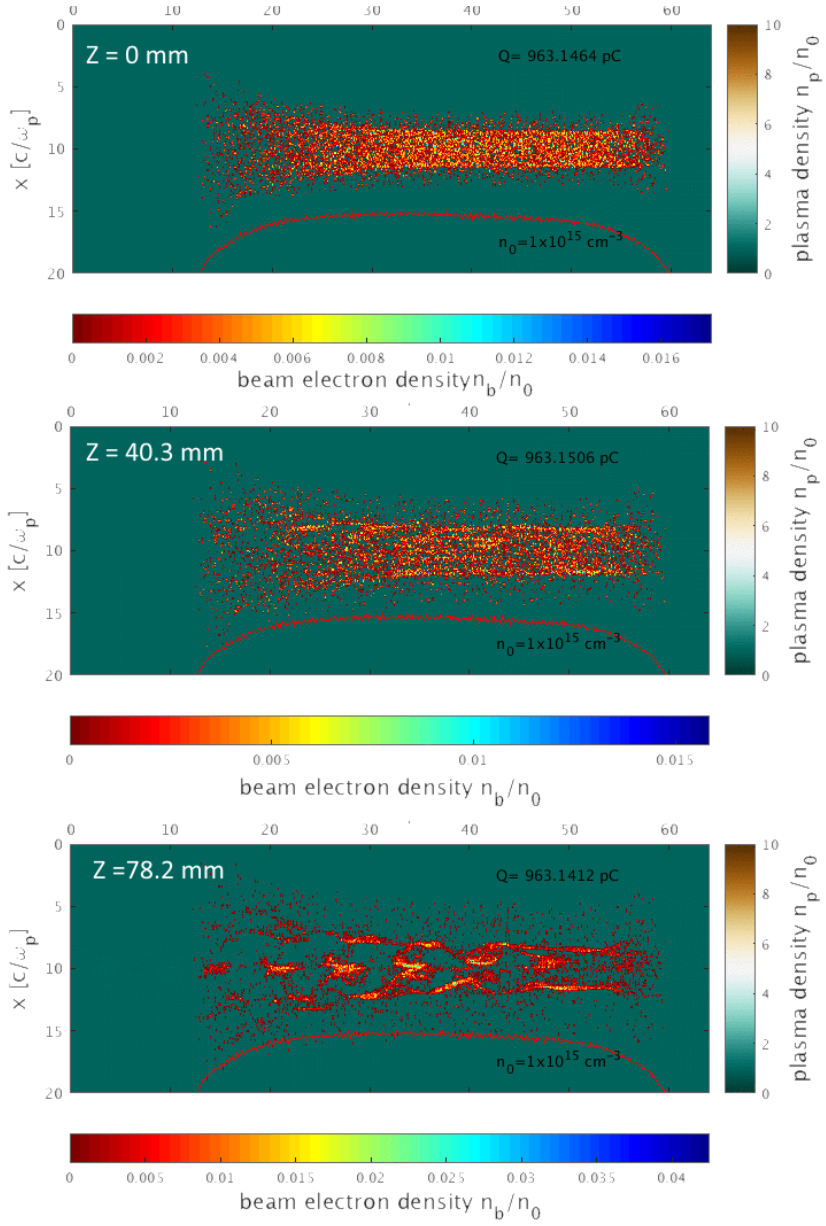

Figure C.10: Development of the filamentation instability for the overfocussed beam ($I_{main} = 398\,A$) in $1 \times 10^{15}\,cm^{-3}$ plasma. The $k_p\sigma_z \ll 1$ condition is not fulfilled and the beam is broken transversely by the plasma return current. For lower solenoid currents, the plasma focusing takes over and the self-modulation instability starts to develop (but only after a considerable distance is traveled in plasma, as the initial seed for the instability is low).

Bibliography

[1] C. Adolphsen *et al.*, "The International Linear Collider Technical Design Report – Volume 3.I: Accelerator R&D in the Technical Design Phase," *ArXiv e-prints*, June 2013.

[2] CLIC collaboration *et al.*, "A multi-TeV linear collider based on CLIC technology: CLIC conceptual design report," Volume 1. CERN, Geneva, Tech. Rep., 2012.

[3] R. Assmann *et al.*, "Calibration of centre-of-mass energies at LEP 2 for a precise measurement of the W boson mass," *Eur. Phys. J. C*, vol. 39, pp. 253–292, 2005.

[4] T. Tajima and J. Dawson, "Laser electron accelerator," *Physical Review Letters*, vol. 43, no. 4, p. 267, 1979.

[5] P. Chen, J. Dawson, R. W. Huff, and T. Katsouleas, "Acceleration of electrons by the interaction of a bunched electron beam with a plasma," *Physical Review Letters*, vol. 54, no. 7, p. 693, 1985.

[6] W. P. Leemans, *et al.*, "GeV electron beams from a centimetre-scale accelerator," *Nature physics*, vol. 2, no. 10, p. 696, 2006.

[7] N. A. Hafz, *et al.*, "Stable generation of GeV-class electron beams from self-guided laser–plasma channels," *Nature Photonics*, vol. 2, no. 9, pp. 571–577, 2008.

[8] X. Wang, *et al.*, "Quasi-monoenergetic laser-plasma acceleration of electrons to 2 GeV," *Nature communications*, vol. 4, p. 1988, 2013.

[9] W. Leemans, *et al.*, "Multi-GeV electron beams from capillary-discharge-guided subpetawatt laser pulses in the self-trapping regime," *Physical Review Letters*, vol. 113, no. 24, p. 245002, 2014.

[10] E. Adli, *et al.*, "A beam driven plasma-wakefield linear collider: from Higgs factory to multi-TeV," *arXiv preprint arXiv:1308.1145*, 2013.

[11] M. Roth and M. Schollmeier, "Ion acceleration – target normal sheath acceleration," in *Proceedings, CAS – CERN Accelerator School: Plasma Wake Acceleration: Geneva, Switzerland, November 23-29, 2014*. Geneva: CERN, 2016, pp. 231–270.

[12] P. Muggli, "Beam-driven, plasma-based particle accelerators," in *Proceedings, CAS - CERN Accelerator School: Plasma Wake Acceleration: Geneva, Switzerland, November 23-29, 2014*. Geneva: CERN, 2016, pp. 119–142.

[13] A. Seryi, *Unifying Physics of Accelerators, Lasers and Plasma*. CRC Press, 2015.

[14] C. Schroeder, C. Benedetti, E. Esarey, F. Grüner, and W. Leemans, "Coherent seeding of self-modulated plasma wakefield accelerators," *Physics of Plasmas*, vol. 20, no. 5, p. 056704, 2013.

[15] V. Malka, "Plasma wake accelerators: introduction and historical overview," in *Proceedings, CAS - CERN Accelerator School: Plasma Wake Acceleration: Geneva, Switzerland, November 23-29, 2014*. Geneva: CERN, 2016, pp. 1–28.

[16] W. Lu, *et al.*, "Generating multi-GeV electron bunches using single stage laser wakefield acceleration in a 3d nonlinear regime," *Physical Review Special Topics-Accelerators and Beams*, vol. 10, no. 6, p. 061301, 2007.

[17] T. Katsouleas, "Physical mechanisms in the plasma wake-field accelerator," *Physical Review A*, vol. 33, no. 3, p. 2056, 1986.

[18] E. Esarey, C. Schroeder, and W. Leemans, "Physics of laser-driven plasma-based electron accelerators," *Reviews of Modern Physics*, vol. 81, no. 3, p. 1229, 2009.

[19] S. Hillenbrand, "Study of plasma-based acceleration for high energy physics and other applications," Ph.D. dissertation, Karlsruhe U., 2013.

[20] S. Steinke *et al.*, "Multistage coupling of independent laser-plasma accelerators," *Nature*, vol. 530, no. 7589, pp. 190–193, 2016.

[21] C. Lindstrm, E. Adli, E. Marn, J. Pfingstner, and D. Schulte, "Transverse Tolerances of a Multi-Stage Plasma Wakefield Accelerator," in *Proc. of International Particle Accelerator Conference (IPAC'16), Busan, Korea, May 8-13, 2016*, June 2016, pp. 2561–2564.

[22] A. Caldwell, K. Lotov, A. Pukhov, and F. Simon, "Proton-driven plasma-wakefield acceleration," *Nature Physics*, vol. 5, no. 5, pp. 363–367, 2009.

[23] N. Kumar, A. Pukhov, and K. Lotov, "Self-modulation instability of a long proton bunch in plasmas," *Physical Review Letters*, vol. 104, no. 25, p. 255003, 2010.

[24] E. Gschwendtner, *et al.*, "AWAKE, the advanced proton driven plasma wakefield acceleration experiment at CERN," *Nuclear Instruments and Methods in Physics Research Section A: Accelerators, Spectrometers, Detectors and Associated Equipment*, vol. 829, pp. 76–82, 2016.

[25] E. Adli, "Towards AWAKE Applications: Electron Beam Acceleration in a Proton Driven Plasma Wake," in *Proc. of International Particle Accelerator Conference (IPAC'16), Busan, Korea*, 2016.

[26] Y. Fang, *et al.*, "Seeding of self-modulation instability of a long electron bunch in a plasma," *Physical Review Letters*, vol. 112, no. 4, p. 045001, 2014.

[27] E. Adli, *et al.*, "Progress of plasma wakefield self-modulation experiments at FACET," *Nuclear Instruments and Methods in Physics Research Section A: Accelerators, Spectrometers, Detectors and Associated Equipment*, vol. 829, pp. 334–338, 2016.

[28] F. F. Chen, *Plasma Physics and Controlled Fusion*, 2nd ed. Springer, New York, 2006.

[29] T. J. M. Boyd and J. J. Sanderson, *The Physics of Plasmas*. Cambridge University Press, 2003.

[30] R. J. Goldston and P. H. Rutherford, *Introduction to Plasma Physics*. CRC Press, 1995.

[31] P. Gibbon, "Introduction to plasma physics," in *Proceedings, CAS - CERN Accelerator School: Plasma Wake Acceleration: Geneva, Switzerland, November 23-29, 2014*, CERN. Geneva: CERN, 2016, pp. 51–65.

[32] C. Schroeder, C. Benedetti, E. Esarey, F. Grüner, and W. Leemans, "Growth and phase velocity of self-modulated beam-driven plasma waves," *Physical Review Letters*, vol. 107, no. 14, p. 145002, 2011.

[33] P. Muggli, *et al.*, "Three regimes of relativistic beam-plasma interaction," in *AIP Conference Proceedings*, vol. 1507, no. 1. AIP, 2012, pp. 594–599.

[34] E. J. Jaeschke, S. Khan, J. R. Schneider, J. Hastings, *et al.*, *Synchrotron Light Sources and Free-Electron Lasers*. Springer Reference, 2016.

[35] A. Caldwell and K. Lotov, "Plasma wakefield acceleration with a modulated proton bunch," *Physics of Plasmas*, vol. 18, no. 10, p. 103101, 2011.

[36] A. Caldwell *et al.*, "Path to AWAKE: Evolution of the concept," *Nuclear Instruments and Methods in Physics Research Section A: Accelerators, Spectrometers, Detectors and Associated Equipment*, vol. 829, pp. 3–16, 2016.

[37] K. Lotov, "Excitation of two-dimensional plasma wakefields by trains of equidistant particle bunches," *Physics of Plasmas*, vol. 20, no. 8, p. 083119, 2013.

[38] C. Schroeder, C. Benedetti, E. Esarey, F. Grüner, and W. Leemans, "Coupled beam hose and self-modulation instabilities in overdense plasma," *Physical Review E*, vol. 86, no. 2, p. 026402, 2012.

[39] A. Pukhov, *et al.*, "Phase velocity and particle injection in a self-modulated proton-driven plasma wakefield accelerator," *Physical Review Letters*, vol. 107, no. 14, p. 145003, 2011.

[40] C. Schroeder, C. Benedetti, E. Esarey, F. Grüner, and W. Leemans, "Particle beam self-modulation instability in tapered and inhomogeneous plasma," *Physics of Plasmas*, vol. 19, no. 1, p. 010703, 2012.

[41] K. Lotov, A. Pukhov, and A. Caldwell, "Effect of plasma inhomogeneity on plasma wakefield acceleration driven by long bunches," *Physics of Plasmas*, vol. 20, no. 1, p. 013102, 2013.

[42] K. Lotov, "Physics of beam self-modulation in plasma wakefield accelerators," *Physics of Plasmas*, vol. 22, no. 10, p. 103110, 2015.

[43] M. Ferrario, K. Flöttmann, B. Grigoryan, T. Limberg, and P. Piot, "Conceptual design of the XFEL photoinjector," *TESLA FEL Report*, 2001.

[44] G. Vashchenko, "Transverse phase space studies with the new CDS booster cavity at PITZ," Ph.D. dissertation, University of Hamburg, 2013.

[45] I. Isaev, "Stability and performance studies of the PITZ photoelectron gun," Ph.D. dissertation, University of Hamburg, 2017.

[46] I. Will and G. Klemz, "Generation of flat-top picosecond pulses by coherent pulse stacking in a multicrystal birefringent filter," *Optics express*, vol. 16, no. 19, pp. 14 922–14 937, 2008.

[47] M. Hänel, "Experimental investigations on the influence of the photocathode laser pulse parameters on the electron bunch quality in an RF-photoelectron source," Ph.D. dissertation, University of Hamburg, 2010.

[48] *JAI: RMC-1405GE / TMC-1405GE CCD camera,* www.jai.com/en/products/tmc-1405ge.

[49] Y. Ivanisenko and M. Hänel, "Latest developments in PITZ cathode laser diagnostics," PITZ Collaboration Meeting, Zeuthen, June 2008.

[50] Y. Ivanisenko, "Photo injector cathode laser beam intensity and position monitoring system," Master's thesis, Karazin Kharkiv National University, 2007.

[51] D. Malyutin, "Time resolved transverse and longitudinal phase space measurements at the high brightness photo injector PITZ," Ph.D. dissertation, University of Hamburg, 2014.

[52] V. Paramonov, *et al.*, "The PITZ CDS booster cavity RF tuning and start of conditioning," in *Proceedings of LINAC10, Tsukuba, Japan*, 2010.

[53] L. Kravchuk, *et al.*, "Layout of the PITZ transverse deflecting system for longitudinal phase space and slice emittance measurements," in *Proceedings of LINAC10, Tsukuba, Japan*, 2010.

[54] H. Huck, *et al.*, "Progress on the PITZ TDS," in *Proceedings of International Beam Instrumentation Conference, Barcelona, Spain*, 2016.

[55] P. Emma, J. Frisch, and P. Krejcik, "A Transverse RF deflecting structure for bunch length and phase space diagnostics," *LCLS Technical Note*, vol. 12, 2000.

[56] W. Panofsky and W. Wenzel, "Some considerations concerning the transverse deflection of charged particles in radio-frequency fields," *Review of Scientific Instruments*, vol. 27, no. 11, pp. 967–967, 1956.

[57] A. M. de la Ossa, *et al.*, "Self-modulation of long electron beams in plasma at PITZ," in *AIP Conference Proceedings*, vol. 1507, no. 1. AIP, 2012, pp. 588–593.

[58] *DANFYSIK website,* www.danfysik.com.

[59] G. Asova, "Tomography of the electron beam transverse phase space at PITZ," Ph.D. dissertation, Bulgarian Academy of Science, 2012.

[60] S. Rimjaem, *et al.*, "Physics and technical design for the second high energy dispersive section at PITZ," in *9th European Workshop on Beam Diagnostics and Instrumentation for Particle Accelerators (DIPAC 2009).* Joint Accelerator Conferences Website, 2009, pp. 107–109.

[61] *Bergoz ICT-178-2-XXX-X,* www.bergoz.com.

[62] S. Rimjaem, *et al.*, "Comparison of different radiators used to measure the transverse characteristics of low energy electron beams at PITZ," in *Proceedings of DIPAC*, 2011.

[63] Y. Ivanisenko, "Investigation of slice emittance using an energy-chirped electron beam in a dispersive section for photo injector characterization at PITZ," Ph.D. dissertation, Universitt Hamburg, 2012.

[64] *Alied Vision: Prosilica GC1350 CCD camera,* www.alliedvision.com/en/products/machine-vision-cameras/detail/Prosilica%20GC/1350.html.

[65] H. S. Lee, *Thermal Design: Heat Sinks, Thermoelectrics, Heat Pipes, Compact Heat Exchangers, and Solar Cells*. John Wiley & Sons, 2010.

[66] K. Shukla, "Heat pipe for aerospace applicationsan overview," *Journal of Electronics Cooling and Thermal Control*, vol. 5, no. 01, p. 1, 2015.

[67] P. Muggli, *et al.*, "Photo-ionized lithium source for plasma accelerator applications," *IEEE Transactions on Plasma Science*, vol. 27, no. 3, pp. 791–799, 1999.

[68] C. Vidal and J. Cooper, "Heat-pipe oven: A new, well-defined metal vapor device for spectroscopic measurements," *Journal of Applied Physics*, vol. 40, no. 8, pp. 3370–3374, 1969.

[69] G. Fuhs, "Entwicklung eines Alkalimetallofens mit optischem Zugang fr Teilchenstrahl-getriebene Plasmabeschleunigung," Master's thesis, University of Hamburg, 2014.

[70] J. Good, "Ionization laser optics design for the generation of plasma," Master's thesis, Karlsruhe Institute of Technology, 2013.

[71] M. Gross, *et al.*, "Preparations for a plasma wakefield acceleration (PWA) experiment at PITZ," *Nuclear Instruments and Methods in Physics Research Section A: Accelerators, Spectrometers, Detectors and Associated Equipment*, vol. 740, pp. 74–80, 2014.

[72] E. Öz and P. Muggli, "A novel Rb vapor plasma source for plasma wakefield accelerators," *Nuclear Instruments and Methods in Physics Research Section A: Accelerators, Spectrometers, Detectors and Associated Equipment*, vol. 740, pp. 197–202, 2014.

[73] D. R. Lide, *CRC Handbook of Chemistry and Physics, 2009 – 2010, 90th ed.* Taylor & Francis, 2009.

[74] G. Marr and D. Creek, "The photoionization absorption continua for alkali metal vapours," in *Proceedings of the Royal Society of London A: Mathematical, Physical and Engineering Sciences*, vol. 304, no. 1477. The Royal Society, 1968, pp. 233–244.

[75] H. W. Davison, "Compilation of thermophysical properties of liquid lithium," 1968.

[76] R. Schuetze, "Tests und Simulationen zur Plasmazelle bei PITZ," bachelorarbeit, Technische Hochschule Wildau, 2014.

[77] L. Melton and P. Wine, "Operation of near ideal spectroscopic heat pipes," *Journal of Applied Physics*, vol. 51, no. 8, pp. 4059–4069, 1980.

[78] J.-M. Tournier and M. S. El-Genk, "HPTAM, a two-dimensional heat pipe transient analysis model, including the startup from a frozen state," 1995.

[79] *AgieCharmilles AC Progress VP3,* http://www.gfms.com/com/en/Products/EDM/wire-cut-edm/high-speed-machining/ac-progress-vp3.html.

[80] *ThermoFlex TF1400 recirculating chiller,* www.thermofisher.com/order/catalog/product/TF900/.

[81] *SIEMENS: SIMATIC Controllers,* www.siemens.com/global/en/home/products/automation/systems/industrial/plc.html.

[82] *Pfeiffer Vacuum Pirani gauge head TPR 018, UHV,* https://www.vacuum-shop.com/produkt/pt-r15010/pirani-messrhre-tpr-018-uhv.html.

[83] *Thermocoax heating elements,* http://www.thermocoax.com/download/1662/.

[84] A. Donat, Internal communications.

[85] Y. Renier, "Matching for plasma self-modulation experiment," PITZ Collaboration Meeting, Zeuthen, Germany, Dec 2014.

[86] H. Wiedemann, *Particle accelerator physics.* Springer, 2015.

[87] T. Böhlen, *et al.*, "The FLUKA code: developments and challenges for high energy and medical applications," *Nuclear Data Sheets*, vol. 120, pp. 211–214, 2014.

[88] A. Ferrari, P. R. Sala, A. Fasso, and J. Ranft, "FLUKA: A multi-particle transport code (Program version 2005)," Tech. Rep., 2005.

[89] A. Ferrari, P. Sala, R. Guaraldi, and F. Padoani, "An improved multiple scattering model for charged particle transport," *Nuclear Instruments and Methods in Physics Research Section B: Beam Interactions with Materials and Atoms*, vol. 71, no. 4, pp. 412–426, 1992.

[90] A. Fasso, A. Ferrari, J. Ranft, and P. Sala, "An update about fluka," in *Proc. 2nd workshop on Simulating Accelerator Radiation Environment, SARE-2, CERN-Geneva*, vol. 9, 1995.

[91] *Astral Technology Unlimited, Inc.,* http://www.astraltechnology.com/.

[92] M. McAlees, "Raw material challenges and new technology innovations in the pressure sensitive tape," *DuPont. Circleville, Ohio*, pp. 285–301, 2002.

[93] D. Richter, Internal communications.

[94] J. Hoggatt, "Investigation of the feasibility of developing low permeability polymeric films," Boeing aerospace co Seattle WA, Tech. Rep., 1971.

[95] T. Makita, H. Konishi, and T. Nagasaki, "Helium gas permeability of kapton polyimide film," Japan Atomic Energy Research Inst., Tech. Rep., 1990.

[96] S. J. Schowalter, C. B. Connolly, and J. M. Doyle, "Permeability of noble gases through Kapton, butyl, nylon, and "Silver Shield"," *Nuclear Instruments and Methods in Physics Research Section A: Accelerators, Spectrometers, Detectors and Associated Equipment*, vol. 615, no. 3, pp. 267–271, 2010.

[97] D. Richter, "Investigations of foils for the termination of the plasma cell," in *LAOLA Workshop*, Wismar (Germany), 23 June 2015 – 24 June 2015.

[98] M. Khojoyan, *et al.*, "Beam dynamics studies for particle driven plasma wakefield acceleration experiments at PITZ," *Proceedings of ICAP2012, Rostock-Warnemünde, Germany*, pp. 236–238, 2015.

[99] *Coherent COMPexPro 201F ArF2,* www.coherent.com/lasers/laser/compex.

[100] M. Schinkel, "Aufbau und Optimierung einer Laser-Beamline fr den Ionisation-slaser des Plasmabeschleunigungsexperiments bei PITZ," Master's thesis, TH Wildau, 2015.

[101] *Newport Model 1825-C power/energy meter,* www.newport.com.

[102] *MDC viewports,* www.mdcvacuum.com/DisplayProductContent.aspx?d=MDC&p=meu.5.1.1.1&g=meu511.

[103] *Ocean Optics HR2000+ (Custom),* oceanoptics.com/product/hr2000-custom/.

[104] Y. Renier, *et al.*, "Statistics on high average power operation and results from the electron beam characterization at PITZ," in *8th Int. Particle Accelerator Conf.(IPAC'17), Copenhagen, Denmark, 14â 19 May, 2017.* JACOW, Geneva, Switzerland, 2017, pp. 1806–1808.

[105] S. Corde, *et al.*, "High-field plasma acceleration in a high-ionization-potential gas," *Nature communications*, vol. 7, p. 11898, 2016.

[106] J. Vieira, W. Mori, and P. Muggli, "Hosing instability suppression in self-modulated plasma wakefields," *Physical Review Letters*, vol. 112, no. 20, p. 205001, 2014.

[107] M. Turner, *et al.*, "The two-screen measurement setup to indirectly measure proton beam self-modulation in AWAKE," *Nuclear Instruments and Methods in Physics Research Section A: Accelerators, Spectrometers, Detectors and Associated Equipment*, vol. 854, pp. 100–106, 2017.

[108] W. Lu, C. Huang, M. Zhou, W. Mori, and T. Katsouleas, "Limits of linear plasma wakefield theory for electron or positron beams," *Physics of Plasmas*, vol. 12, no. 6, p. 063101, 2005.

[109] J. Su, T. Katsouleas, J. Dawson, and R. Fedele, "Plasma lenses for focusing particle beams," *Physical Review A*, vol. 41, no. 6, p. 3321, 1990.

[110] R. A. Fonseca, *et al.*, "OSIRIS: a three-dimensional, fully relativistic particle in cell code for modeling plasma based accelerators," in *International Conference on Computational Science*. Springer, 2002, pp. 342–351.

[111] R. Fonseca, *et al.*, "One-to-one direct modeling of experiments and astrophysical scenarios: pushing the envelope on kinetic plasma simulations," *Plasma Physics and Controlled Fusion*, vol. 50, no. 12, p. 124034, 2008.

[112] K. Flöttmann, *ASTRA,* www.desy.de/~mpyflo.

[113] G. Pathak, *et al.*, "Simulations study for self-modulation experiment at PITZ," in *Proceedings of 6th International Particle Accelerator Conference, Richmond, VA, USA*, 2015, pp. 2496–2498.

[114] T. Mehrling, C. Benedetti, C. Schroeder, and J. Osterhoff, "HiPACE: a quasi-static particle-in-cell code," *Plasma physics and controlled fusion*, vol. 56, no. 8, p. 084012, 2014.

[115] M. Khojoyan, A. M. d. l. Ossa, and D. Malyutin, "Optimization and transport of electron beam for self-modulation experiments at PITZ," in *LAOLA Workshop*, Wismar (Germany), 6 Oct 2014 – 7 Oct 2014.

[116] *MAD-X,* mad.web.cern.ch/mad/.

[117] K. Lotov, "Effect of beam emittance on self-modulation of long beams in plasma wakefield accelerators," *Physics of Plasmas*, vol. 22, no. 12, p. 123107, 2015.

[118] T. Mehrling, "Theoretical and numerical studies on the transport of transverse beam quality in plasma-based accelerators," Ph.D. dissertation, University of Hamburg, 2014.

[119] K. Yee, "Numerical solution of initial boundary value problems involving Maxwell's equations in isotropic media," *IEEE Transactions on antennas and propagation*, vol. 14, no. 3, pp. 302–307, 1966.

[120] R. Courant, K. Friedrichs, and H. Lewy, "On the partial difference equations of mathematical physics," *IBM journal of Research and Development*, vol. 11, no. 2, pp. 215–234, 1967.

[121] P. Sprangle, E. Esarey, and A. Ting, "Nonlinear interaction of intense laser pulses in plasmas," *Physical Review A*, vol. 41, no. 8, p. 4463, 1990.

[122] E. Esarey, B. Shadwick, P. Catravas, and W. Leemans, "Synchrotron radiation from electron beams in plasma-focusing channels," *Physical Review E*, vol. 65, no. 5, p. 056505, 2002.

[123] J. M. Dawson, "Nonlinear electron oscillations in a cold plasma," *Physical Review*, vol. 113, no. 2, p. 383, 1959.

[124] D. C. Carey, F. Rothacker, and K. Brown, "Third order TRANSPORT with MAD input: A Computer program for designing charged particle beam transport systems," Tech. Rep., 1998.

[125] M. Krasilnikov, *et al.*, "Electron beam asymmetry compensation with gun quadrupoles at PITZ," in *Proceedings of FEL, Santa Fe, USA*, 2017.

[126] M. Gross, *et al.*, "Observation of the self-modulation instability via time-resolved measurements," *Phys. Rev. Lett.*, vol. 120, p. 144802, Apr 2018.

[127] E. Gschwendtner, "Starting Up the AWAKE Experiment at CERN," in *Proc. of International Particle Accelerator Conference (IPAC'17), Copenhagen, Denmark, 1419 May, 2017*, ser. International Particle Accelerator Conference, no. 8. Geneva, Switzerland: JACoW, May 2017, paper TUOBB2, pp. 1261–1264.

[128] D. Jeppson, J. Ballif, W. Yuan, and B. Chou, "Lithium literature review: lithium's properties and interactions," Hanford Engineering Development Lab., Richland, Wash.(USA), Tech. Rep., 1978.

[129] I. G. R. Gutz, CurTiPot – pH and AcidBase Titration Curves: Analysis and Simulation freeware, version 4.2, http://www.iq.usp.br/gutz/Curtipot_.html.

[130] A. Bejan and A. D. Kraus, *Heat Transfer Handbook*. John Wiley & Sons, 2003, vol. 1.

[131] D. Upper, "The unsuccessful self-treatment of a case of "writer's block"," *Journal of Applied Behavior Analysis*, vol. 7, no. 3, pp. 497–497, 1974.

Acknowledgments

I would like to express my deep gratitude to whose who have contributed, directly or indirectly, to the success of this work:

- Dr. R. Brinkmann, Prof. Dr. F. Grüner, Dr. C. B. Schröder, Dr. F. Stephan for conceiving the experiment.
- Prof. Dr. F. Grüner and Dr. M. Groß for supervising this work.
- Dr. E. Öz and Dr. P. Muggli for discussions on the heat pipe oven design.
- J. Engel, G. Koss, S. Philipp, G. Loisch for their extensive participation in the heat pipe oven studies and preparations.
- Dr. Y. Renier, G. Loisch, Dr. M. Krasilnikov, Dr. I. Isaev for contributions to the measurement procedures and tools used for the experiment.
- Dr. M. Groß, Dr. M. Krasilnikov, G. Loisch for helpful discussions on beam dynamics simulations.
- Members of PITZ group, shift crews and DESY Zeuthen technical staff for operating the accelerator and providing the best possible conditions for the experiment.
- People who have contributed or are still contributing to the experiment: Dr. G. Asova, J. Good, P. Boonpornprasert, Dr. M. Khojoyan, Dr. D. Malyutin, S. Maschmann, A. Myufti, Dr. A. Oppelt, Dr. J. Osterhoff, Dr. A. M. de la Ossa, G. Pathak, B. Petrosyan, M. Reimann, Dr. D. Richter, M. Schinkel, R. Schütze, J. Schultze, Dr. T. Mehrling, P. Weidemann, V. Wohlfarth.
- I want to acknowledge Dr. D. Upper's findings [131], which were reproduced by me multiple times during the time I spent on this work.

Finally, I want to thank my family and friends. They always support and motivate me regardless of success or failure. I am thankful to Alya for her support and for inspiring me on major decisions, such as pursuing a PhD at DESY.

Eidesstattliche Versicherung

Hiermit versichere ich an Eides statt, die vorliegende Dissertationsschrift selbst verfasst und keine anderen als die angegebenen Hilfsmittel und Quellen benutzt zu haben.

Die eingereichte schriftliche Fassung entspricht der auf dem elektronischen Speichermedium.

Die Dissertation wurde in der vorgelegten oder einer ähnlichen Form nicht schon einmal in einem früheren Promotionsverfahren angenommen oder als ungenügend beurteilt.

Ort, Datum Unterschrift der Doktorandin / des Doktoranden